Master Thesis in Physics

Development and Characterisation of a Scintillator Based Muon Detector with SiPM Readout for Air Shower Experiments

Rebecca Meißner

submitted to the

Faculty of Mathematics, Computer Science and Natural Sciences of RWTH Aachen University

conducted at the

III. Phys. Inst. A

First examiner and supervisor: Prof. Dr. Thomas Hebbeker

Second examiner: Prof. Dr. Christopher Wiebusch

December 11, 2015

Abstract

The detection of ultra-high energy cosmic rays (UHECRs) is performed indirectly using the extensive air showers (EASs) which are initiated by the primary particles. A cascade of secondary particles is produced consisting of a hadronic, an electromagnetic and a muonic component. Especially muons are directly related to the mass and energy of the primary making them interesting for air shower experiments.

The Aachen Muon Detector (AMD) is specifically developed for the measurement of the muonic component. A total of 64 scintillator tiles form a sensitive area of $5.76\,\mathrm{m}^2$. Each tile is read out individually. Into each, a wavelength shifting (WLS) fibre is inserted for light collection. The light is coupled into an optical fibre which conducts the light onto a silicon photomultiplier (SiPM). The signal processing, data readout and correction for external influences are controlled by a special front end ASIC for SiPMs, the extended analogue SiPM read out chip (EASIROC). A power supply unit (PSU) powers SiPMs and EASIROC board. The voltage outputs of the EASIROC board for each channel and of the PSU are studied and quantified. Measurements with the whole read out chain, including SiPMs, EASIROC and power supply unit as main components are performed to describe the dark count rate with inclusion of all noise effects of the chain. All electronic components are temperature dependend. Consequently, dark count rate, EASIROC and PSU voltage output change with temperature. These effects are measured and quantified. Subsequently, an algorithm is implemented in the readout software which corrects for these dependencies. Additionally, effects of different configurations of the EASIROC and channel uniformity are quantified. Mechanical couplings are installed between the WLS and the optical fibre and between the optical fibre and the SiPM. Typical damages and impurities of the fibres themselves are shown as they reduce the light yield.

For first test measurements of the Aachen Muon Detector, a shelf is developed into which 8 tiles are inserted above one another. This allows to use multiple tiles in coincidence as trigger and such reduce the noise level caused by SiPM dark noise for a future detailed characterisation of individual tiles. With this setup, atmospheric muons are observed. The observed rate of about $(9.3\pm0.5)\,\mathrm{Hz}$ for a twofold coincidence with the tiles immediately on top of each other complies with the expectation of $(9.5\pm1.1)\,\mathrm{Hz}$.

Contents

Chapter 1

Introduction

Modern astroparticle physics covers a wide field of research aiming at identifying the sources and acceleration mechanisms of cosmic rays. Therefore, the energy spectrum, the mass composition and the arrival direction distribution of the particles are studied. State of the art technologies are installed in new detector designs to improve the measurement accuracy and thus enable more precise analyses.

Ultra-high energy cosmic rays (UHECRs) propagate through the universe and eventually hit the Earth's atmosphere. For energies above E=10^{19} eV, this occurs for less than one particle per square-kilometer and year. When a cosmic ray interacts with an atmospheric molecule, secondary particles are produced which in turn interact further. Thus, an avalanche process is started which forms an extensive air shower (EAS). Within the cascade, three shower components can be identified: The electromagnetic, the muonic and the hadronic component. As no direct measurements of the characteristics of the primary particle can be performed with EAS particles, observables which allow conclusions of the characteristics are studied.

In the currently largest observatory of its kind, the Pierre Auger Observatory, two complementary detectors are installed for the detection of a selection of these observables. The surface detector (SD) consists of 1660 Cherenkov stations covering an area of 3,000 km^2. Secondary particles reaching ground level penetrate through the water detector and emit Cherenkov light which is detected with photomultipliers in the SD stations. The timing of incoming particles and their energy is measured. Out of the response of the individual stations, energy and arrival direction of the primary are reconstructed. The fluorescence detector (FD) overlooks the area with a total of 27 telescopes. The electromagnetic shower component emits fluorescence light while interacting with atmospheric molecules which make high precision energy measurements possible. Thus, the Observatory determines the lateral and longitudinal shower profile.

Although a hybrid detection principle like applied in the Pierre Auger Observatory facilitates the measurement of a wide range of observables, large uncertainties on the energy and mass composition of the primary particle prevail in analyses. Thus, an upgrade with a muon detector is planned. Dedicated muon measurements are very promising to improve the resolution of primary particle characteristics analyses. The number of muons produced in an air shower and their production depth are directly linked to the energy and chemical composition of the primary.

Within this search for a detector extension, a prototype detector is developed in Aachen, the Aachen Muon Detector (AMD). The sensitive area is formed by 64 scintillator tiles making up a total sensitive area of 5.76 m^2. Wavelength shifting fibres collect the scintillation light. For the conduction of the light to the photosensors, optical waveguides are installed. Silicon photomultipliers (SiPMs) are used as sensors. They allow for a single photon resolution, are small in size and have photon detection efficiencies of about 35%. A dedicated application-specific integrated circuit for SiPMs,

the extended analogue SiPM readout chip (EASIROC) is used for data processing and readout.

In the context of this thesis, the Aachen Muon Detector is developed and characterisations of both single components and whole readout chains are performed. An introduction to cosmic rays and air shower physics is given in chapter 2. Hereafter, the detector design of the AMD is described in detail and the detection principle, separated into the individual components, explained, see chapter 3. Subsequently, chapter 4 focuses on the light conduction subsystem which includes stability measurements of fibre couplings and influences on the light output of fibres. In chapter 5, the electronics are studied and the influence of external conditions like temperature on their output is quantified. Measurements with a complete readout chain, including all components from scintillator tile to SiPM to readout electronics, are performed, for example the muonic minimum ionising particle peak. These are described in chapter 6. Finally, a conclusion and outlook is given in chapter 7.

Chapter 2

Study of Cosmic Rays

The history of cosmic rays starts with their discovery in 1912 by Victor Hess. Previously, ionisation of air molecules had been demonstrated with experiments using fully charged electroscopes which discharged themselves without further external influences. In his study aiming at revealing the source of this phenomenon, Hess performed balloon flights to altitudes of up to 5,300 m to measure the discharging rate at different heights. After a firstly decreasing rate to up to 1,000 m height, he found a rate increasing with altitude. Consequently, the radiation was coming from outer space. Werner Kolhörster confirmed the result one year later with measurements at altitudes of up to 9,300 m above sea level [1, 2].

The charged particle nature of cosmic rays was firstly indicated by Clay in 1927. He found the discharging rate to be dependent on the geomagnetic latitude. Hence, a pure gamma ray composition was excluded [1].

In 1935, Regener and Pfotzer performed coincidence measurements with three Geiger-Müller counters at altitudes of up to 28 km. At around 14 km above sea level, they obtained the highest coincident rate. The henceforth called "Pfotzer Maximum" was attributed to electron multiplication in the atmosphere. Within the following years, the spacial distance of the coincidence counters was varied by the groups of Rossi, Schmeiser and Bothe, Kolhörster et al. and Auger. All found the correlated arrival to decrease with increasing spacial distances. It was concluded that the detectable secondary particles originate from the same event and developed as extensive air shower (EAS) through the atmosphere. The additional achievement by Auger was his estimation of the primary energy to 10^{15} eV by using the number of particles, assuming each particle carries its critical energy and taking the energy loss in the atmosphere into account. This is why the discovery of EAS is usually attributed to him [2, 3].

2.1 Cosmic Rays

Since the discovery of cosmic rays, many experiments have been built to investigate their characteristics such as the energy spectrum, the mass composition and the arrival direction. Combined, these characteristics allow conclusions about the sources of cosmic rays, which in turn is a key point in understanding acceleration mechanisms and propagation effects. Up to energies of 10^{14} eV measurements are performed directly above the atmosphere. At higher energies, the characteristics of cosmic rays are deduced from observations of extensive air showers at ground level, see chapter 2.2.

2.1.1 Energy Spectrum

The energy spectrum of the primary cosmic ray particles can be described with a broken power law, i.e. the exponent underlies changes at certain points:

$$J(E) = \frac{\mathrm{d}n}{\mathrm{d}E\,\mathrm{d}t\,\mathrm{d}\Omega\,\mathrm{d}A} \propto E^{-\gamma} \tag{2.1}$$

with the differential flux $J(E)$, kinetic energy per nucleus E, time t, solid angle Ω, area A, and the spectral index γ [1, 4]. By today, measurements cover an energy range of about 14 orders of magnitude, from 10^6 to about 10^{20} eV.

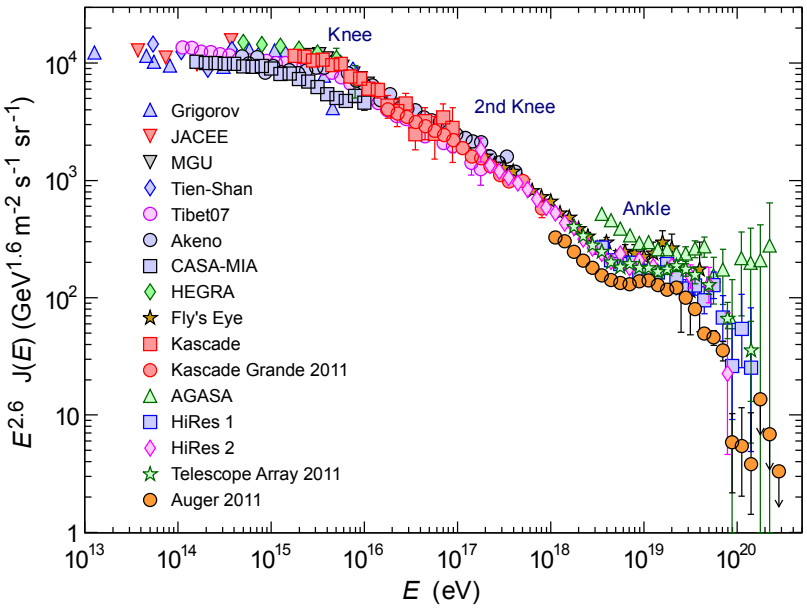

Figure 2.1: All-particle spectrum of cosmic rays as a function of the energy-per-nucleus E. The flux is scaled by $E^{2.6}$. Adapted from [4].

The spectrum (c.f. fig. 2.1) contains certain characteristic features:

At $E_{k1} \approx 4 \cdot 10^{15}$ eV, the position of the **knee**, the spectral index changes from $\gamma = 2.7$ to $\gamma = 3.1$ [1]. Two explanatory approaches exist. The first assumes a maximal acceleration energy of the galactic sources is reached. A successive suppression of elements proportional to the nuclear charge, starting at light elements, induces the steepening of the spectrum. The second approach implies a weak galactic magnetic field which cannot confine particles above E_{k1} in the galaxy. The cutoff is rigidity dependent, meaning that heavy elements with higher charge escape later. Depending on the exact model, the flux suppression reaches the heaviest elements approximately at the **second knee**, at $E_{k2} \approx 3 \cdot 10^{17}$ eV [1, 4]. Additionally, it marks the onset of extragalactic sources.

At the position of the **ankle** at $E_a \approx 3{\cdot}10^{18}$ eV, the spectrum flattens and the spectral index changes back to $\gamma = 2.7$ [5]. The most favoured explanation states that the by now dominating extragalactic flux of higher energetic particles starts to be suppressed [4].

The high energy end of the spectrum, the **cutoff** at around $E_c \approx 5 \cdot 10^{19}$ eV, is challenging to be measured due to the low flux rate. It is still controversial whether the

cutoff is due to an upper end of the acceleration power of the sources or a result of the GZK-cutoff. In the latter case, protons interact with photons of the cosmic microwave background (CMB). A Δ^+-resonance is produced which subsequently decays into a lower energetic proton or neutron and pion. Heavier nuclei are split up by the photo-disintegration process which thus impedes their propagation. As a consequence, nuclei undergo attenuation processes which suppress cosmic rays in the energy range of around 10^{20} eV from sources further away than 100 Mpc [4, 6].

2.1.2 Mass Composition and Arrival Direction

The mass composition and arrival direction of cosmic rays are further important characteristics in the process of identifying the sources. Together with the knowledge of their energy and the galactic and extra-galactic magnetic fields, particles can be backtracked in principle.

The mass composition of cosmic rays is shown in fig. 2.2. It changes from light to heavy in the range from knee to ankle. Shortly before the ankle, the composition lightens. The situation near the cutoff remains unclear as different experiments observe either a heavier composition above 10^{18} eV (Pierre Auger Observatory) or a remaining light one (HiRes) [6, 7].

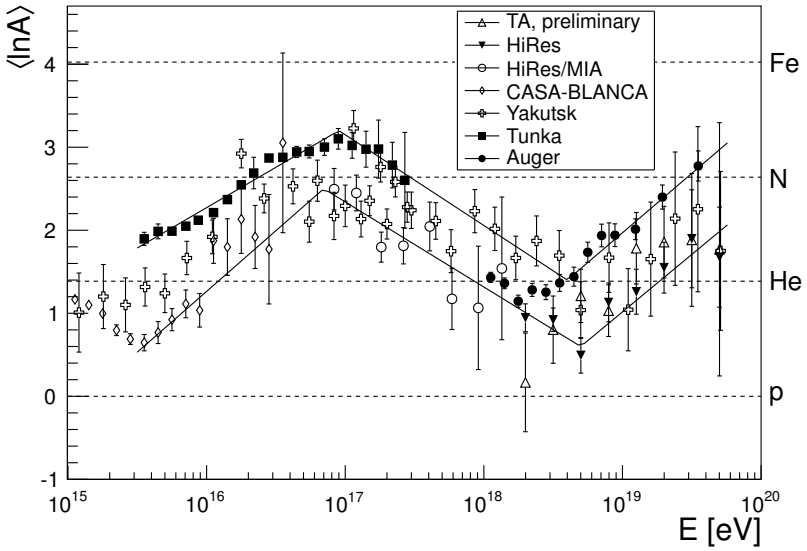

Figure 2.2: Mean logarithmic mass number A derived from measurements with fluorescence detectors over energy. Measurements are only possible on statistical basis, hence the composition is given as mean. The two solid lines symbolise estimates on the experimental systematics. The calculated nuclei equivalent scale takes the interaction model EPOS 1.99 [8] as a basis. Adapted from [9].

In terms of large scale anisotropies a dipolar structure was found by the Auger Collaboration for particles with energies above $8 \cdot 10^{18}$ eV. In equatorial coordinates the position points to 95°±13° in right ascension and -39°±13° in declination with a chance probability of $6.4 \cdot 10^{-5}$ [10]. A joint analysis from the Pierre Auger and the Telescope Array collaborations reinforces the dipolar pattern [11].

2.1.3 Origin

Identifying sources of high energetic cosmic rays requires consideration of propagation effects. On the one hand, particles interact with the CMB which influences their energy distribution and composition. On the other hand, charged particles are deflected in the cosmic magnetic field which affects both their arrival direction and their arrival time. Especially higher Z nuclei are affected by deflection due to the higher charge they carry [7].

For the sources themselves, some specifications can be given by the relation of the maximal acceleration energy $E_{\max}$ of a source and its magnetic field B, its radius R and the charge of the accelerated particles Ze

$$E \leq E_{\max} \simeq 10^{18}\,\mathrm{eV} \cdot Z \cdot \beta \cdot \frac{B}{1\mu\mathrm{G}} \cdot \frac{R}{1\mathrm{kpc}} \tag{2.2}$$

where β is the speed of the accelerating medium in units of the speed of light [7]. A necessary condition for the size of the site of acceleration is that it is comparable to the Larmor radius. If the Larmor radius exceeds e.g. the thickness of the galactic disk, the particles cannot be confined within it. Hence, cosmic rays of the highest energies, which have higher Larmor radii than the galactic disk, must have sources of extragalactic origin. The Hillas plot summarises several astrophysical objects with known radius and magnetic field regarding their acceleration power by applying eq. 2.2, see fig. 2.3. Only few can accelerate cosmic ray particles into the ultra-high energy region, these include neutron stars, gamma ray bursts (GRBs), the intergalactic medium (IGM) and active galactic nuclei (AGNs) [6, 7].

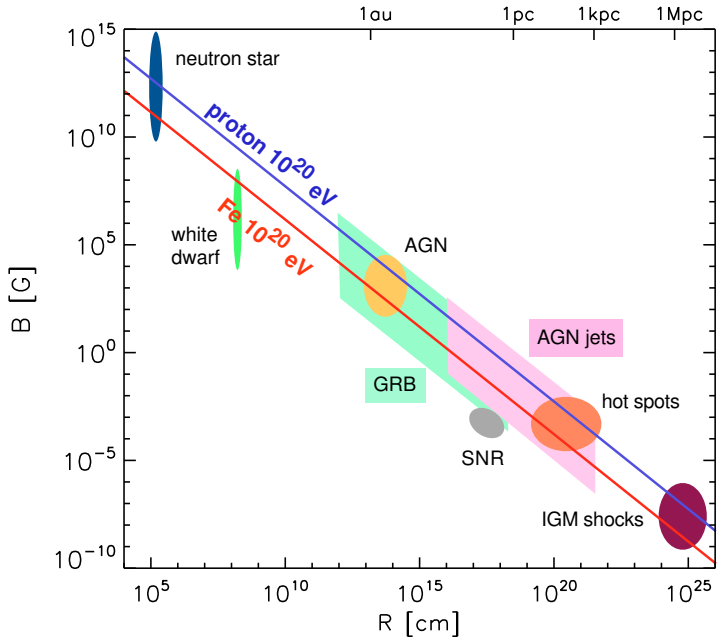

Figure 2.3: Updated Hillas plot. Source candidates for UHECRs are shown taking their radius and magnetic field into account. The blue line symbolises the limit for the confinement of protons with energies of 10^{20} eV. Below the line an acceleration to these energies is not possible. The corresponding limit for iron particles is shown with the red line. Taken from [7].

Identifying the source types leads to the question of acceleration mechanisms. Different explanation approaches exist. For the favoured ones, the injection spectrum of the sources explains the ultra-high energy cosmic ray (UHECR) spectrum after propagation, both in energy range and as a power-law. One of these approaches is the first order Fermi acceleration. When a shock wave, e.g. of a supernova remnant (SNR), propagates with velocity $\beta = v/c$, particles are deflected back and forth by scattering centers both in the surrounding medium and the shock front. At each cycle, they undergo an energy gain of $\Delta E/E \sim \beta$. While this can explain scenarios in GRBs, AGNs and SNRs, other sources like neutron stars are more likely to be characterised by different approaches [7].

Until today, the search for discrete sources of cosmic rays of the highest energies remains without positive result [12].

Thus, the energy spectrum around the cutoff, the mass composition and the arrival direction of UHECRs are current topics of research to yield more information about their sources and acceleration mechanisms.

2.2 Extensive Air Showers

Direct measurements of cosmic rays are performed up to energies of $\mathrm{E} = 10^{14}\,\mathrm{eV}$ [2]. For example satellites and balloons are sent above the atmosphere to take data. For higher energies, the number of events is too small for this kind of experiments with very limited detector sizes. Instead, indirect measurements with ground-based detectors are performed. These usually consist of an array of individual detector stations. Their detection principle, detector spacing, height above sea level and total area vary depending on the investigated energy range.

An incoming high-energy primary hadronic cosmic ray particle interacts with a nucleus in the upper atmosphere creating both charged and neutral mesons ($\pi^{\pm}$, π^0, $K^{\pm}$, K^0, and possibly others). Most of them interact further giving rise to an extensive air shower (EAS). Within such an EAS, an electromagnetic, a muonic and a hadronic component can be distinguished, see fig. 2.4. Showers initiated by electrons develop only an electromagnetic component.

The hadronic component results from hadronic interactions creating mostly protons, neutrons, pions and kaons. The electromagnetic component consists of electrons, positrons and photons and the muonic one of positively and negatively charged muons. The latter two components originate from the decay of mesons: Neutral pions have a short decay length ($c\tau = 25.5\,\mathrm{nm}$ [4]) compared to their interaction length (about 900 m at sea level). Hence, they decay promptly into two photons which subsequently give rise to the electromagnetic shower component. Charged pions have longer decay lengths ($c\tau = 7.8\,\mathrm{m}$ [4]). Therefore, interacting processes prevail until the energy falls below the critical energy E_c^{π} ($E_c^{\pi} = 20\,\mathrm{GeV}$ in air [5]). For energies below E_c^{π}, charged meson decays into muons prevail. The electromagnetic component is enriched at each interaction step (one third of the energy is passed to the electromagnetic component) and by the decay of some of the muons into electrons. Similar interaction chains apply for kaons instead of pions.

Hence, cascades of secondary particles spread out. Many of them carry sufficient energy to reach ground level and they are produced in numbers high enough to be detected as particle shower [2, 5].

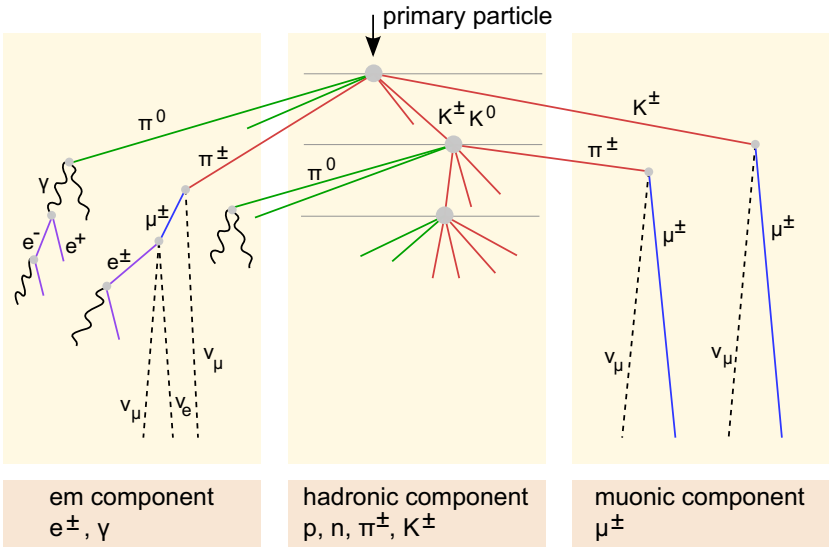

Figure 2.4: Schematics of the development of an extensive air shower. A primary hits a nucleus of the upper atmosphere creating light hadrons and mesons. Out of these, the electromagnetic (em), muonic and hadronic components evolve. In an adopted Heitler model, each hadronic interaction step above the critical energy of a π creates N_π neutral mesons (green) and $2N_\pi$ charged ones (red). ν stand for neutrinos and antineutrinos.

A shower initiated by a 10^{19} eV proton for example produces about $3 \cdot 10^{10}$ particles at ground level of which 99% belong to the electromagnetic component. This component carries 85% of the primary particle's energy where each electron, positron or photon carries 1 to 10 MeV. Muons and pions are transporting about 10% and 4% of the energy where each particle carries about 1 GeV and a few GeV, respectively [5]. The footprint of the shower measures approximately a few km^2, see fig. 2.5a. Hence, detector arrays of thousands of km^2 are needed for their detection at a sufficient rate. For comparison, for showers with energies of about 10^{15} eV thousands of m^2 are sufficient [5].

Since the energy, the mass and the arrival direction of the incoming primary particle are not directly measurable, they have to be deduced from other parameters. An important mass sensitive observable is the atmospheric depth of maximal shower particle production $X_{\max}$. It is expressed in the production depth $X(h)$ which quantifies the total amount of traversed matter before the interaction in units of $[X] = \mathrm{g\,cm^{-2}}$ in dependence of the production distance h which is measured from sea level upwards, see fig. 2.5b:

$$X(h) = \int_h^\infty \rho(h')\,\mathrm{d}h' \tag{2.3}$$

with $\rho(h)$ being the density of air, see fig. 2.5b. Insertion of the Boltzmann barometric equation and integration gives

$$X(h) = X_{\mathrm{ref}} \cdot \mathrm{e}^{-h/h_{\mathrm{ref}}} \tag{2.4}$$

with the atmospheric depth at sea level $X_{\mathrm{ref}} = 1,030\,\mathrm{g\,cm^{-2}}$ and $h_{\mathrm{ref}} = 8.4\,\mathrm{km}$ [15]. For inclined showers, the amount of traversed matter increases with zenith angle θ which

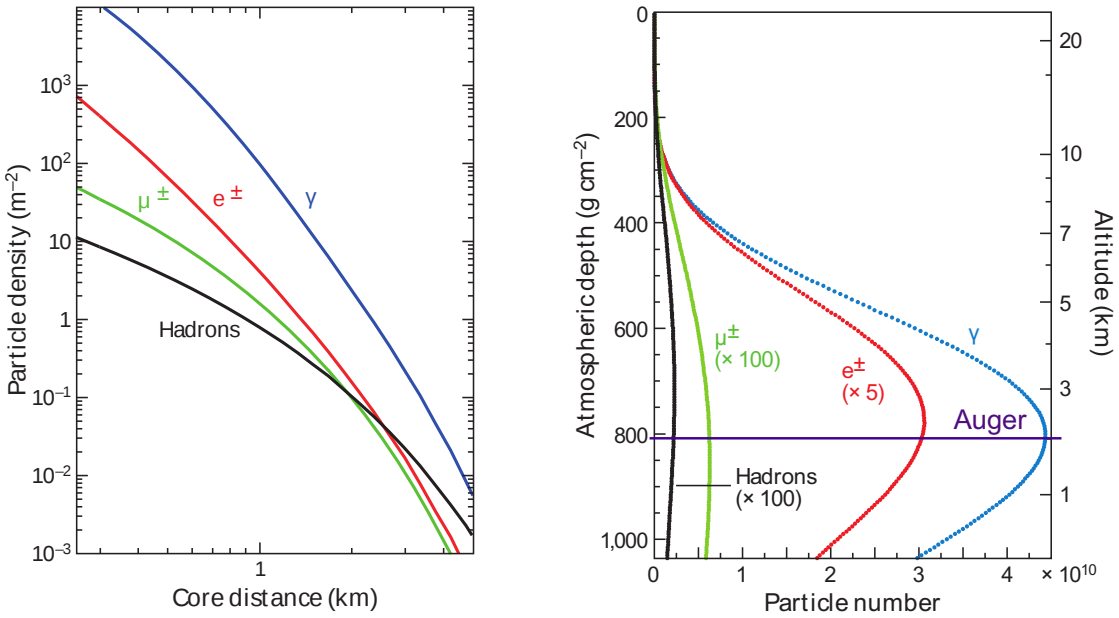

(a) Lateral shower distribution. **(b)** Longitudinal shower distribution

Figure 2.5: CORSIKA [13] simulations of the lateral and longitudinal distribution of a shower initiated by a vertical incoming proton of 10^{19} eV. The lateral profile gives only the number of particles and is not energy weighted. The single muons carry much higher energies than the particles of the electromagnetic component. Thus, in an energy weighted distribution the importance of muons is much increased. The lateral profile corresponds to the atmospheric depth of the Pierre Auger Observatory of $807\,\mathrm{g\,cm^{-2}}$, this depth is also indicated in 2.5b. Energy cuts for $e^{\pm}$ and photons are at 0.25 MeV and for muons and hadrons at 0.1 GeV. Taken from [14].

is the angle between shower axis and normal to the ground, according to

$$X(h,\theta) = X(h) \cdot \frac{1}{\cos(\theta)} \quad . \tag{2.5}$$

Protons carry a higher energy per nucleon than heavy nuclei. Each nucleon of a primary particle creates an own avalanche process after the first interaction developing individually and in parallel. Thus, proton initiated showers evolve their maximum $X_{\max}$ deeper in the atmosphere than heavier nuclei. Hence, mass composition studies are feasible, see fig. 2.6.

An energy sensitive observable commonly used for ground-based observatories with detector arrays of individual stations is the particle density interpolated at a fixed distance to the shower core. A lateral distribution function (LDF) is fitted to the signals $S(r)$ of the single stations using e.g. a phenomenologically motivated parametrisation of the Nishimura-Kamata-Greisen (NKG) function

$$S(r) = k \cdot \left(\frac{r}{r_\mathrm{s}}\right)^{-\beta} \cdot \left(1 + \frac{r}{r_\mathrm{s}}\right)^{-\beta} \tag{2.6}$$

where r is the distance to the shower axis, k is the normalisation constant, r_s is the scaling parameter and β is the slope parameter determined from data or simulations [17].

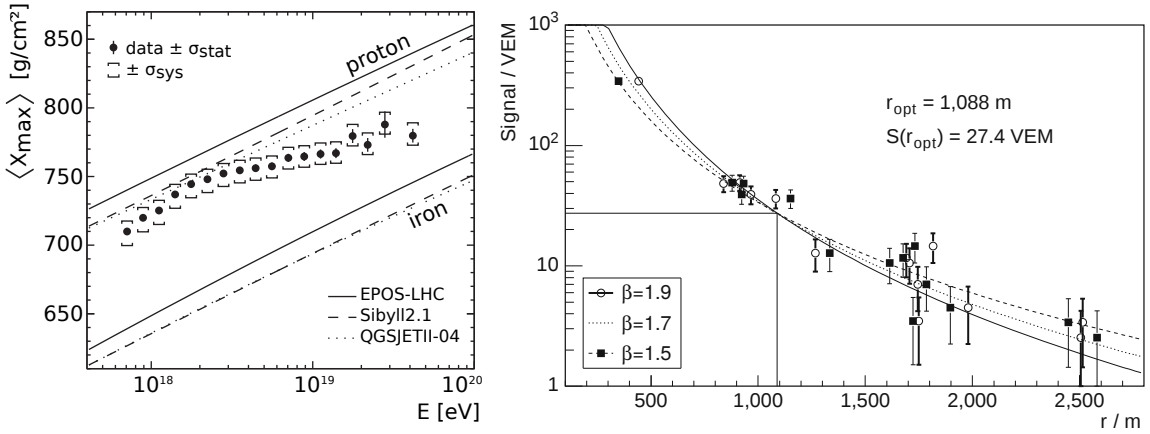

(a) Dependence of the mass sensitive observable $X_{\max}$ over energy. For UHECRs only measurements on statistical basis exist, so the mean $\langle X_{\max} \rangle$ is taken. Protons evolve deeper in the atmosphere, i.e. at higher $X_{\max}$ values. Different hadronic interaction models differ in the predicted depth. Taken from [16].

(b) The optimal distance for the energy estimator $S(r_{\text{opt}})$ is determined by the point at which the signal is independent of the free parameter β. The signal is converted into a signal expected for vertical equivalent muons (VEM) in a single detector station. Examples for the Pierre Auger Observatory. Taken from [15].

Figure 2.6: Observables for the determination of the mass and energy of the primary particle.

At a certain distance r_{opt} of the shower core the obtained fitted signal is independent of the LDF variables. Instead, it depends only on the characteristics of the primary particle and can hence be used as energy estimator. For a detector spacing of 1.5 km, $r_{\text{opt}} \approx 1,000\,\text{m}$ [15], see fig. 2.6.

2.2.1 Muonic Component

The quality of reconstructed characteristics of the primary particle improves with the amount of measured quantities of the air shower. Muons have an important part within the determination process. They are directly linked to the hadronic component as they are produced via pion decay $\pi^{\pm} \rightarrow \mu^{\pm} + \nu_{\mu}/\nu_{\bar{\mu}}$ and to a smaller fraction by kaon decay. Thus, the number of muons and their production depth contain information about energy and mass of the primary, see fig. 2.7. Low energetic muons also result to up to 10% from the electromagnetic component which is only a minor contribution [15].

In an adopted Heitler model there are n_{ch} charged and n_{neut} uncharged pions produced at each interaction step giving in total $n_{\text{tot}} = n_{\text{ch}} + n_{\text{neut}}$ (see fig. 2.4). Interaction of charged pions continues until the energy of the single particle falls below E_c^{π}. Neutral pions decay into photons. Applying this model, the number of steps N_{steps} has to fulfill the condition

$$(n_{\text{tot}})^{N_{\text{steps}}} = \frac{E_0}{E_c^{\pi}} \tag{2.7}$$

where E_0 is the initial energy of the primary. For later simplification the factor κ is

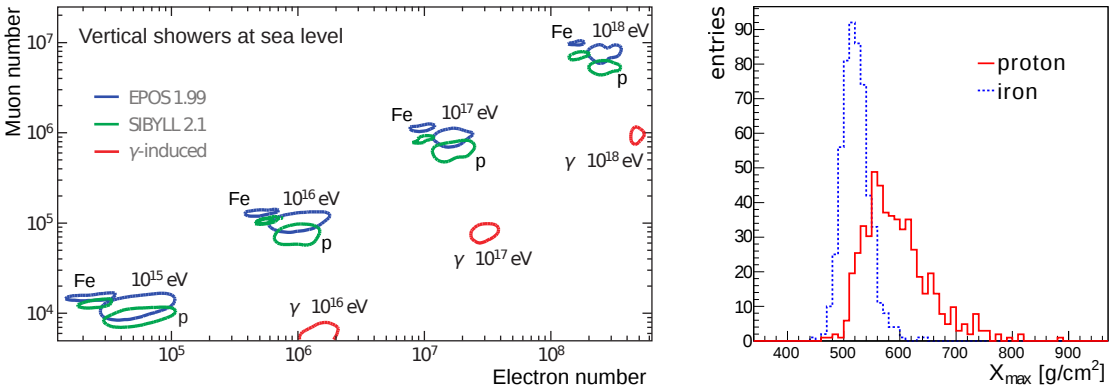

(a) Mass discrimination with the number of muons and electrons.

(b) Mass discrimination with $X^{\mu}_{\max}$.

Figure 2.7: 2.7a: Simulation of the discrimination power of the number of muons and electrons with vertical showers. Taken from [14]. 2.7b: Simulation with EPOS-LHC [18] of the muon production depth (MPD) distribution $X^{\mu}_{\max}$ of $3{\cdot}10^{18}$ eV showers with zenith angles between 55° and 65°. The MPD can be used for primary mass determination. Taken from [19].

introduced, following

$$\kappa = \frac{\ln n_{\mathrm{ch}}}{\ln n_{\mathrm{tot}}} \qquad \Leftrightarrow \qquad n_{\mathrm{ch}} = (n_{\mathrm{tot}})^{\kappa} \qquad . \tag{2.8}$$

Under the assumption that all $\pi^{\pm}$ decay into muons when reaching E^{π}_{c} (branching ratio $\pi^{\pm} \rightarrow \mu^{\pm} + \nu_{\mu}/\nu_{\bar{\mu}}$: $99.98770 \pm 0.00004\%$ [4]), the number of muons in a proton initiated shower is then given by

$$N^{p}_{\mu} = (n_{\mathrm{ch}})^{N_{\mathrm{steps}}} = \left(\frac{E_0}{E^{\pi}_{c}}\right)^{\kappa} \tag{2.9}$$

[5, 20]. For heavier primaries with atomic number A, the same model is used. A superposition of A nucleons, each of energy E_0/A gives

$$N^{A}_{\mu} = N^{p}_{\mu} \cdot A^{1-\kappa} = A \cdot \left(\frac{E_0/A}{E^{\pi}_{c}}\right)^{\kappa} \tag{2.10}$$

which implies that heavier nuclei produce more muons as $\kappa < 1$ [20]. Thus, the number of muons can be used as primary mass estimator under the knowledge of the energy, see fig. 2.7a. More muons are produced for primaries with higher atomic numbers with the same total primary energy ,see fig. 2.8. For comparison, the number of electrons shows a reverse dependency. For primaries with many nucleons, each nucleon carries a lower energy than for low atomic number primaries. Thus, the number of interaction generations is smaller as the critical energy is reached faster. As the electromagnetic component increases its energy with each interaction step, fewer generations imply a weaker electromagnetic component [21], see fig. 2.7a.

Each primary possesses distinct hadronic properties. These influence the hadronic cascade and consequently the muon production depth (MPD). Hence, the MPD distribution contains mass sensitive information. Furthermore, hadronic interaction studies

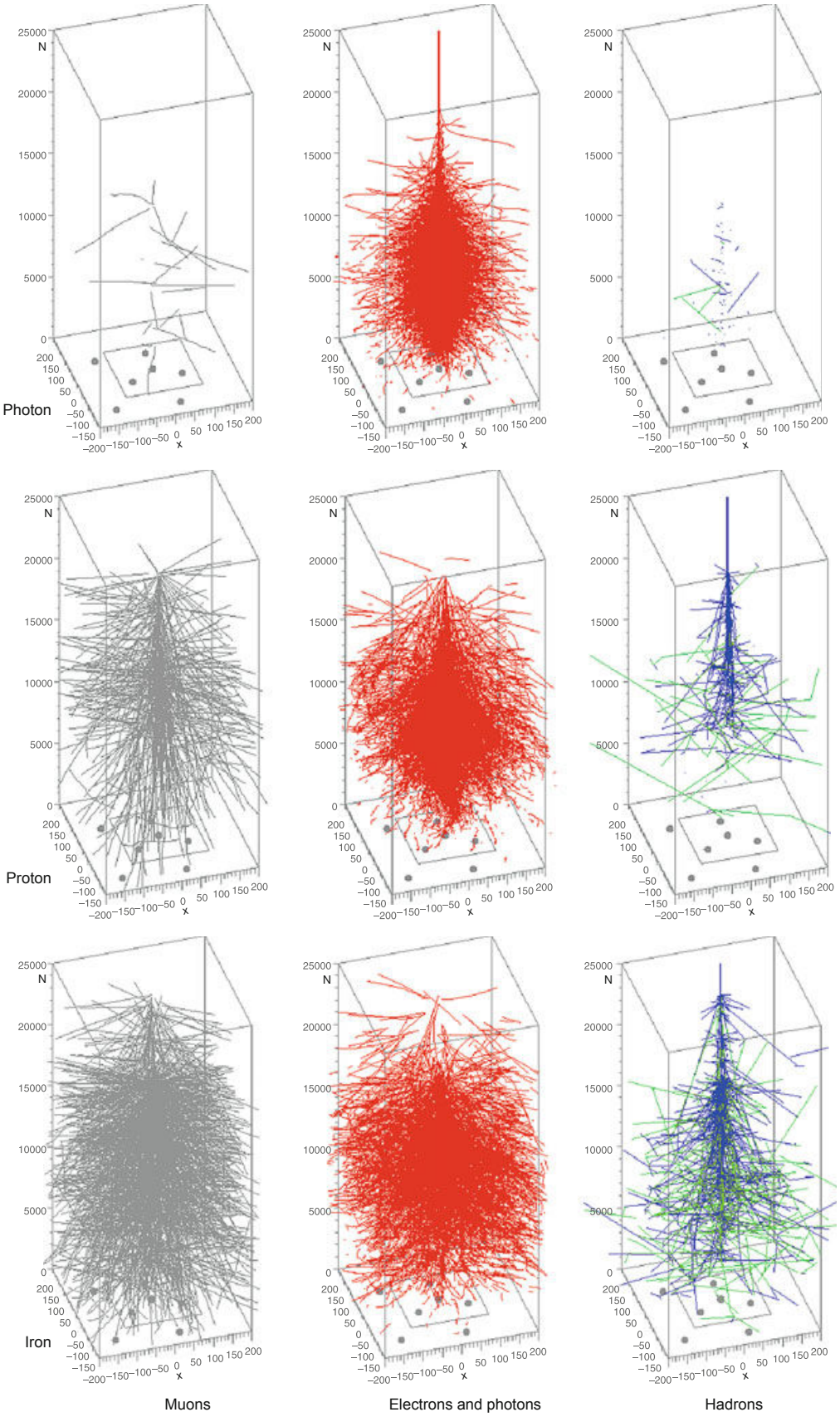

Figure 2.8: CORSIKA [13] simulation of air showers initiated by a 10^{13} eV photon, proton, and iron nucleus. The tracks of the muonic, electromagnetic and hadronic component are separated. Taken from [15].

at ultrahigh energies are possible [19]. To determine the point of production of muons it is assumed that muons travel in straight lines with the speed of light c and are created along the shower axis. These assumptions are motivated by the small contribution of bremsstrahlung and multiple scattering. Due to these characteristics, the arrival time t of a muon can be transformed into its production distance along the shower axis z

$$z \simeq \frac{1}{2}\left(\frac{r^2}{c\cdot(t-\langle t_\epsilon\rangle)} - c\cdot(t-\langle t_\epsilon\rangle)\right) + \Delta - \langle z_\pi\rangle \tag{2.11}$$

where r is the distance from the muon's impact point to the shower axis, Δ is the distance between shower plane and impact point, z_π is the decay length of a π representing the path traveled by the mother meson and $\langle t_\epsilon\rangle$ is the mean kinematic delay which arises e.g. from energy loss processes and causes muons to travel with a velocity smaller than c [19], c.f. fig. 2.9. The production distance z from eq. 2.11 is inserted into eq. 2.3 to convert it into the production depth $X^\mu(z)$. Here, the production depths refers only to the muonic component. The set of $X^\mu(z)$ of a single shower forms the MPD. To extract mass sensitive information, a Gaisser-Hillas function is fitted to the profile

$$\frac{\mathrm{d}N}{\mathrm{d}X} = \frac{\mathrm{d}N_{\max}}{\mathrm{d}X}\left(\frac{X-X_0}{X^\mu_{\max}-X_0}\right)^{\frac{X^\mu_{\max}-X_0}{\lambda}} \cdot \mathrm{e}^{\frac{X^\mu_{\max}-X_0}{\lambda}} \tag{2.12}$$

where $\frac{\mathrm{d}N}{\mathrm{d}X}$ is the differential number of particles and X_0, $X^\mu_{\max}$, $N_{\max}$ and λ are the four free parameters. $X^\mu_{\max}$ describes the maximum of the profile, i.e. the depth at which muon production reaches its maximum. $N_{\max}$ is the maximal number of particles observed at $X^\mu_{\max}$. X_0 and λ are parameters depending on primary mass and energy. The quantity $X^\mu_{\max}$ is mass sensitive as showers initiated by heavier nuclei develop faster and higher in the atmosphere, see fig. 2.7b. It provides a complementary measure of the mass composition to the $X^{em}_{\max}$ distribution of the electromagnetic component measured with fluorescent light [19].

Consequently, both muon number and muon production depth provide a fundamental access to the mass and energy of the primary cosmic ray particle.

2.3 Pierre Auger Observatory

The measurement of extensive air showers induced by ultra-high energy cosmic rays requires detectors covering huge surface areas as the flux decreases exponentially with energy (see chapter 2.1.1). Currently, the largest experiment for this purpose is the Pierre Auger Observatory with an area of 3,000 km^2. For zenith angles below 60° the aperture is 7,350 km^2 sr. The observatory is located in the Argentine Pampa Amarilla in the province of Mendoza, close to the city of Malargüe. This specific location was chosen to allow for the fewest disturbance impacts possible. Thereby, some of the relevant conditions were namely a pure atmosphere, little light pollution, a flat surface for the detector, and the height above sea level of 1416 m [22].

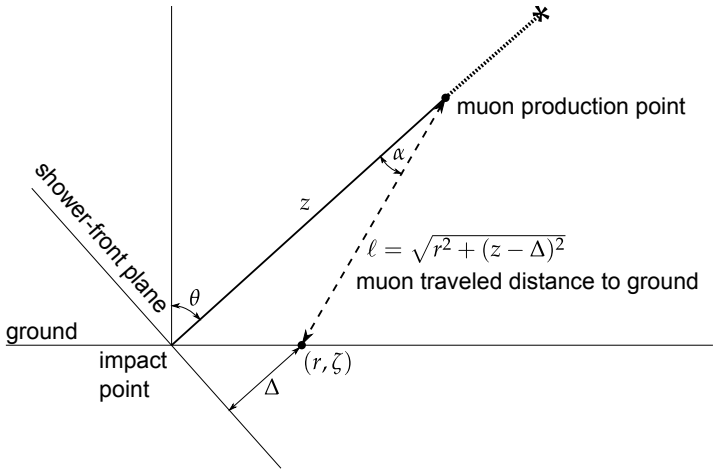

Figure 2.9: Geometry used to calculate the path of the muon using the arrival time structure. The coordinates (r,ξ) are measured in the reference frame of the shower. Taken from [19].

(a) Photo of an SD station (front) and FD building (back). Taken from [23].

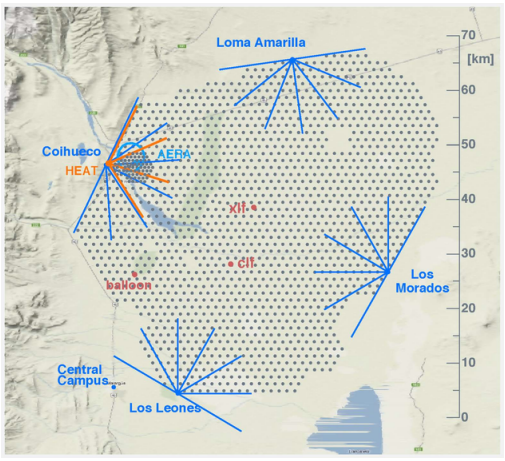

(b) The SD stations are symbolised by grey dots and the field of view of the FD (HEAT) in blue (orange) lines. Taken from [24].

Figure 2.10: Site of the Pierre Auger Observatory with surface detector (SD) and fluorescence detector (FD).

2.3.1 Hybrid Detection Principle

The Pierre Auger Observatory combines two different types of detector to a hybrid detection principle. These are the Surface Detector (SD) and the Fluorescence Detector (FD), see fig. 2.10a. In the near future, a muon detector "AugerPrime" will complement the Observatory. While the SD measures the secondaries at ground level and hence the lateral distribution of an extensive air shower, the FD measures the energy deposited in the atmosphere and thus the longitudinal distribution of an EAS. Using complementary techniques entails advantages such as an improved reconstruction of the geometry and energy of showers, the possibility to cross-calibrate both detectors and a reduction of systematic uncertainties. Since 2004, data of extensive air showers with energies above

10^{18} eV are taken with the hybrid detector. In 2009, the observatory was supplemented by the High Elevation Auger Telescope (HEAT) to extend the energy range down to energies of 10^{17} eV [22].

Fluorescence Detector (FD)

The fluorescence detector comprises four buildings housing six fluorescence telescopes each and the HEAT site with 3 telescopes in an additional housing (see next paragraph). The sites are located along the edges of the surface covered by SD, see fig. 2.10b. All 24 telescopes are aligned to overlook this area uniformly. The observed quantity of FD is fluorescence light emitted by excited nitrogen molecules of the atmosphere. Charged secondary particles, especially electrons and positrons, collide with the molecules and lift one of its electrons into a higher state. During de-excitation, photons in the ultra-violet up to the visible-blue range are emitted. Thus, ultra-violet (UV) and partially infra-red (IR) pass-filters are used to reduce the noise level due to visible light and let mainly fluorescence light pass to the camera of the reflector telescopes. The IR pass range is an undesired side effect in the UV pass-filters. The focal plane of each telescope comprises 440 PMTs. Their field of view adds up to a total of $30\times30°$. To avoid damage to the PMTs, operation is only feasible in moonless nights. Hence, the duty cycle of FD is only in the order of $10-15\%$. The technique enables a near calorimetric measurement of the energy of the shower [25].

High Elevation Auger Telescope (HEAT)

As the fluorescence detector measures the flux of cosmic rays in higher energy regions than other ground based observatories, a direct comparison of their results was impractical. Hence, the Pierre Auger Observatory was supplemented by a low energy extension. It consists of three fluorescence telescopes identical in construction to the FD telescopes but with a higher inclination angle. Thus, higher atmospheric regions are within the field of view. This facilitates the fluorescence light detection of the secondary particles of lower-energetic primaries ($E \approx 10^{17}$ eV) which deposit their energy earlier after entering the atmosphere. These primaries give rise to fainter showers. With the HEAT being closer to these faint showers even their detection is enabled. Consequently, the energy range is extended [26].

Surface Detector (SD)

The surface detector consists of an array of 1,660 Cherenkov detectors covering an area of 3,000 km^2. The individual stations are arranged in a hexagonal grid with a spacing of 1.5 km. The tanks have a round base of 10 m^2, a lightproof enclosure and are filled with 12 t of pure de-ionised water. To prevent the water to be contaminated biologically or chemically a foil is installed in each tank. To reflect the diffuse light towards the light sensors, the foil is highly reflective. Furthermore, it serves as an additional shielding against external light [27].

In an area of 23.5 km^2, the spacing of the tanks is reduced to 750 m. The Auger Muon and Infill for the the Gorund Array (AMIGA) serves as low-energy extension and is in the field of view of HEAT. The infill was completed in 2011 [26].

Secondary particles reaching ground level (1,400 m a.s.l.) penetrate into the detectors. Charged particles whose speed exceed the speed of light in the medium, emit Cherenkov

light. The same applies for electrons and positrons created by energetic photons in the water of the station. Subsequently, the Cherenkov light pulses are detected by three photomultiplier tubes (PMTs) mounted at the inner top of each station. The signal is recorded into flash analog-to-digital converter (FADC) traces. Time stamps are taken from GPS antennas to allow for precise timing of the signals. The particle density or lateral distribution of the EAS at ground level is measured. Since the detection principle is independent of external conditions like weather and daytime, a duty cycle of nearly 100% is achieved [28].

2.3.2 Muon Separation with the Current Detector

Most of the particles reaching ground level are muons, electrons, positrons and photons. The charged particles mainly have energies exceeding the Cherenkov threshold. The differentiation of these components is crucial for mass composition analyses. But it is only possible on statistical basis with the current detectors.

To optimise the separation power, the SD tank height was chosen to be 1.2 m. In this configuration, about 85% of the electromagnetic component is absorbed making the signal proportional to the initial energy [27]. Since electrons have only a short path length before they interact in water (e.g. about 5 cm for 10 MeV particles [28]), many small peaks can be observed in the FADC traces. In case of photons, the water volume allows for the development of an electromagnetic cascade which is mainly contained in the detector volume. The amount of light is proportional to the energy. Electrons, positrons and photons combined cause a smooth and elongated signal contribution in the FADC traces. In contrast, muons lose 2 MeV/cm in water [28]. Thus, they travel through the whole tank causing a signal proportional to their geometric path length. A short light pulse in the order of nanoseconds is produced. The FADC traces show a short, large peak with fast rise time and exponential decay which is earlier in time than the electromagnetic component [29, 28], see fig. 2.11. In order to reconstruct the mass sensitive geometrical production height of muons the arrival time of muons is needed (see eq. 2.11). Therefore, it is required that the muon peaks can be clearly distinguished and isolated from the electromagnetic component in the FADC traces. Since the density of incoming particles decreases rapidly with distance to the shower axis, this generally applies for detectors which are at least some 100 m away from the shower core [28, 30]. The arrival times of muons is converted into the muon production depth (MPD) to infer the primary mass sensitive observable X^{μ}_{max} (see eq. 2.3). Under the assumption that simulations fit real shower events and by comparing simulation and data, conclusions on the mass composition can be drawn [19].

For the energy reconstruction of the shower the energy estimator S(1000) can be used (see eq. 2.6). It describes the fitted signal at 1,000 m from the shower axis. S(1000) is cross-calibrated with the energy estimator of the FD. A lateral distribution function (LDF) is fitted to the integrated amplitudes of the FADC traces and the signal at 1,000 m is interpolated. Subsequently S(1000) is converted into an energy measure [19, 27].

A more direct method for primary energy determination but in turn limited by the knowledge of the primary mass, is the use of very inclined showers only [32]. For showers with zenith angles above 60° the path through the atmosphere is long enough to absorb all other components but the muonic one, see fig. 2.11. Thus, a direct measurement of the number of muons at ground level is provided. Under the knowledge of the mass of

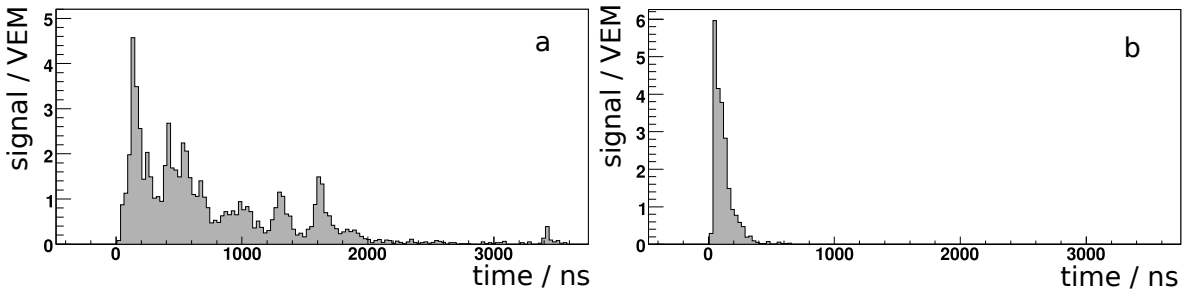

Figure 2.11: Signal characteristics in the FADC trace of a shower with zenith angle = 22° (a) and an inclined shower with zenith angle = 80° (b), shown for an SD station 1 km distant of the shower core. Event a: The muonic component peaks early and high in the trace whereas the electromagnetic component shows some smaller peaks and a background signal. Event b: The inclined event has only a muonic component. The signal is measured in vertical equivalent muons (VEM). Taken from [31].

the primary particle, the energy is directly inferred with eq. 2.10 [20, 29].

The direction of the shower is reconstructed using the relative arrival times of muons at the SD stations. A parabolic shower front is fitted to the data and the direction of the shower is estimated in coordinates of the zenith angle θ and azimuthal angle φ [27].

2.3.3 Extension by a Muon Detector

The current detector design with the FD and the SD allows only for an evaluation of the number of muons on a statistical basis since the measurements of the muonic component remain indirect in large parts. Additionally, their analysis depends on simulations which are strongly dependent on models describing the hadronic interaction of high energies. Currently, diverse hadronic interaction models are compared to data, either with a pure proton or a mixed or iron composition. All predict a smaller number of muons than observed [29, 28], see fig. 2.12.

A better description of the muonic component is also essential for a better understanding of the electromagnetic and the hadronic shower component, as they are all connected within the shower development [20].

Dedicated muon detectors can thus help to overcome some of these limitations. Such dedicated detectors for the detection of cosmic rays are already implemented in other experiments. The experiment Karlsruhe Shower Core and Array Detector (KASCADE) was taking data from 1996 till 2009 of EAS in the energy region around the knee. In 2003 it was extended to KASCADE-Grande. A muon tracking detector based on streamer tubes allows for the separation of the electromagnetic and the muonic component [33, 34].

Now, a dedicated muon detector is planned for the Pierre Auger Observatory called "AugerPrime". With direct muon measurements an improved description of hadronic multiparticle production and interactions is obtainable, leading to further constraints on hadronic interaction models. Together with composition sensitive observables, these enhanced models allow for mass composition studies at energies in the region of the GZK-cutoff. Once composition-tagging is possible on an event-by-event basis, proton initiated showers can be separated from those which originate from higher-Z nuclei. Protons are deflected less in the galactic and intergalactic magnetic field and are hence

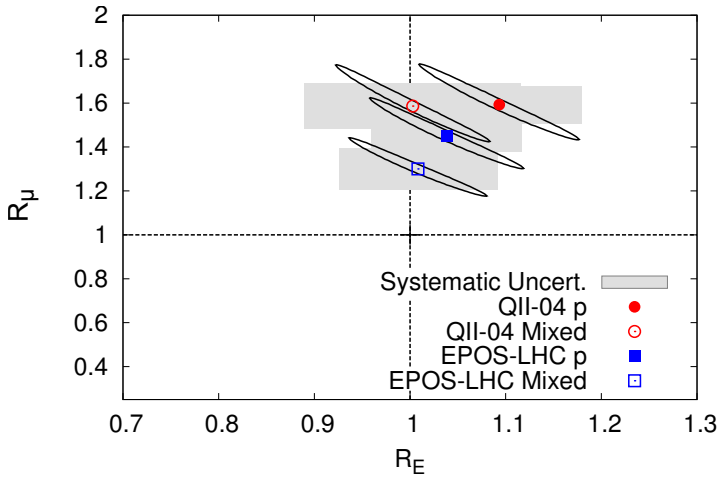

Figure 2.12: Energy and hadronic scaling parameters for different simulation tools. The rescaling factor of the energy R_E is compatible with 1 within the uncertainties, implying that the predicted energy matches the observed one. The hadronic / muon rescaling factor indicates that the prediction of the muon size needs to be increased by a factor of 1.3 - 1.6 to fit the observed muon size, depending on the model. Taken from [29].

preferable for anisotropy studies and source detection. A direct detection of muons is therefore a step towards the clarification of the flux suppression and whether it is caused by source characteristics or propagation losses [35].

As the array of KASCADE is much smaller ($200 \times 200\,\mathrm{m}^2$), different requirements and possibilities regarding e.g. material use prevail for the Upgrade of the Pierre Auger Observatory. One of the proposed upgrade options with detectors already in the field is the Auger Muons and Infill for the Ground Array (AMIGA). The individual stations are buried alongside the SD stations. The detection principle is based on scintillator counters and signal readout with photomultiplier tubes (PMTs) [26, 36]. The advantage of underground detectors is that the electromagnetic component is absorbed in the layer of earth above the detector leaving only the muonic signal. The disadvantage of the detector is the horizontal distance to the SD stations which inhibits the detection of the same particles in both detectors. The Aachen group is proposing a detector underneath the SD stations with scintillators and SiPM readout.

Chapter 3

Aachen Muon Detector

Dedicated muon measurements open a promising window for the study of cosmic rays at the highest energies. The KASCADE experiment revealed the importance of analyses of cosmic rays in the knee region and since recently the Pierre Auger Observatory sets priority in extending their physics reach by planning a new dedicated muon detector. Within this upgrade challenge, a prototype project was started in Aachen, the Aachen Muon Detector (AMD) [37], which is also an interesting concept for general muon detection in air shower physics.

The fundamental requirements are on the one hand determined by the conditions given when operating a detector in the field of the Pampa Amarilla, such as deployment, amount of required detector stations, power supply and environmental influences. On the other hand, the specifications on the physics output define parameters of the detector like size, efficiency and position.

The design chosen by Aachen addresses these requirements by constructing a scintillator based detector with silicon photomultiplier (SiPM) readout in a robust and waterproof housing out of steel. The AMD is split into two halves to allow for a better handling and assembly. They are equal in layout and completely independent from each other. Hence, if not stated otherwise, information is given for one half only.

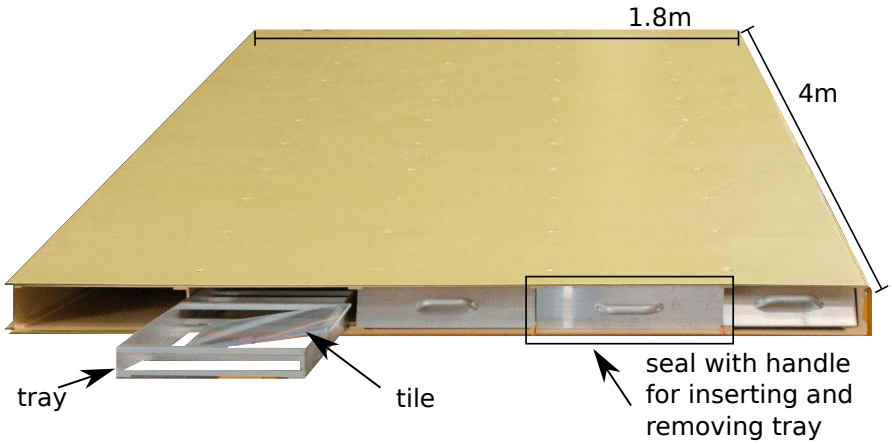

Figure 3.1: Photo of the Aachen Muon Detector prototype. One tray is partly removed for demonstration. The SiPM carrier boards sit at on the end of each tray. One chamber (on the right) is reserved for all other electronics (EASIROC and PSU) and cables.

The housing is split into four elongated chambers, see fig. 3.1. Each of these rows holds a tray with eight scintillator tiles. Hence, the active detector area consists of 32 scintillator tiles. The trays can be inserted and removed individually for practical purposes such as maintenance work, see fig. 3.2. Special boundaries on the trays hold the tiles in fixed positions. When a particle travels through the tile, scintillation light

is produced. Wavelength shifting fibres collect the light in the tiles and optical fibres guide the light onto photo-sensors, see fig. 3.2. In the AMD, SiPMs are installed as photo-sensors. There is one SiPM for each tile giving each tile its own readout channel. All eight photo-sensors of a chamber sit on a carrier board at one of its ends, allowing for an easier operation and handling. A dedicated front-end application-specific integrated circuit (ASIC) for SiPM data readout, the Extended Analogue SI-pm ReadOut Chip (EASIROC), is installed. It is integrated into an evaluation board. The voltage for the readout board and the SiPMs is supplied by a power supply unit which is specially designed to be powered by the 24 V of the SD battery. A schematics of the AMD is shown in fig. 3.3.

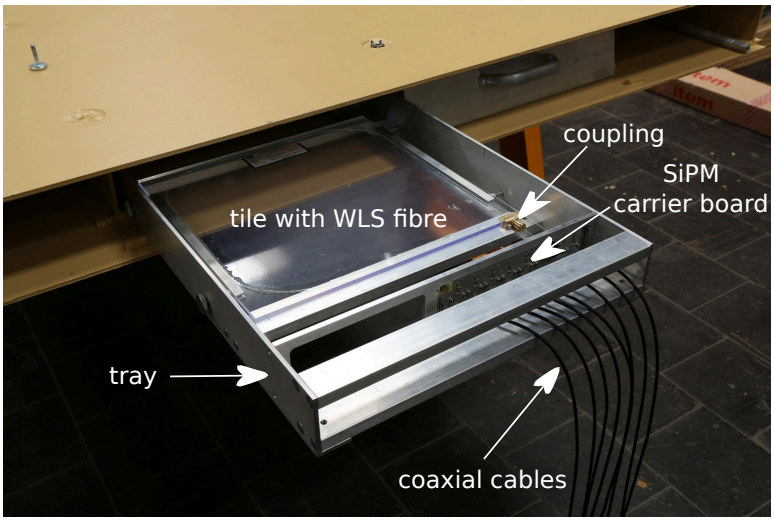

Figure 3.2: One tray partly removed from the Aachen Muon Detector prototype. A wavelength shifting fibre is glued into the scintillator tile. An optical fibre is coupled onto the WLS fibre and conducts the light onto one of the SiPMs.

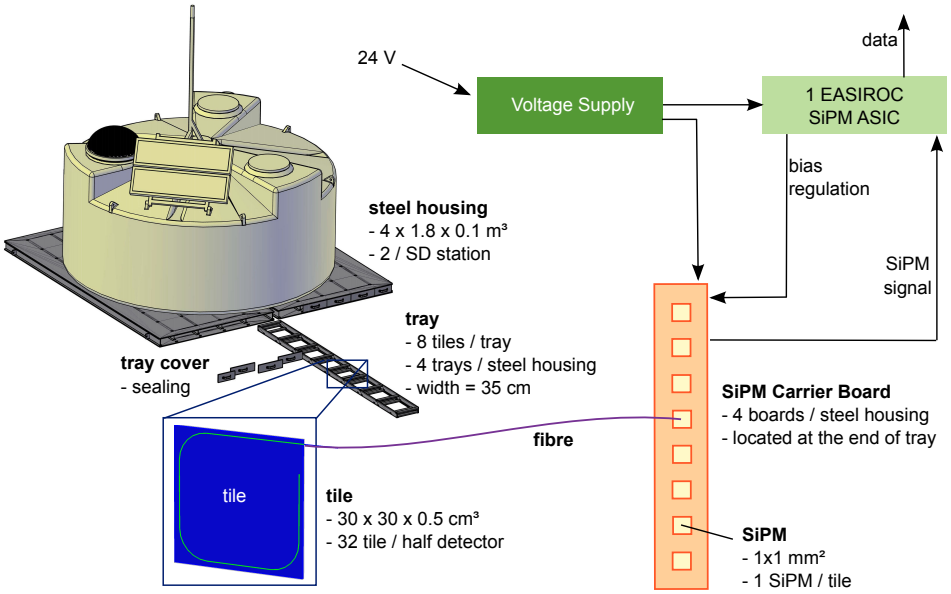

Figure 3.3: Schematics of the Aachen Muon Detector with all its components.

The modular design with 64 tiles was chosen for several reasons. Firstly, the spatial

information together with the assumption that all particles originate from the shower axis may help in the arrival direction reconstruction of the particles. Secondly, the dynamic range is increased by reading out each tile individually instead of only one light sensor for the whole detector. Thus, higher muon hit rates are resolvable. Additionally, the light yield and timing is improved for smaller tile sizes. Finally, a practical reason is the mechanical stability which is higher for smaller tiles than for a single big one.

The steel support structure is developed to allow for placing the AMD beneath a 12 t SD station. The outer dimensions amount to $4\times1.8\times0.1\,\mathrm{m}^3$ taking into account the diameter of 3.6 m of an SD tank. Thus, the SD tank serves as shielding for a main part of the electromagnetic component. Still, a mixed composition of electromagnetic and muonic component will be measured by AMD like in the SD but with a higher fraction of muons. For the later analysis of data, Monte Carlo simulations are essential to separate both components. The AMIGA detector avoids this dependence on simulations by burying the stations 2.3 m deep next to the SD station position. But the advantages of placing a detector right under the SD tank include that the SD is exposed to the same particles. Thus, further information about the particles is available. These include that an interplay of both detectors increases the spatial resolution of the path of the particle and the identification of particles is enhanced. Additionally, the SD station can provide a trigger. Considering the assembly, no burying is needed as the SD tank serves as shielding. The geometrical design (with a muon detector below the SD tank) was inspired by another proposal for the muon upgrade, the "Muon Array with RPCs for Tagging Air Showers"(MARTA) [38] which uses resistive plate chambers (RPC) for muon detection. In case of maintenance, an easy access is available. The steel housing can be sealed to protect the detector components from environmental influences such as humidity, wind, sand and external light. The cables for communication, power supply line to the SD battery, trigger, timing and data transfer are guided through waterproof adapters out of or into the detector.

In the following, the individual components of the Aachen Muon Detector are discussed in detail.

3.1 Shower Particle Detection with Plastic Scintillators

Scintillators are widely used within high-energy physics. The basic concept is to convert part of the kinetic energy of an incoming particle into fluorescent light. Ideally, the relation between light yield and deposited energy is proportional.

In organic scintillators the energy level structure of a molecule causes fluorescence [39]. The electron configuration consists of singlet states S_x with spin=0 and triplet states T_x with spin=1, where $x = 0$ is the ground state (only for singlets) and $x > 1$ represent excited states. The energy gap between S_0 and S_1 is about 3-4 eV. With higher excitation states the gaps become smaller. Each excited state splits up into several vibrational states with energy spacings in the order of 0.15 eV. As the average thermal energy is about 0.025 eV at room temperature, all molecules populate the ground state. By absorbing energy of particles passing through the scintillator, the molecular structure is excited into one of the vibrational states of S_1 and above, see fig. 3.4. This is followed by fast non-radiative internal conversions to the S_1 state without vibrational excitation. Subsequently, either fluorescence light is emitted ($\mathcal{O}$(ns)) when the electron configuration de-excites into the ground state S_0 or the structure converts

into the triplet state T_1 via an inter-system crossing. In the latter case, phosphorescence is emitted ($\mathcal{O}$(ms)) during de-excitation to S_0 or alternatively the system is thermally excited back to S_1. In the succeeding de-excitation, delayed fluorescence is emitted. Ideally, fluorescence light clearly outweighs phosphorescence and delayed fluorescence. The absorption and emission processes follow the Franck-Codon principle, stating that the nuclear change is insignificant compared to electronic transitions. Since internal degradation processes take place before the emission of photons, the emission spectrum is shifted with respect to the absorption spectrum. This is known as Stokes shift and makes the scintillator transparent for its own wavelengths [39].

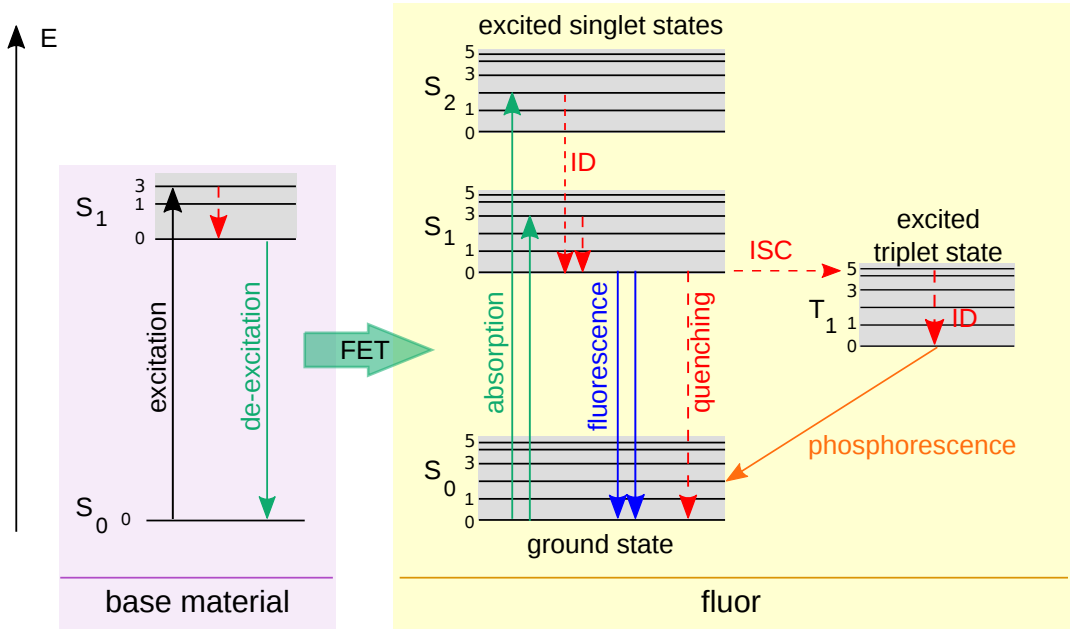

Figure 3.4: Schematics of working principle of plastic scintillator consisting of a base material and added fluor. Abbreviations: S for singlet state, T for triplet state, FET for Förster energy transfer, ID for internal degradation and ISC for inter-system crossing. Adapted from [39, 40].

Plastic scintillators consist of a base material, for the Aachen Muon Detector this is the commonly used polyvinyltoluene (PVT), mixed with a soluble organic fluorescent material. The base easily absorbs energy of the traversing particles. In resonant dipole-dipole interactions the energy is passed from base to the primary fluorescent emitter which is called Förster energy transfer (FET). Subsequently, the same process as for pure organic scintillators occurs, see fig. 3.4. This combination shortens the rise and decay time of the scintillator by taking advantage of the particular characteristics of base and fluor [4].

Disadvantages of plastic scintillators in contrast to e.g. inorganic scintillators include their smaller light output, aging and their susceptibility for radiation damages. The damage depends on both integrated dose and dose rate, atmosphere and temperature. Colour centers absorbing stronger in the UV than blue light or fogging of the scintillator may occur [41]. The effects are still poorly understood. Advantages are that plastic scintillators can be formed into large and complex shapes making them an attractive choice. Their temperature dependency is small and they are cheap compared to inorganic scintillators. They are very fast in rise and decay time and allow for pulse-shape

discrimination [4].

For AMD, the EJ-212 plastic scintillator from Eljen Technology [42] is used. In the whole detector, 64 scintillator tiles with 30 cm×30 cm×0.5 cm each make up the sensitive surface of 5.76 m^2 of the whole detector. The thickness is a trade-off of costs given by the requirements for a huge array which gives priviledge to thin tiles and physics performance which ideally requires thick tiles. The spacing between the tiles amounts to 7.5 cm. Consequently, the sensitive area may be increased in future versions to 7.84 m^2 with tiles of up to 35 cm×35 cm each, without requirement of additional changes of the detector. The refractive index of the material of the scintillator is 1.58. Values close to the refractive index of glass of 1.5 are favoured to allow for an efficient coupling to optical devices.

The time response can be described with the fluorescent light intensity

$$I(t) = I_0 \cdot \left(\mathrm{e}^{-t/\tau_{\mathrm{decay}}} - \mathrm{e}^{-t/\tau_{\mathrm{rise}}}\right) \tag{3.1}$$

where $\tau_{\mathrm{decay}} = 2.4\,\mathrm{ns}$ is the decay time of the fluorescence light and $\tau_{\mathrm{rise}} = 0.9\,\mathrm{ns}$ is the rise time to populate the luminescent states [39], stated values are for EJ-212 [42].

The differential light yield $\mathrm{d}L/\mathrm{d}x$ is the fluorescence energy emitted per unit length and can be described with Birks' formula

$$\frac{\mathrm{d}L}{\mathrm{d}x} = \frac{S \cdot \frac{\mathrm{d}E}{\mathrm{d}x}}{1 + k \cdot B \cdot \frac{\mathrm{d}E}{\mathrm{d}x}} \tag{3.2}$$

[39]. The numerator alone is the linear response to the specific energy loss $\mathrm{d}E/\mathrm{d}x$ of the charged particle. Here, the scintillation efficiency S is the proportional constant (AMD: $S \approx 10,000\,\mathrm{photons}\,/\,1\,\mathrm{MeV\,e^-}$ [42]). But as quenching occurs, i.e. processes diminishing the scintillation efficiency as e.g. non-radiative de-excitation processes, a non-linear part is added in form of the denominator. The constant B describes the density of damaged molecules and k is the fraction of those leading to quenching. Their product is specific for each scintillator and has to be determined experimentally [39]. The light output is stable in a range from -60°C to 20°C and reduces to 95% at 60°C for EJ-212 [42].

(a) Unwrapped tile. **(b)** PFTE wrapping. **(c)** Tyvek wrapping.

Figure 3.5: Unwrapped and wrapped scintillator tiles. As light is lost at the edges of the tile, PFTE and Tyvek wrappings are tested to reduce the effect.

The edges of a scintillator are regions of high light losses, see fig. 3.5a. Wrapping the tiles into reflective materials can guide the exiting light back into the scintillator. For defining the best output for the Aachen Muon Detector, both wrapped and pure scintillator tiles are used. Three different types of wrapping are utilised: Polytetrafluo-

rethylen (PFTE) tape and two types of Tyvek®. In case of the PFTE wrapping, firstly thread seal tape with 12 mm width and 0.1 mm thickness is used to cover the sides. Afterwards, a 50.8 mm wide and 0.2 mm thick tape is wound around the tile slightly diagonally to allow for covering the edges, see fig. 3.5b. The procedure is repeated perpendicular to the first layer. For Tyvek wrapping, two materials of the style 10 series (hardstructure series) are chosen to test whether difference in the output occur: The 1082D with a thickness of (270 ± 80) µm and (98 ± 1) % opacity and a similar one with additional coating specially absorbing in the ultraviolet range [43]. The sheets are cut into shapes which allow for a complete and tight covering of the tiles, see fig. 3.5c. To avoid external light from penetrating through the PFTE or Tyvek into the detector, two aluminium layers are placed above. The edges of the tiles are reinforced by paper. A better handling of the tiles is enabled by a last layer of Tyvek.

A study of the optical reflectance of commonly used reflectors found that Teflon® tape which is similar to the used PFTE tape is a nearly pure Lambertian light distributor, i.e. the emitted light is proportional to the cosine of the angle between the observational angle and the surface normal, see fig. 3.6. Tyvek shows a complicated behaviour, neither fitting specular nor diffuse reflectors nor linear combination of both, see fig. 3.6. The relative reflection coefficients were determined with respect to four layers of Teflon. A selection of materials is shown in table 3.1 [44]. All materials except aluminium foil show similar high coefficients.

Reflector	Reflection coefficient ± standard deviation
Teflon (4 layers)	1.000 ± 0.006
Teflon (3 layers)	0.992 ± 0.004
Tyvek paper	0.979 ± 0.004
Aluminium foil	0.787 ± 0.014
Titanium dioxide paint	0.951 ± 0.003

Table 3.1: Average reflection coefficients of commonly used optical reflectors for incident angles between 14° and 78°. Values are normalised to results of four layers of Teflon. Taken from [44].

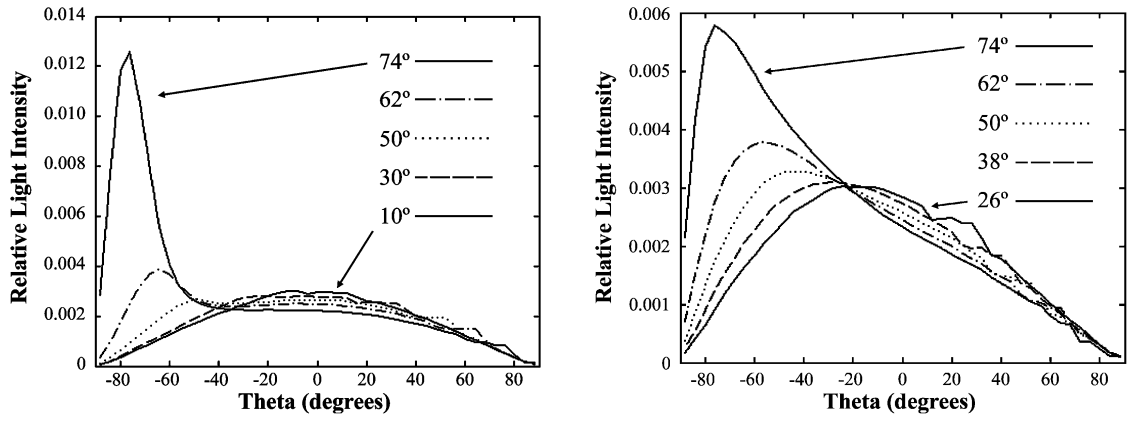

(a) Teflon **(b)** Tyvek

Figure 3.6: Angular distribution profile of reflectivity measurements of Teflon (3 layers) and Tyvek for incidence angles as indicated in the plots. Taken from [44].

When handling the scintillator, gloves have to be worn all the time to avoid fingerprints on the surface. Furthermore, performing the wrapping process in a clean room is highly advisable since the scintillators are electrostatically charged after removing their protective foil and therefore attract dust easily.

3.2 Light Collection and Conduction with Fibres

The light of the plastic scintillators is collected with wavelength shifting (WLS) fibres, coupled into optical fibres at one end and conducted onto the light sensors. The non-coupled end of the WLS fibre is treated with aluminium paint to make it reflecting for light loss avoidance.

Wavelength shifting fibres work similar to plastic scintillators with added wavelength shifting dopant. Photons enter the fibre, get absorbed and excite the molecular structure. Non-radiative transitions like for scintillators plus an additional wavelength shift due to the dopant material are followed by an isotropic emission of photons of longer wavelength. Thus, the WLS fibres are mostly transparent for their own light. This prevents the re-absorption of previously produced photons. The induction of light is indirect. This means, the light is not coupled into the fibre by one of the end surfaces but is a result of absorption and de-excitation processes.

For the Aachen Muon Detector, WLS fibres from Saint-Gobain of type BCF-92 [45] are used. They are fast blue to green shifters which implies that their absorption spectrum fits to the emission spectrum of the plastic scintillator EJ-212, see fig. 3.7a. The decay time amounts to 2.7 ns and the trapping efficiency to 3.44% minimum (general value given for round fibres from Saint-Gobain [45]). The overlap of emission spectrum of the scintillator and absorption spectrum of the WLS fibre should be as high as possible to enable an efficient coupling. For the same reason, WLS fibres are usually embedded into the scintillator. In case of the AMD, a sigma-shaped groove is milled into each tile with a distance of 1 cm to its edge and the WLS fibres are inserted into them, see fig. 3.2 and fig. 3.3. No minimal bending radius is given in the specifications of the fibre but studies have shown a rapid decrease in light output for bending radii smaller than 50 mm which becomes exponential for radii below 25 mm [46]. This is taken into account by guiding the fibres in curves with radius 65 mm around the edges. Fixation is achieved by glueing the WLS fibre into the tile with the optical cement BC-600 from Saint-Gobain [47]. The refractive index is n=1.56 and thus matches the index of the scintillator (1.58).

WLS fibres have a small absorption length which is the length at which the signal decreases to 1/e of its original strength. In case of the BCF-92 it amounts to about 3.5 m [45]. Since the distance from tile to light sensors is up to 2.9 m long, the use of WLS fibres only for light conduction would weaken the signal too much and non-uniformly. Instead, clear optical fibres are used for conducting the light over longer distances. To allow for an efficient coupling of the fibres, a small part of the WLS fibre of 10 mm protrudes out of the tile. Here, both fibres are held together mechanically with a specially developed coupling by the mechanical workshop of the III. Phys. Inst. A, RWTH Aachen, see chapter 4.1.

In the AMD, the optical fibre ESKA CK-40 from Mitsubishi is installed. The absorption length is with about 14 m more suitable for light conduction [49]. To match the outer physical characteristics of the WLS fibre, the diameter of both fibres is 1 mm

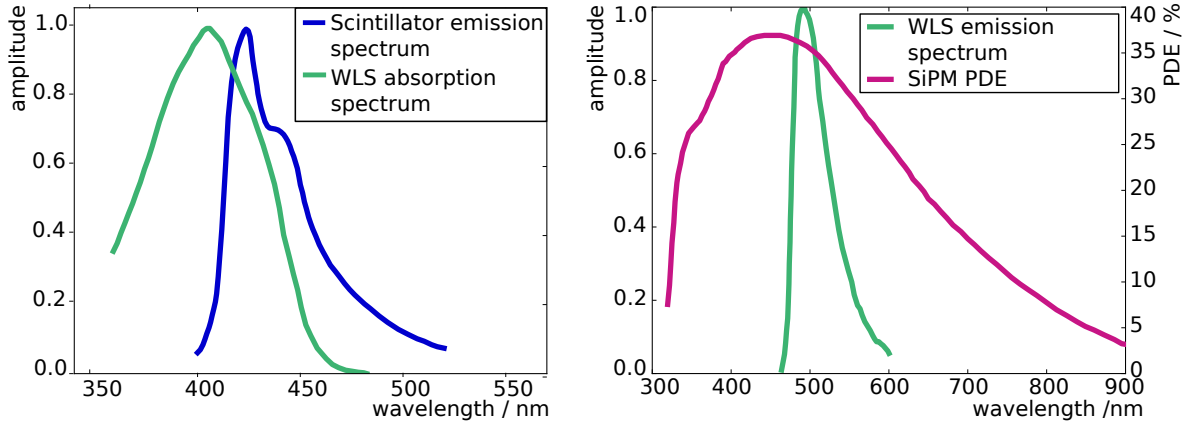

(a) Scintillator emission spectrum and WLS absorption spectrum. A high overlap guarantees little light loss and a good coupling of the light into the fibre.

(b) WLS emission spectrum and SiPM photon detection efficiency (PDE). The PDE spectrum fully covers the emission spectrum which reduces the number of undetected photons and increases the light yield.

Figure 3.7: Emission and absorption spectra of scintillator, WLS fibre and SiPMs. High overlaps guarantee a high light yield. Adapted from [42, 45, 48].

with a diameter of the core of 0.98 mm. The optical properties do not correspond perfectly. While the WLS fibre has an exit angle of $\alpha_e = 35.7°$C, the optical fibre has an acceptance angle of $\alpha_a = 30.5°$, see fig. 3.8 But a study of the exit characteristics of light from fibres investigated the exit angles with the result that only few light rays exits the fibre in the critical range for the AMD between α_a and α_e [50].

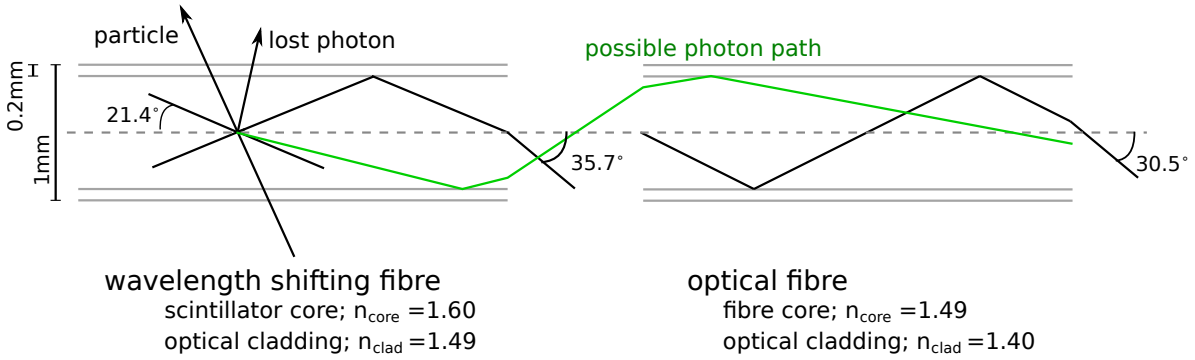

Figure 3.8: Schematics of induction and conduction of light in a wavelength shifting and optical fibre. The maximal exit angle of the WLS fibre is 35.7° while the maximal acceptance angle of the optical fibre is 30.5°. Adapted from [45, 49].

Temperature stability of the WLS and optical fibre is given from -20°C to +50°C and -55°C to 70°C, respectively. Since the light sensors are installed at one end of each tray, the optical fibres from scintillator tiles to light sensors have different lengths. The design is the same for each tray. The shortest optical fibre measures 0.3 m and the lengths increase over 0.7, 1.0, 1.4, 1.8, 2.2, 2.5 m to the maximum of 2.9 m for the most distant tile. Along the tray, spacers ensure that the optical fibres stay apart from each other to avoid optical crosstalk between them.

3.3 Light Detection with Silicon Photomultipliers

Silicon photomultipliers (SiPMs) are installed as light sensors, see fig. 3.9a for a microscopic view. These are single photon sensitive detectors consisting of an array of avalanche photodiodes (APDs) which are operated in Geiger-mode. In the context of SiPMs, a single G-APD is also referred to as a cell. There is one SiPM for each fibre, meaning that every scintillator tile has its own readout channel.

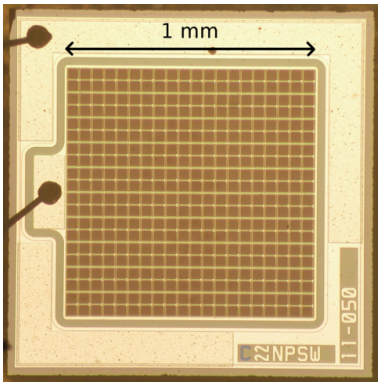

(a) Microscopic view on the active surface of a 1 mm^2 SiPM with 400 cells.

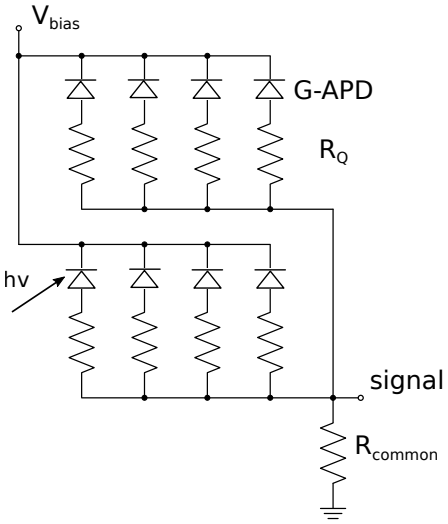

(b) Schematics of an array of cells, quenching resistor R_Q and connection circuit. Adapted from [51].

Figure 3.9: Silicon Photomultiplier (SiPM) microscopic view and electronics schematics.

A photodiode consists of an n-doped and a p-doped semiconductor connected as a pn-junction. A reverse bias voltage is applied to the photodiode which creates a depletion region, see fig. 3.9b. When a photon hits the depletion zone and gets absorbed, energy is transferred to one of the valence electrons of the silicon. The electron is lifted into the conduction band creating an electron-hole pair. If the photodiode is operated in Geiger-mode with an electric field of $> 5{\cdot}10^5$ V/cm [51], the electron and the hole are accelerated to energies high enough to create secondary charge carriers. A self-sustaining ionisation cascade is initiated. The cell breakdown has to be stopped externally by a quenching resistor which is connected in series. Once the cell becomes conductive due to the cascade, current flows through the resistor. As a consequence, the voltage and thus the electric field in the depletion zone decreases to a value too small to sustain the avalanche in the G-APD. The cell breakdown stops and the cell starts to recover [52]. The pulse shape is characterised by rise and recovery time. The rise time is influenced by the size of the cell and the capacitance from the circuit which connects it to the anode and cathode. The recovery time can be expressed via

$$\tau_{\text{rec}} = R_Q \cdot C \tag{3.3}$$

where R_Q is the quenching resistor and C is the capacitance of the cell which in turn is dominated by the cell pitch [51].

Every initiation event amounts to an identical output signal for a fully charged cell. Hence, a single cell produces a binary output. The signal height is determined by the gain of the SiPM which is the ratio of output charge to the charge of an electron q and can be calculated via

$$G = \frac{C \cdot V_{\text{over}}}{q} \tag{3.4}$$

where V_{over} is the overvoltage [53]. The overvoltage is the difference of breakdown voltage V_{break} at which the electric field is strong enough for Geiger discharge and the bias voltage V_{bias} at which the SiPM is operated

$$V_{\text{over}} = V_{\text{bias}} - V_{\text{break}} \quad . \tag{3.5}$$

To allow for photon counting, an array of G-APDs connected in parallel composes an SiPM. They are small, electronically and optically isolated G-APDs each having a quenching resistor in series [51]. This leads to a quasi analogue output signal which can either be quantified by pulse observation or by integration of the pulse. As all single cell breakdowns have the same signal characteristics, all pulses with the same amount of cell breakdowns have the same size. Furthermore, the signal heights of breakdowns add up, meaning that e.g. the pulse of two cell breakdowns is twice as high as of only one, see fig. 3.10a. Integration of the pulses leads to a spectrum of clearly distinguishable peaks, each corresponding to a certain number of cell breakdowns, see fig. 3.10b [52].

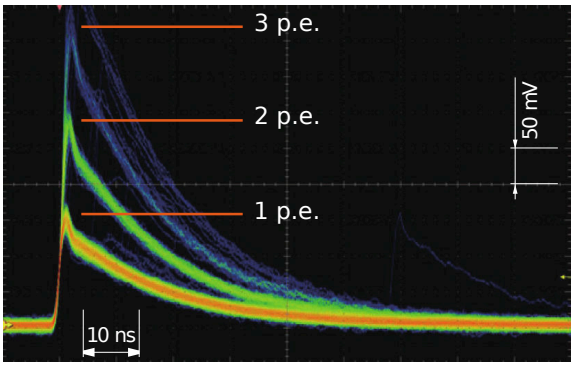

(a) Oscilloscope screenshot showing clearly distinguishable SiPM output signals.

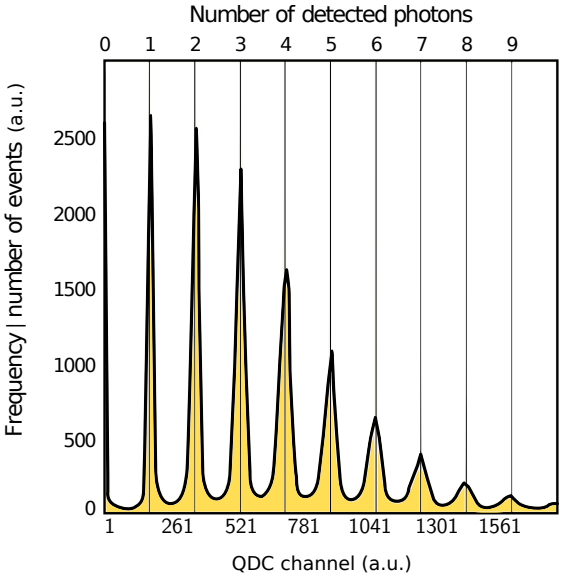

(b) Charge integrals result in the photoelectron spectrum with separated p.e. peaks.

Figure 3.10: SiPM pulse height characteristics. Depending on the number of cell breakdowns, the output levels to a characteristic pulse height which is measureable in photo equivalents (p.e.). Adapted from [52] (3.10a) and [48] (3.10b).

SiPMs are characterised by certain performance characteristics. These are, among others, the photon detection efficiency (PDE), dynamic range, noise effects and temperature sensitivity.

The **photon detection efficiency** gives the probability for a photon hitting the active area of an SiPM to create a pulse in one of its cells. Thus, it is the ratio of detected photons over the number of incident photons and is calculated with

$$PDE(\lambda, V_{\text{over}}) = QE(\lambda) \cdot \epsilon(V_{\text{over}}) \cdot F \tag{3.6}$$

where $QE(\lambda)$ is the quantum efficiency, i.e. the probability for a photon to create a charge carrier pair which depends on the wavelength λ of the incident light, $\epsilon(V_{\text{over}})$ is the avalanche initiation probability depending on the overvoltage, i.e. the probability that a charge carrier initiates an avalanche process, and F is the fill factor. The fill factor F is the active part of a pixel's area and always smaller than 1 due to e.g. inter-pixel wiring which diminishes the active surface and increases the separation of the cells [53]. The PDE ideally matches the emission spectrum of the WLS fibre, see fig. 3.7b.

The **dynamic range** is the scope over which an output signal is provided such that the size of the input signal can be reconstructed and is defined by the number of cells N_{cell} and the PDE. Under the assumption that the number of incident photons N_γ arrives in an infinitesimal amount of time and uniformly in space, the average number of fired cells can be expressed with

$$N_{\text{fired}}(N_{\text{cell}}, V_{\text{over}}, \lambda) = N_{\text{cell}} \cdot \left(1 - \exp\left(-\frac{PDE(V_{\text{over}}, \lambda) \cdot N_\gamma}{N_{\text{cell}}}\right)\right) \tag{3.7}$$

[53]. Hence, saturation occurs for $N_\gamma \cdot PDE \to N_{\text{cell}}$.

Noise effects alter the signal output of SiPMs to higher rates and higher pulses. Their characteristics are the same as for photon initiated signals. Thus, noise is statistically superimposed to the wanted signal and only estimations of their contribution are possible. Therefore, the events causing cell breakdowns are referred to as photo equivalents (p.e.) to include both photons and noise. An undesired increase in the rate of an SiPM is mainly caused by **thermal noise**. Here, thermally excited electrons are the initiators of an avalanche in a cell. Their occurrence follows a Poissonian distribution in time and can thus not simply be subtracted from the signal [51]. Their impact can drastically be reduced by setting a trigger above the single p.e. level. The dark count rate depends on temperature, bias voltage, cell size and the overall detector area. A further addition to the rate is caused by defects in the silicon lattice. During a cell breakdown, an electron can be trapped within the lattice and may be released only after the cell has recharged, thus causing another cell breakdown. This effect is known as **afterpulsing** but is negligible for state of the art SiPMs [51]. Besides the effects changing the pulse rates, **optical crosstalk** affects the pulse height. During an avalanche, charge carriers emit photons when recombining with their counterparts or in the acceleration process itself. Some of these photons emerge from the cell and are transmitted into a neighbouring cell creating a new avalanche process. The second cell breakdown is instantaneous and increases the overall output signal of the SiPM. Thus, the crosstalk probability for the dark noise can be determined by the ratio of the count rate above the 1.5 p.e. pulse to the count rate of 0.5 p.e.. It can be approximated with a binomial distribution [54]. For high crosstalk probabilities it converges into a Poissonian distribution [55]. The main dependencies are on the overvoltage and the distance between the cells. All noise effects are summarised as dark counts.

Most of the performance characteristics of an SiPM are temperature dependent. In

case of the noise effects, the thermal noise and hence the dark noise rate increases with temperature. To describe the contribution correctly, the dependency is given by the manufacturer for each SiPM type. Also the breakdown voltage of an SiPM is affected by temperature. With increasing temperature, lattice vibrations get stronger. Charge carriers interact more easily with the crystal whereby their acceleration process is impeded. Hence, ionisation processes are inhibited. This has an impact on the gain, PDE and timing of SiPMs. To overcome this phenomenon, the operation voltage has to be increased with rising temperature [53], see chapter 5.1.

In the Aachen Muon Detector, 64 SiPMs of type S12571-050P from Hamamatsu are installed (all technical data for S12571-050P is taken from [48]). Each has a photosensitive area of $1\times1\,\mathrm{mm}^2$ which was chosen to match the round size of the fibres of 1 mm diameter as good as possible. Since only square SiPMs exist, the edges protrude. It consists of 400 pixels where each has a pitch of 50 µm. The fill factor amounts to 62%. For the specific SiPM type deployed, the gain measures $1.25 \cdot 10^6$ at 25°C with a gradient of $+2.7 \cdot 10^4/°\mathrm{C}$. The breakdown voltage is $65 \pm 10\,\mathrm{V}$ and the recommended overvoltage 2.6 V. For temperature compensation, the bias voltage has to be adjusted with a coefficient of 60 mV/°C. The noise level of SiPMs is relatively high. Precisely, the S12571-050P has a dark count rate of 100 kcps (cps=counts per second) at 25°C. Additionally, it rises by 50% for every increase of 10°C. The SiPM's spectral response ranges from 320 to 900 nm which makes them well suitable for the slightly shifted fluorescence spectrum of scintillator tile and WLS fibre. At the maximum at λ=450 nm, the PDE amounts to 35.6%.

Compared to the classic photo-sensor choice, the photomultiplier tube (PMT), SiPMs carry certain assets and drawbacks. A disadvantage is the noise level which is much higher for SiPMs. The gain of PMTs and SiPMs is similar. Advantages include the compact size of SiPMs and the operation with much lower voltages. Additionally, the PDE outperforms state-of-the-art PMTs. Further advantages of SiPMs include their insensitivity for magnetic fields and their resistance to mechanical shocks and accidental light exposure.

For each tray in the AMD detector, eight SiPMs are required, one for each tile. They all sit on a carrier board at one end of the tray which was developed within this thesis and produced by the electronic workshop of III. Phys. Inst. A, RWTH Aachen, see fig. 3.11. Both high voltage and data readout connections are provided on the board. The supplied voltage amounts to about 70 V which is stabilised by two consecutive low passes. Coaxial cables conduct the signal on to the readout board. The temperature is continuously monitored by a 1-wire temperature sensor on the board to guarantee the readjustment of the operation voltage, see chapter 5.1.

3.4 Signal Processing

The electronics for signal processing have to fulfill the given spatial (mechanical housing) and electronic (supply voltage of SD batteries) limitations. Additionally, the readout of SiPM signals requires dedicated processing electronics. Hence, in the Aachen Muon Detector, "Extended Analogue Silicon pm Integrated Read Out Chip"(EASIROC) boards are integrated. These were specially developed for the readout of SiPM detectors by Omega Micro at CNRS-IN2P3-Ecole Polytechnique [56, 57]. The voltage supply for SiPMs and EASIROC board is regulated by a dedicated power supply unit.

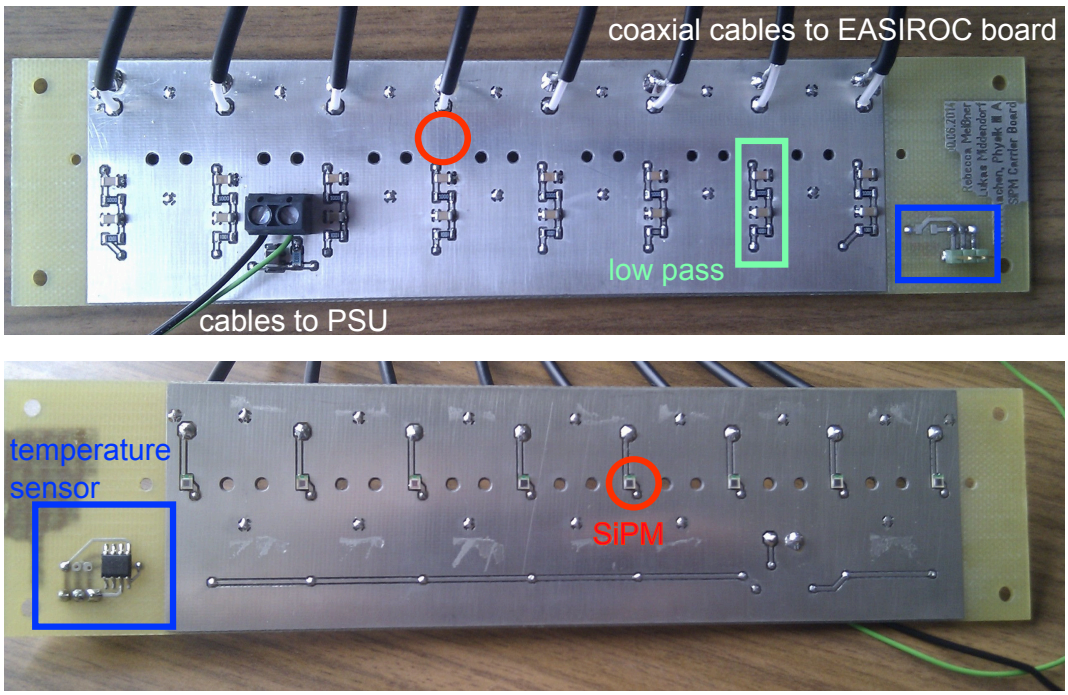

Figure 3.11: Photo of the back and front of SiPM carrier board. The SiPMs sit on the front and the electronics (low passes) and connections (coaxial cables to EASIROC, HV supply) on the back.

3.4.1 Power Supply

Both SiPMs and the EASIROC boards require a stable power supply. For this reason, a power supply unit (PSU) was built by the electronic workshop of the III. Phys. Inst. A, RWTH Aachen, see fig. 3.12. The external specification for the input voltage is given by the voltage supplied by the SD tank batteries which each have 12 V [22]. By connecting the batteries in series, 24 V are available. A step-down converter on the PSU provides a voltage of about 6.5 V for the EASIROC board and a step-up converter regulates the voltage to about 70 V for the coarse setting of the operation voltage of the SiPMs. The temperature on the PSU is monitored on top of the operational amplifier doing the bias voltage regulation to check for temperature stability, see chapter 5.3.

3.4.2 Readout Board

The EASIROC was designed as a front-end application-specific integrated circuit (ASIC) for the readout of SiPM pulses and gain adjustment. An incoming SiPM signal is amplified and processed within the ASIC to determine the pulse height of single pulses or the sum of multiple pulses in a short time window and the output is digitised. A total of 32 channels can be read out in parallel or individually and the gain of each SiPM can be trimmed separately. All channels are identical in construction. One common discriminator is available for threshold setting. The EASIROC is configured with an internal memory, the slow control, which serves i.a. for setting the gain, the DACs values and to switch on and off single features.

The EASIROC allows for gain adjustment of each SiPM by fine tuning their bias voltages. This is performed by uplifting the ground level of the SiPMs, see fig. 3.13.

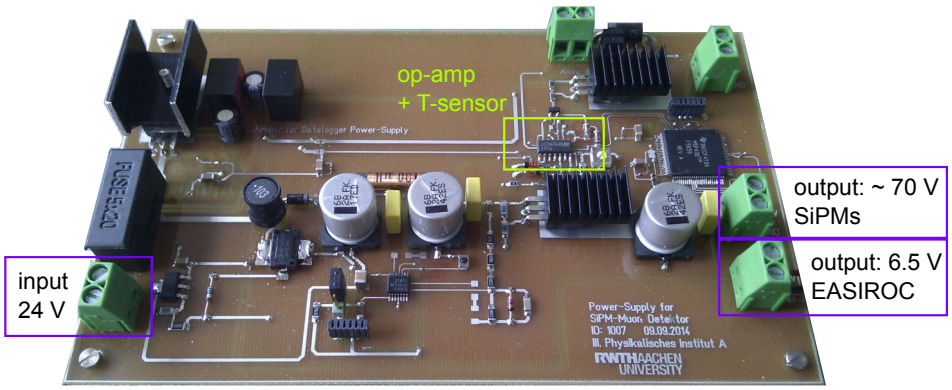

Figure 3.12: Photo of the power supply unit. The SD battery or an equivalent voltage source serve as input. An output is for the supply for the SiPMs and another for the EASIROC evaluation board. The temperature is monitored on top of the operational amplifier.

Thus, the applied voltage to the SiPMs by the PSU is reduced. One internal 8-bit DAC for every channel enables to vary the bias voltage in a range from 0 to 4.5 V with an external reference source. The range is decreased to a smaller interval from about 2.5 to 4.5 V by adjusting an external resistor at one of the EASIROC pins. Consequently, the voltage steps become smaller and a higher precision in equalising the gains can be achieved. To cover the full 4.5 V range, an additional internal reference source is available besides the external one. It covers the voltage range between 0 and 2.5 V. The required reference source is set by a slow control bit [57].

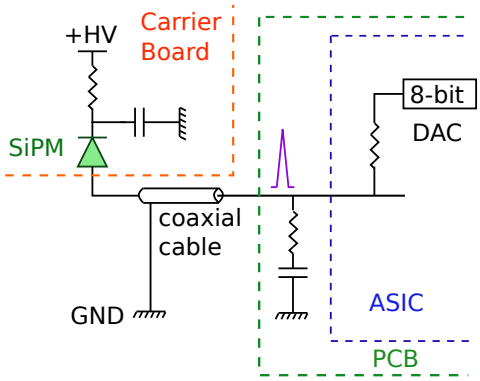

Figure 3.13: Scheme of how the SiPMs are connected to the ASIC / printed circuit board (PCB). The bias voltage is applied to the SiPMs over low passes to keep it stable. Fine tuning is achieved by adjusting the ground level via an 8-bit DAC on the ASIC. Adapted from [57].

The EASIROC provides a trigger output over a dedicated signal chain. A high-gain pre-amplifier is used and a fast shaper forms the signal with 15 ns peaking time. Hereafter, a discriminator compares the shaped signal to a threshold. This is set by an internal 10-bit DAC which is common for all 32 channels. The digital output of the discriminator is available either as OR32 which is a cabled OR of all channels or as a 32-bit trigger output T[31:0] which writes out each of the 32 channels discriminator status on a pin [57].

The readout of SiPM signals can be performed with a high gain and a low gain

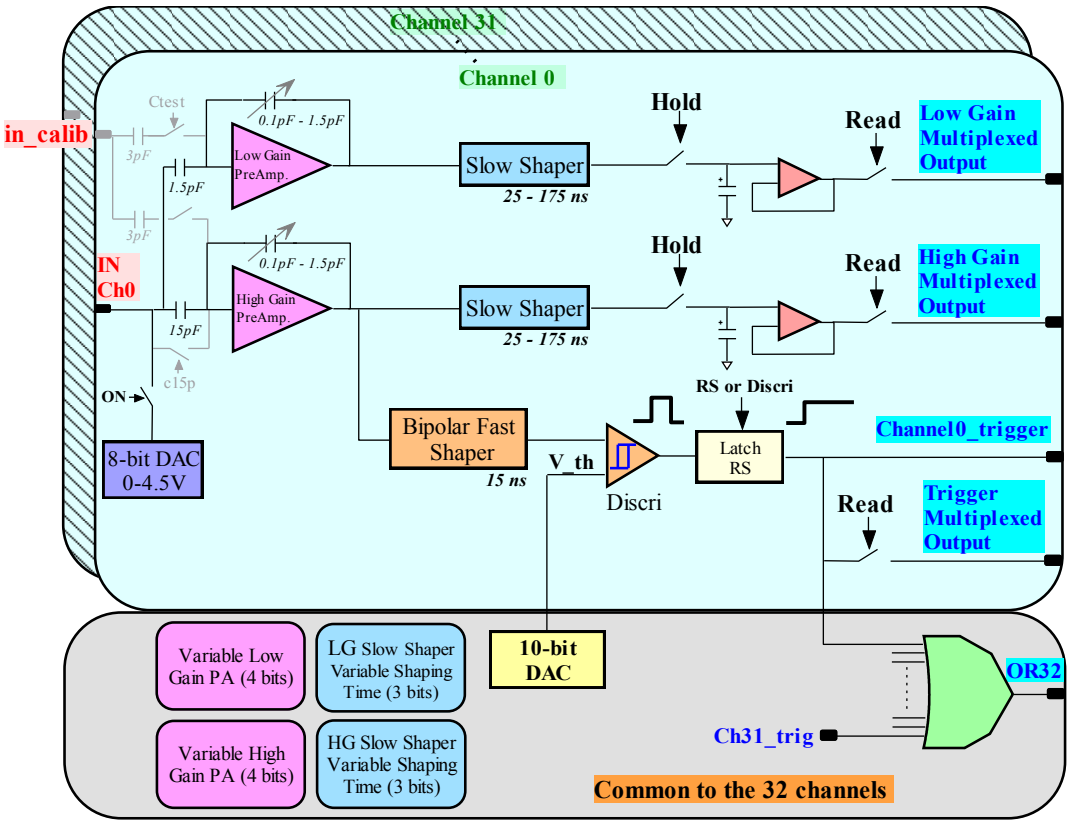

Figure 3.14: Schematic of one channel of the EASIROC. Taken from [57].

chain. Each chain is composed of a pre-amplifier, an adjustable shaper and an analogue memory in form of a track and hold cell. Both pre-amplifiers are tunable with 4 bits, see fig. 3.14. The gain control value of one pre-amplifier is variable in a range of 1-15 (high gain chain) and the other can be set between 10-150 (low gain chain). Here, the control value is defined as the ratio of the two capacitors of the pre-amplifier (see fig. 3.14) and are hence nominal gain values. The actual amplification factors are inverse to the control value. Thus, a small control value corresponds to a high amplification factor. The exact factors have to be determined with measurements. These setting options enables charge measurements in a dynamic range from 160 fC to 320 pC, equivalent to 1 photo electron (p.e.) to 2,000 p.e. assuming an SiPM gain of about 10^6 [57]. Both chains work in parallel but which chain is used for the data readout and to which value the pre-amplifier is set depends on the application. The amplified signal is fed into an integrating slow shaper. The shaping or peaking time is variable between 25 and 175 ns with 3 bits. By choosing high peaking times, the output becomes independent of the specific form of the input pulses. Specifically, this means multiple pulses separated in time shorter than the shaping time deliver the same output as one single peak of the according number of photo electrons. Furthermore, the shapers reduce the noise level. When the signal reaches its maximum, the amplitude is saved by a track and hold cell. For this purpose, a hold signal is provided externally by the field programmable gate array (FPGA). Ideally, it holds the signal at the time the peak reaches its maximum using information provided by the trigger discriminator of the fast shaper chain. Subsequently, a read module with shift register activates the data readout of the track and hold cells channel-by-channel using an analogue multiplexer and an external ADC digitises the amplitude. Here, the

maximum readout speed is 2 MHz [57].

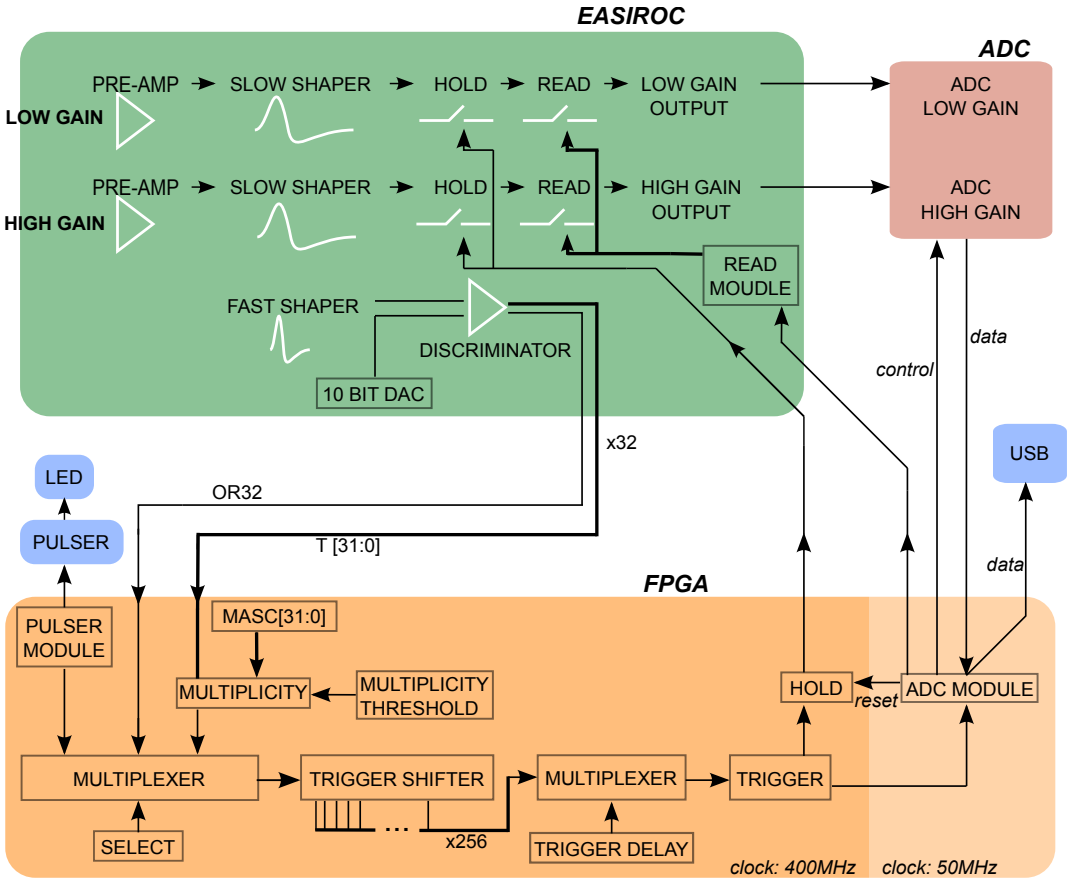

Figure 3.15: Schematic of the interplay of EASIROC, FPGA and ADCs on the evaluation board. Adapted from [57] (EASIROC) and [58] (FPGA)

The EASIROC itself is integrated in an evaluation board which had the original purpose of characterising the chip, see fig. 3.15 and fig. 3.16 [56]. Thus, many easy access points to the EASIROC output are provided on LEMO plugs. For plugging the SiPMs onto the printed circuit board (PCB), male HE13 connectors are provided. Furthermore, the PCB includes the two 14-bit ADCs for the high and low gain circuit. For the communication with the EASIROC (setting the hold and read signal and the slow control) and temporary data storage, a FPGA is accommodated on the PCB. Between EASIROC and FPGA a digital serial link allows the control of the slow control and a parallel link is established for the data transfer of triggers and hold signals. Data transfer between evaluation board and PC works via mini universal serial bus (USB).

A firmware for the FPGA [58] enables the data readout of the EASIROC and the controls the hold and read signals. The discriminator outputs (OR32 and T[31:0]) are the input signals for the FPGA. In case of the T[31:0], the discriminator signal is linked to a 32-bit masc MASC[31:0] by a reducing OR which compares the discriminator output (1 or 0) with the masc. The MASC[31:0] selects the channels of interest (bit value = 1 for corresponding bit) and if both the MASC[31:0] and the T[31:0] have positive output (1 for both), the positive signal is passed to the multiplicity. A multiplicity threshold counts the number of positive outputs of the multiplicity. Thus, coincidence triggers of multiple channels can be set by selected the corresponding channel in the MASC[31:0] and writing the number of the channels into the multiplicity threshold.

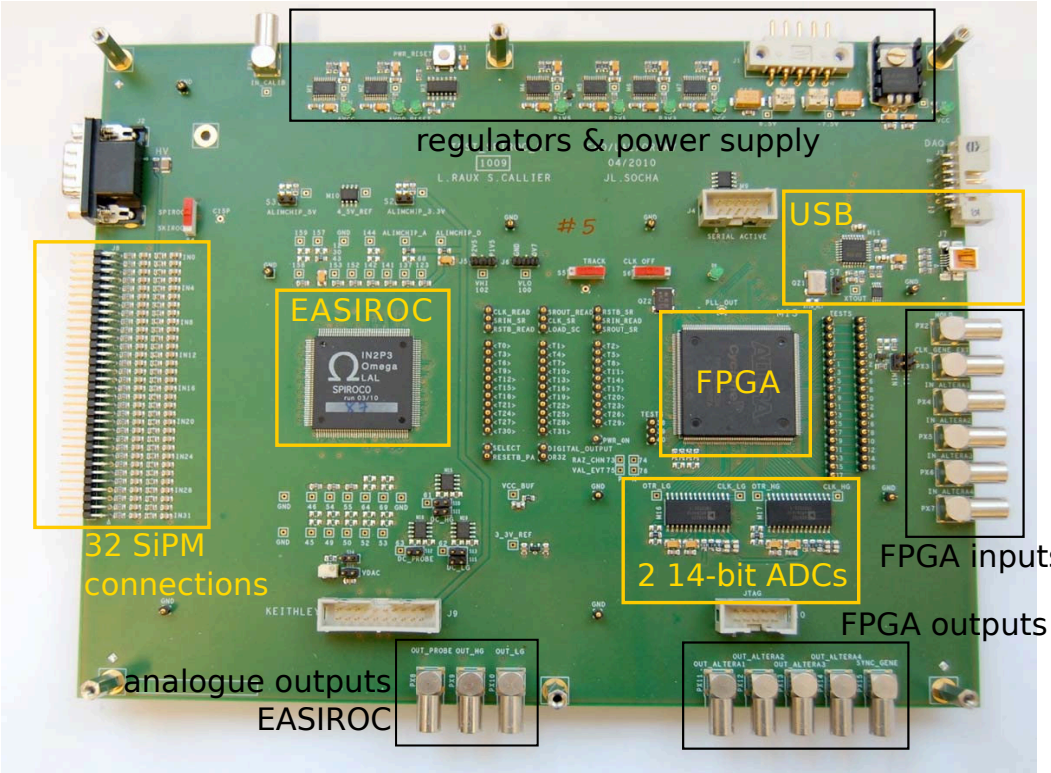

Figure 3.16: Photo of the EASIROC evaluation board. Marked in orange is the processing chain as described in the text. In black are further features which are mentioned in the text. Adapted from [56].

A multiplexer in the FPGA gets the OR32, the multiplicity and optionally a signal of a pulser module as input and a select module provides the variable for determining which output is used. The selected signal is fed into a shift register with 256 steps. Each stage is passed into a second multiplexer through which the effective length and therefore the trigger delay can be chosen. Since the readout with the external ADCs takes time as it occurs channel-by-channel, the hold signal is sent to the track and hold cell of the EASIROC to keep the amplitude at peaking time. Furthermore, the trigger of the FPGA activates the ADC module. This sends the read signal to the EASIROC. Additionally, the ADC module controls the external ADC of the high and low gain circuit. After the data readout, the ADC module resets the hold of the FPGA. Thus, hold, read and digitisation signals are controlled by the same device and consequently match in time and order [56]. Since the digitisation dead time amounts to about 16 µs [56], the process is possible only once per air shower which produces a signal with approximately 1 µs duration in the AMD.

Determining the number of muons in an air shower is feasible by two different techniques. Either the fast shaper output is used and the number of positive discriminator outputs which exceed the thresholds is counted. This is only an option for low hit rates. Or the charge is integrated using one of the slow shaper outputs. Here, high hit rates can be processed. Depending on the hit rate using either the low or the high gain chain allow for overcoming saturation effects.

While the evaluation board as delivered consumes 2 W, the EASIROC itself was developed for low power consumption [56]. To reduce the wattage, unused features

can be disabled, the FPGA can be replaced by a newer model, low power ADCs can be installed and better voltage regulators (step-down converter instead of linear regulators) built in. Fixed contributions are the chip with 155 mW and each channel with 4.84 mW. Thus, power savings of about 1.25 W per evaluation board are feasible. Calculating the power consumption of the SiPMs and high voltage supply with 0.25 W, the total power needed amounts to 1 W per detector half.

Chapter 4

Light Conduction Subsystem

The light conduction system consists of the wavelength shifting (WLS) and optical fibre and two mechanical couplings which couple the optical light guide either to the WLS fibre or to the SiPM. The subsystem starts with the collection of light by the wavelength shifting fibre and ends with the coupling of the light onto the SiPM. The light yield critically depends on the quality of these components. Minimal changes in the setup or to the components themselves can already result in an increased or decreased output. Hence, the mechanical couplings are studied regarding their stability in holding the optical fibres at a fixed position. Furthermore, the WLS and optical fibres are exposed to varying temperatures to check for decreasing quality effects. Already existing damages and impurities in the fibres at the moment of delivery are documented.

4.1 Mechanical Coupling

The transition of light between two fibre ends and the coupling of light into the SiPMs require a stable positioning of the fibres. Ideally, the fibres are coupled with their ends exactly aligned to each other without gap or aligned with the SiPM with the greatest possible match of sensitive area of the SiPM and outlet area of the fibre. This scenario is usually not achieved due to intrinsic mechanical limitations of the components. Polishing effects of the fibres can cause non perfectly flat surfaces. Additionally, the coupling mechanism generally causes a small spacial distance between the components. This reduces the light output. To keep the light yield at a stable level and thus describable, the couplings have to hold the fibres at fixed positions, i.e. in constant distances and at immovable planar orientation.

4.1.1 Requirements and Design

The couplings are points of light transitions with potentially high light losses. Thus, mechanical couplings reducing the light loss to a minimum are developed in cooperation with the mechanical workshop of the III. Phys. Inst. A of RWTH Aachen University. This includes that the couplings allow for an accurate adjustment of the fibre's position, both in height and in the planar orientation. Additionally, a tight mounting has to ensure that vibrations of the whole detector or single components do not change the position of the fibre and the output remains stable.

Fig. 4.1 shows the technical drawing of the mechanical coupling between an optical fibre end and an SiPM located on the SiPM carrier board. The distance in between the SiPMs on the board was specifically chosen under the spacial requirements of the coupling and amounts to 2 cm. In fig. 4.2 a photo of the single components of the coupling is shown.

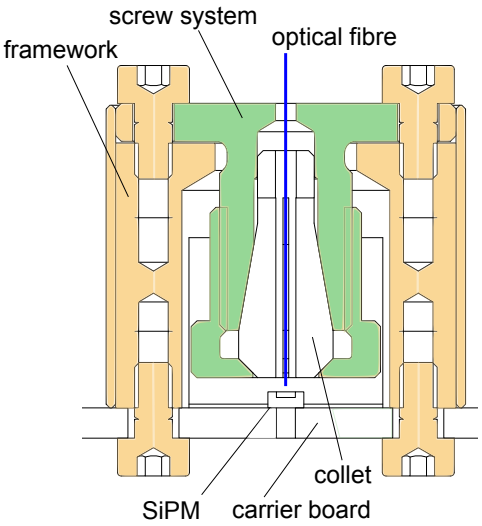

Figure 4.1: Technical drawing of the mechanical coupling between optical fibre and SiPM and attachment to the SiPM carrier board [59].

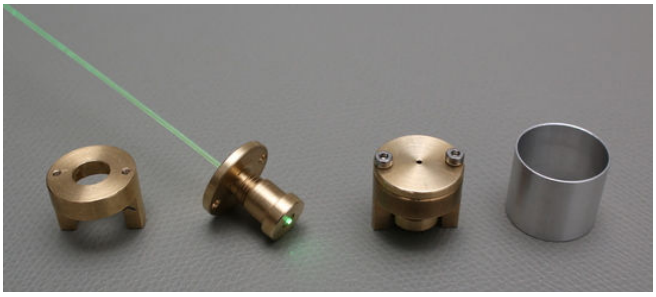

Figure 4.2: Components of a mechanical coupling between optical fibre and SiPM. From left to right: Metal framework for positioning of the fibre, screw system (here with WLS fibre for better visibility), screw system inserted into metal framework, aluminium ring for light tightness.

The mechanical coupling between WLS fibre and SiPM consists of a metal framework, screw system, collet and aluminium ring, see fig. 4.2. The purpose of the metal framework is to mechanically attach the coupling to the SiPM carrier board and ensure the correct positioning. A screw system with collet inside fixes the optical fibre at a specific height above the SiPM. By turning the system, the collet opens or closes. When closing the collet, the fibre is slightly pulled away from the SiPM. Since this is an undesired effect, the mechanical coupling is currently being improved. A new version will also simplify the alignment of the components. Small set screws allow for the fine adjustment of the optical fibre in the horizontal plane above the SiPM, see fig. 4.3. An aluminium ring can be put over the coupling to reduce stray light and avoid crosstalk between the different couplings.

The coupling between the WLS and optical fibre differs only slightly from the one between fibre and SiPM. Only the metal framework is different so it can be attached to the scintillator tile (see fig. 4.4) and the orientation of the screw system with collet is inverted. Thus, when tightening the system, the optical fibre is slightly pushed towards the WLS fibre in the tile. Hence, this has to be taken into account by leaving a small space before the closure.

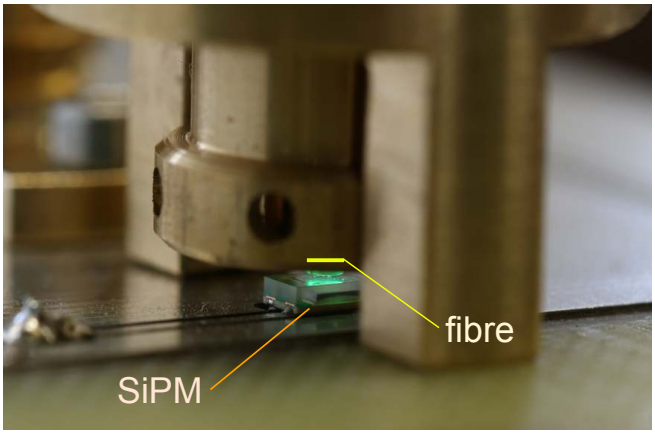

Figure 4.3: Fine adjustment of the fibre onto an SiPM. A WLS fibre is used for easier fine tuning due to better visibility. The width of the horizontal yellow line indicates the diameter of the WLS fibre below.

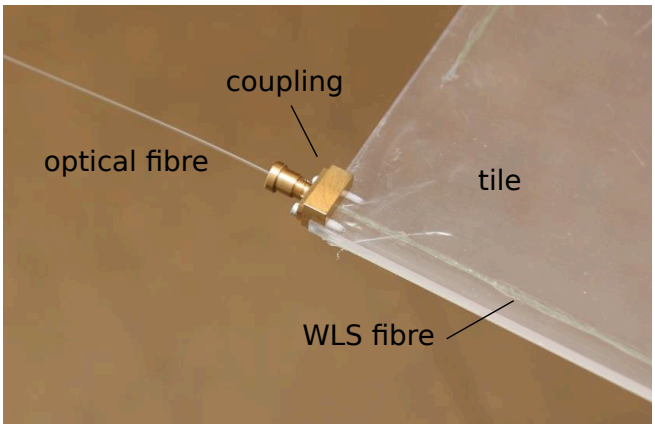

Figure 4.4: Mechanical coupling between two fibre ends. The coupling is attached to a scintillator tile.

4.1.2 Stability Under Stress

During the deployment and the operation of the Aachen Muon Detector, the system is exposed to vibrations. Since changes in the position of the coupled fibres relatively to each other or to the SiPM result in a non quantifiable decrease of the light yield, its stability has to be ensured under stress. Therefore, a test stand is developed for stress measurements. A photo of a similar test stand is shown in fig. 4.6 (equal except neither tube nor temperature sensor is installed). A superbright 5mm-LED in the blue to UV range from Lumitronix (article number 15401) [60] is powered by a sourcemeter. The light is coupled into an integrating sphere by one of its inputs. A WLS fibre protrudes into an output of the sphere. Since the coupling between two fibre ends can only be mounted onto a tile, the WLS fibre is glued into a piece of acrylic glas. The position of the acrylic glas is fixed in the setup to avoid movements or fluctuations from this part of the setup. Coupled onto the WLS fibre is an optical fibre. The middle part of the clear waveguide can be moved freely. Its second end is fixed within a mounting which in turn is locked within the setup. The end itself is aligned with a pin diode which detects the light. The readout is performed with a picoammeter.

Approximately every second the current value is read out. This value is an internal average of 10 measurements of the picoammeter to reduce fluctuations. Only variations in the current trace are of interest. The absolute value depends on many factors of the setup unimportant for the result such as the brightness of the LED and the distance between optical fibre end and pin diode. A slow increase in the output current may occur due to the LED which slightly changes its brightness with time.

During a measurement run, the optical fibre is grabbed close to the mechanical coupling and either pulled straight away from it or vertically shaken. These stresses occur at a specific time interval making it possible to allocate the times of stress to the according points in the trace. The results are plotted in fig. 4.5. Times of stress are marked with arrows. Clearly visible are the spikes within the otherwise constant trace. When comparing these to the points of stress, a coincidence is identifiable. The changed output only occurs while manipulating the fibre's position. Further test runs are performed where the fibre is only touched (always with gloves) but not moved in any direction. Neither spikes nor smaller peaks appear in the trace. Thus, the effect originates from a relative position change of the end of the optical fibre in the coupling only. The position and hence the output change is completely reversible. Whether the fibre is pulled or shaken makes no qualitative difference.

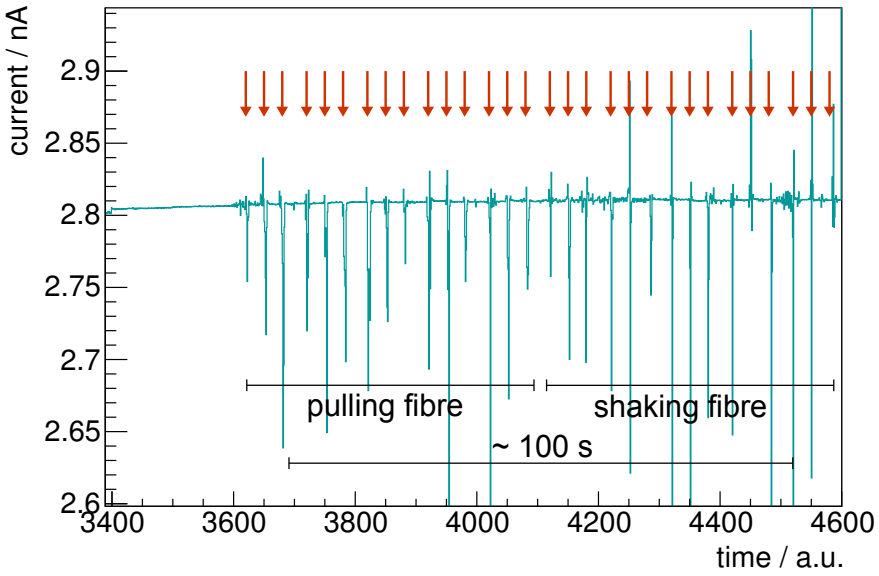

Figure 4.5: Stability test results of the mechanical coupling. Points of stress are indicated by orange arrows. The spikes in the trace coincide with these points. Whether the fibre is pulled away from the coupling or shaken makes no visible difference in the output.

Consequently, stress changes the light yield of the system but only at the very moment of its occurrence. The position of the fibres recovers completely by itself and the light yield with it. Thus, the mechanical coupling is suitable for the purposes of the Aachen Muon Detector.

4.2 Temperature Dependent Light Output of Fibres

When applying a detector outdoors, it is subject to many external influences, such as temperature variations. In the Pampa Amarilla, the components of the detector are exposed to a temperature range between -15 to +50°C. The installed electronics temperature dependences are quantified in chapter 5 and subsequently implemented in measurements and analysis programmes and thus corrected for. Whether irreversible fibre damages are to be expected is tested with a similar test stand as in chapter 4.1.2.

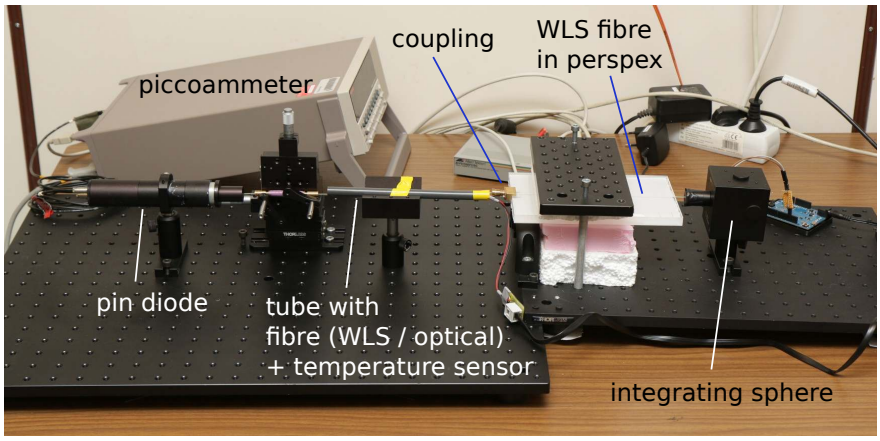

Figure 4.6: Test setup for stability measurements of the mechanical coupling (without tube and temperature sensor) and light output measurements of fibres.

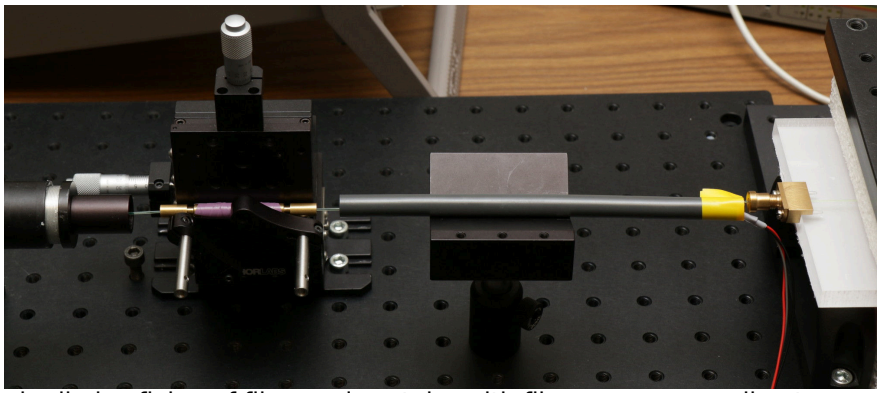

Figure 4.7: Detailed view of the test setup from (right to left) mechanical coupling to tube with temperature sensor and fibre (WLS or optical) to pin diode.

The test setup is only changed slightly by inserting a plastic tube of 15 cm length and a diameter of approximately 1 cm, see fig. 4.6. The previously freely movable clear waveguide is put through the tube together with a temperature sensor which sits in the middle of the pipe, see fig. 4.7. During the measurement, the plastic tube is either exposed to a cooling cycle by use of a freezer spray or a heating cycle by use of a hot air blower. With the fibre and sensor inside the tube, an easier targeting is facilitated and the fibre is not directly exposed to the sources. Additionally, the cold or heat is stored in the tube for a while rather than only observing an effect at the moment of cooling

or heating, respectively. Plastic was chosen as material to decelerate the heating and cooling process. Furthermore, the temperature sensor may have contact to the tube which implies that the sensor is influences by the tube's temperature. For plastic, this effect is smaller than for metal.

The data taking process functions with the exact same programme as in chapter 4.1.2. After the LED and the picoammeter are turned on, the programme is started. Firstly, only the current trace at room temperature is observed for a while to measure the light output level at stable conditions. Then, the tube with fibre and temperature sensor is cooled down with a freezer spray to about +4°C (the room temperature and the amount of freezer spray available sets limits to the cooling process). Subsequently, the system reheats itself back to room temperature. Data points are taken constantly. For switching from cooling to heating process, the measurement is shortly interrupted to change from the freezer spray to the hot air blower. Within the next measurement run, the system is heated up to about 58°C. The system cools down to room temperature and the measurement is stopped. Thus, the fibre is exposed to one temperature cycle.

The WLS fibre is replaced by an optical fibre and the measurement is rerun. Here, a temperature range between about -10 and 60°C is measured.

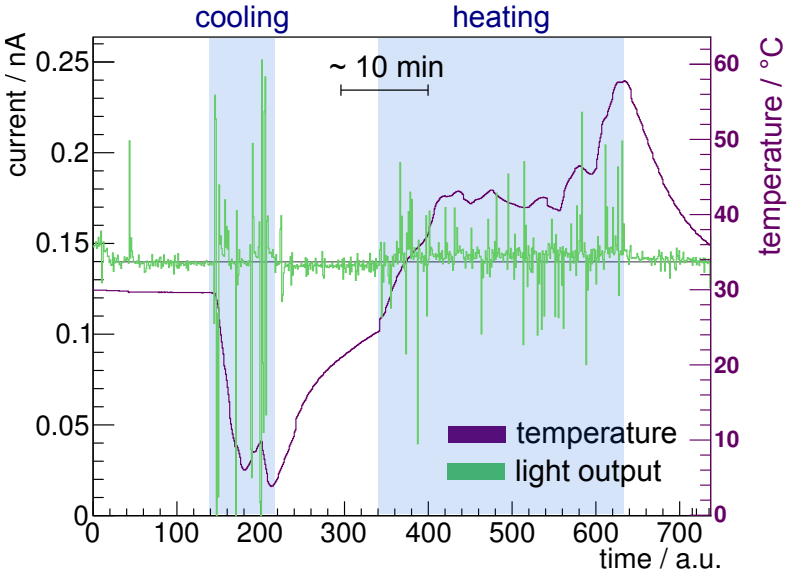

Figure 4.8: Light output of a wavelength shifting fibre exposed to one temperature cycle. Cooling and heating periods are marked in blue regions. During these periods of time, fluctuations in the current trace originate from movements in the setup.

Measurement results are shown in fig. 4.8. The light output measured in units of nA shows several peaks as already seen in fig. 4.5. These mainly occur during the cooling and heating process. Both processes cause air movement which in turn can produce movements in the setup. Thus, the position of the fibre in front of the pin diode or the alignment of the fibres fluctuates, as seen in chapter 4.1.2. The relative fluctuations in the trace of fig. 4.8 are higher than in fig. 4.5. This can be explained as several features influence the height of the fluctuations. These include for example ploishing effects (different exit and entrace areas and their realtive position change influence the light coupling degree), the coupling itself (i.e. the spatial distance between the fibres) and that first an optical and then a WLS fibre is used. Additionally, the pin diode can be influenced by the heating and cooling processes as the application of the freezer spray

and the hot air blower occurred in complete darkness which makes exact targeting at the tube difficult. This explanation is supported by the periods without cooling or heating with significantly less fluctuations. The overall trend of the trace shows a stable output. Hence, the light output and conduction properties of the WLS fibre after one temperature cycle is unchanged. The results for the optical fibre are similar. No changes in the current trace beside the fluctuations during heating and cooling cycle are observed.

Summarising, the charactersistics of WLS and optical fibre after one temperature cycle are constant. The test setup makes a high number of repetitions unpractical since the cooling and heating of the tube happens manually. Additionally, an alternative to freezer spray has to be found as multiple cooling cycles are very material consuming. Thus, the first tests with one temperature cycle are promising but for a complete exclusion of temperature damages to fibres, further tests are essential. Furthermore, additional tests regarding the temperature dependence of the light yield of the WLS fibre are required.

4.3 Documentation of Fibre Damages and Impurities

The quality of the fibres is one of the factors which essentially determines the light yield. Any kind of damage is origin of light loss in the output. Since the damage differs from fibre to fibre, quantitative predictions about the impact are hardly possible. But damage has to be considered when comparing simulations which usually imply perfect fibres with measurements as one reason for differing results. Thus, types of damages in fibres are documented to prove the deviation from ideal fibres.

Fibres have been photographed before and after the polishing and after several mounting cycles. Before polishing the fibre, both cladding and output area exhibit structural roughness, see fig. 4.9a. Afterwards, the light output area is flat without any visible structural deviations. In turn, the cladding close to the fibre end can break during the process, as seen in fig. 4.9b. The severity for this effect varies, a fibre with no visible cladding damage is shown in fig. 4.9c.

The protruding cladding can break off completely when mounting the fibre in a mechanical coupling. Additionally, the insertion or removal of the fibre into or from the coupling can further damage the cladding of the fibre and the output area, see fig. 4.9d. Thus, once installed in the final detector, the clear waveguide is ideally not removed again for other than replacement works.

Besides the damages close to the fibre ends, impurities are observed all along the fibre claddings and cores, see fig. 4.10. Already just delivered fibres show these impurities. Again, their severity and amount vary. Hence, the output of equally long fibres can be different due to these effects.

Unless no improved polishing method or alternative solution for smoothing the fibre end's surface is found, the light loss has to be taken into account. Also the impurities within the fibres are origin of a reduced light yield. For the final application of the Aachen Muon Detector, each readout chain has to be calibrated to quantify the light yield and output of each channel. A short measurement is desirable due to the amount of chains. Since other components such as the mechanical coupling cause deviations as well (the spacial distance between fibres differ), such a measurement includes all light loss effects at once.

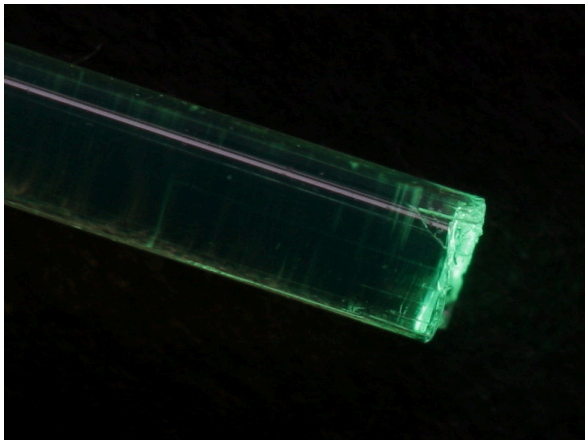

(a) Unpolished fibre.

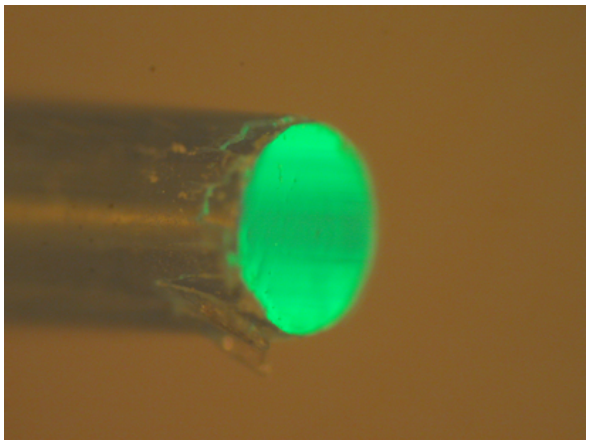

(b) Polished fibre with damaged cladding (microscopic view).

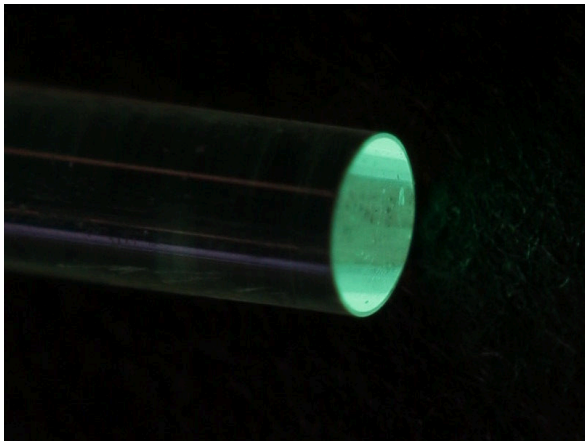

(c) Polished fibre with no visible structural roughness.

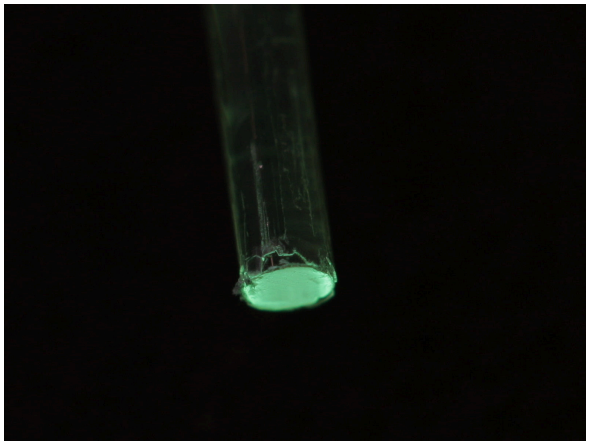

(d) Fibre damages after putting it into and out of the coupling several times.

Figure 4.9: Fibre ends at different states of treatment from unpolished to polished to used.

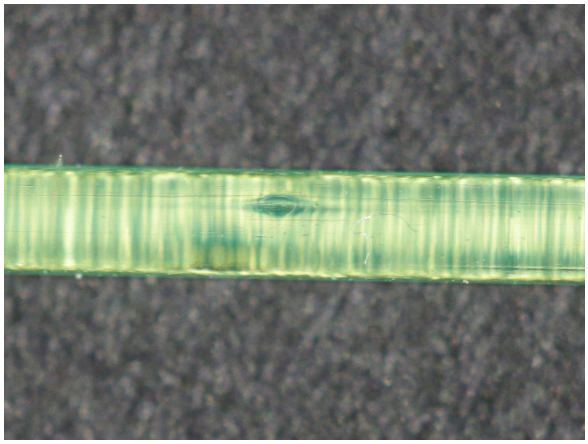

(a) Photo of an impurity in the cladding.

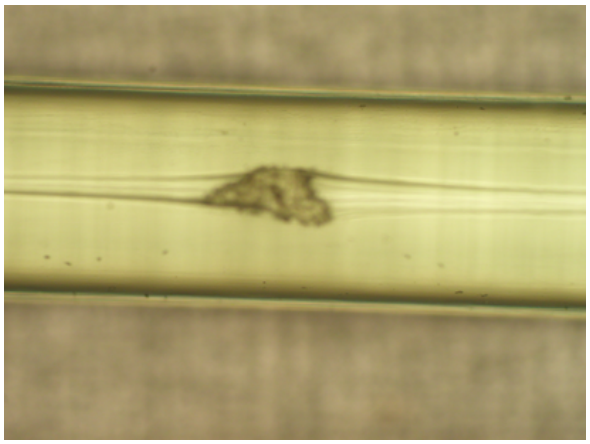

(b) Microscopic view of an impurity in the fibre core.

Figure 4.10: Impurities in the fibres are observed in delivered fibres and can occur in the cladding or core of the fibre. Their severity varies for all fibres.

Chapter 5

Electronics Characteristics and Temperature Dependencies

The operation of the Aachen Muon Detector (AMD) requires a full analysis of the electronics installed. This includes the silicon photomultipliers (SiPMs), the Extended Analogue SI-pm ReadOut Chip (EASIROC) evaluation board and the power supply unit (PSU). Besides characterising the output of the power supply and readout chain, a stable operation under temperature variations has to be guaranteed both for the SiPM operation voltage stability and for the correct signal threshold setting for the operation of the AMD. Detailed requirements for SiPMs and the threshold are given in chapter 5.1 and 5.2.2 and the importance of studied temperature effects of the EASIROC board and the PSU are discussed as part of their analysis in chapter 5.2.1 and 5.3. For all components the operation has to be stabilised within a temperature range between -15°C and +50°C, which are the variations of the ambient temperature in the Pampa Amarilla [27]. Flow charts for the subsequently described characterisation and analyses procedures are given as summary in chapter 5.4.

5.1 Silicon Photomultiplier Temperature Control

The response of silicon photomultipliers (SiPMs) is temperature dependent. Characteristics like dark count rate, cross talk, gain and breakdown voltage vary (c.f. chapter 3.3). The dependence of the dark count rate cannot be corrected for, but dedicated measurements of the background rate of the whole setup quantify these effects (c.f. chapter 5.2.2). All other characteristics can be stabilised by adapting the operation voltage of the SiPMs with temperature. For this reason, the manufacturer, here Hamamatsu, states the optimal operation voltage for each SiPM along with a temperature correction factor for each device. The operation voltages U_{op} for the installed SiPMs are given in table 5.1 for 25°C. They have been chosen out of a series of the delivered SiPMs such that their optimal operation voltages are nearly similar. The bias voltage is fine-tuned for each SiPM individually but a common voltage is applied to all SiPMs. Since the fine tuning is limited to a small voltage range which is equal for all SiPMs, different ideal operation voltages of the SiPMs require that part of the voltage range is used to correct for these differences. This entails a reduced fine tuning range.

The temperature correction factor for the breakdown voltage of the SiPMs amounts to $k = 60\,\mathrm{mV/°C}$. Applying this correction guarantees that SiPM characteristics are stable, except the dark noise. Consequently, the temperature adjusted bias voltage is calculated via

$$U(T) = U_{op} + k \cdot (T - T_0) \tag{5.1}$$

Serial Number	308	309	322	323	324	325	326	333
U_{op} / V	66.44	66.58	66.60	66.58	66.43	66.47	66.60	66.60
Position	2	4	6	5	1	3	7	8

Table 5.1: Serial number, ideal operation voltage and position on the carrier board (left to right) of the installed SiPM of type S12571-050P. Values as given in the delivery sheet by Hamamatsu.

for each SiPM, with $T_0 = 25°C$.

One temperature sensor per SiPM carrier board is read out in regular time intervals. Adjustments in the bias voltage are calculated by the measurement programme on the PC and written into the slow control of the EASIROC. This enables a continuous regulation during the measurement and thus stable gain values.

Additionally, the supply voltage from the power supply unit is stabilised by low passes filtering out voltage fluctuations of higher frequencies. An overall control precision of 20 mV on the overvoltage of the SiPMs is to be achieved which corresponds to 1.5% of the overvoltage of 1.3 V.

5.2 EASIROC Characterisation

The Extended Analogue SI-pm ReadOut Chip (EASIROC) is one of the central elements in signal processing. It is installed on an evaluation board which also provides all other components for data processing which are subsequently described. The EASIROC processes the incoming signal pulses and passes on the data to the field programmable gate array (FPGA). Furthermore, it allows for bias voltage fine tuning of the SiPMs with an 8-bit digital to analogue converter (DAC) for each SiPM. For this purpose the EASIROC provides an external and internal reference source which differ in their voltage output ranges. The output voltage of the external source is modified by adjusting an external resistor at one of the EASIROC pins to a range from about 4.5 to 2 V. The internal source allows bias voltage fine tuning in a range from 2.5 to 0 V. Consequently, a fine tuning in the range between 4.5 and 0 V is possible.

Detailed analyses of the DACs' output for the bias voltage regulation and characterisations of the dark noise spectrum, threshold constraints, and additional noise effects within the scope of data processing are performed. This is a time consuming measurement procedure as the individual channels of the EASIROC board have to be tested for different behaviours not only under changing conditions but also among each other. Thus, besides the development of the procedure itself and the implementation for the present EASIROC test board, a flow chart is developed for future measurements of additional boards. It provides an overview of necessary measurements and tests which can shorten the procedure due to the adaption of previous results to other conditions, channels or even other EASIROC boards. First, the measurements are described and in chapter 5.4 the flow chart is given. Several of the subsequently described measurements were repeated at constant conditions to test on reproducibility. All results prove the reproducibility and are thus not further described in the analysis of data.

5.2.1 Calibration of DACs for SiPM Bias Voltage Regulation

The knowledge of the output voltage of the 8-bit DACs is essential for a correct bias voltage fine tuning. Hence, the output of all 8 bits of all 32 channels was measured. Furthermore, the EASIROC was exposed to temperature variations in a range from about 3°C to 51°C to quantify the effect on the output voltages. For this purpose, a temperature sensor is mounted on top of the chip. Both internal and external reference source have to be measured successively since they are independent of each other and can thus have a different behaviour.

Measurement Setup

The measurement setup consists of the EASIROC evaluation board, a FLUKE 8845A multimeter [61] and a 6.5 V power source which supplies the test board. Cables which have bunch plugs at one end and female 1/10" 32×2 pin header plugs on the other end connect the multimeter to the evaluation board at the output where the SiPMs are connected in detector operation mode.

The chosen reference source of the DAC (internal or external) regulates the voltage for the fine tuning. As the DAC can only sink current which the SiPMs are delivering from the high voltage but not source current, only a multimeter with a high impedance may be used to avoid that current flows from the power supply over the multimeter to ground. The FLUKE 8845A has an input impedance of 10 GΩ which is sufficiently high.

Measurement Procedure

For data acquisition, firstly the slow control of the EASIROC is configured. This includes the activation of the DACs of all channels. Additionally, the reference source is chosen. Finally, all 8 bits are switched off. Since switched-on bits reduce the DAC voltage output, this implies that the output is maximal. Subsequently to the configuration of the slow control, the multimeter is turned on and connected to the first channel of the evaluation board. The measurement is started and the first voltage value is read out. After the first data point is taken, the slow control is adjusted by increasing the DAC count by one. The new configuration is written into the EASIROC and the next data point is read out. Before each value is taken, a sleep time of 1 second guarantees that the voltage is stable. This procedure is repeated for all 256 steps per channel. Then, the multimeter is connected to the next channel and the measurement is rerun.

To allow measurements at different temperatures, the EASIROC evaluation board is placed inside of a cooling chamber. The COOLI was developed in the III. Phys. Inst. B of RWTH Aachen [62]. It enables temperature regulation in a range between approximately 0°C and 55°C for the environmental influences during data taking with the current setup. Depending on the outer temperature conditions the range can be enlarged in other measurements. Dry air circulation prevents condensation even at low temperatures. The cooling itself is regulated with several Peltier coolers within the box. For the characterisation of the DACs, measurements were taken at 15 different temperatures in the above mentioned range with steps of about 5°C for five of the 32 channels.

Data Analysis

For the analysis, the output voltage of each DAC step (which will later serve as bias voltage regulation) is plotted over the DAC count. Each DAC step corresponds to a voltage change of approximately

$$\frac{(4.5-2)\,\mathrm{V}}{256\,\mathrm{steps}} \approx 10\,\mathrm{mV} \tag{5.2}$$

which is about the value of bit 0, the bit with the smallest voltage output. The expected voltage output of the single bits increases exponentially within

$$U(bit) = 10\,\mathrm{mV} \cdot 2^{bit} = 10\,\mathrm{mV} \cdot e^{\ln(2)\cdot bit} \tag{5.3}$$

In fig. 5.1, a selection of different channels measured at the same temperature is shown. At DAC count 0 all bits are switched off and the output voltage is maximal. The curves of the channels vary which makes it necessary to characterise each channel individually. Steps in the otherwise linear behaviour can occur when single bits are switched on or off. This is explained by small deviations from an exponential increase in the output value of successive bits according to eq. 5.3, see fig. 5.2. The highest voltage difference measured between two DAC counts is channel dependent. Overall, the highest measured voltage step amounts to 100 mV at (20.2 ± 0.2)°C but usually does not exceed about 50 mV. Within the overall aim to reach an accuracy of 20 mV for the overvoltage this is a non negligible effect. But as theses steps are characteristics of the channels, no compensation is available. Critical quantities for the correct description of the output voltage are thus the maximal value at DAC count 0 and the value of each bit.

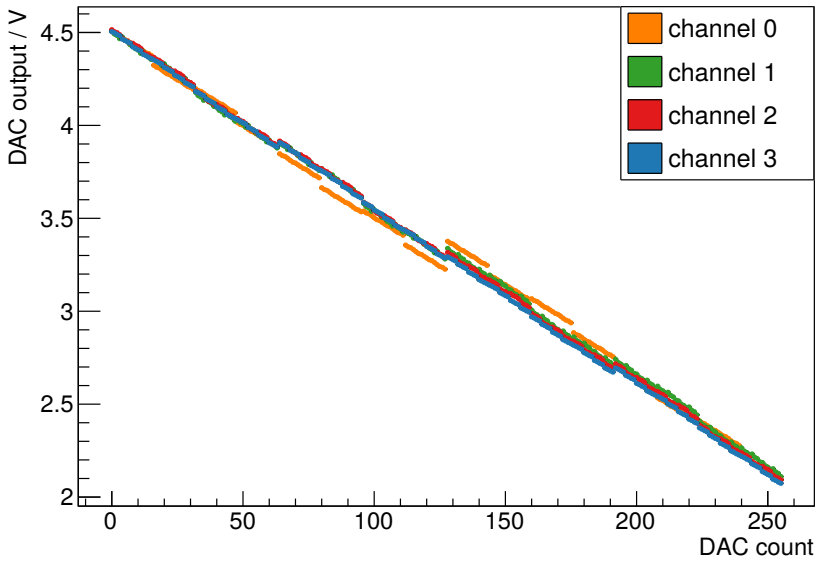

Figure 5.1: Calibration curves for the 8-bit DAC of the first 4 channels at $T = (26 \pm 0.2)$°C. The voltage output is maximal for DAC count 0 and subsequently decreases with increasing DAC count. The output of the channels vary, making a calibration of the bits for every channel necessary.

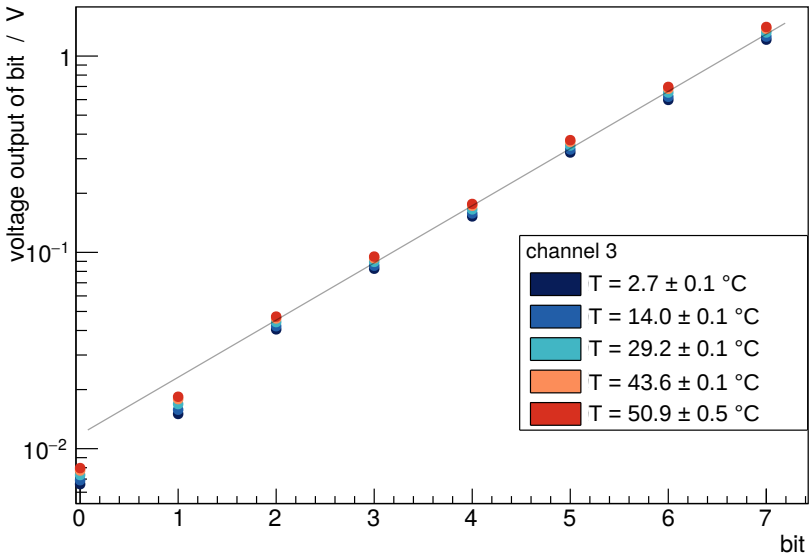

Figure 5.2: Voltage output of the single bits of channel 3. The increase deviates from the exponential expectation (according to eq. 5.3) which causes breaks in the calibration curve of the DAC. The value of the bits enlarges with increasing temperature. The grey line gives an approximation for an ideal exponential increase of the bit's output voltage.

The effects of the temperature variations are shown in fig. 5.2 and 5.3. In fig. 5.3, a dependency is observed in form of a steeper slope of the voltage output over DAC count for higher temperatures. The output difference at the maximal DAC step 256 amounts to about 0.5 V for a temperature difference of about 50°C. To reach an accuracy of 20 mV on the overvoltage of the SiPMs, a correction algorithm is essential for the operation of the detector with the EASIROC. Subsequently, the values of the single bits are calculated for this purpose and their temperature dependency is evaluated. Additionally, whether the maximal output voltage of the channels (equivalent to all bits switched off) depends on temperature is examined.

The temperature T_i is measured at each data taking point or DAC count i. Although the evaluation board is situated inside the COOLI, small temperature fluctuations occur of maximal 1°C. For the analysis, the mean of all temperature values T_i is taken, i.e.

$$T = \frac{1}{N_{\mathrm{DAC}}} \cdot \sum_{i=1}^{N_{\mathrm{DAC}}} T_i \tag{5.4}$$

where N_{DAC} is the number of DAC steps = 256. As uncertainty, half of the temperature spread T_{spread} is used to take into consideration that the temperature value for the respective DAC step does not necessarily comply with the mean. Also, the precision of the temperature sensor $T_{\mathrm{prec}} = 0.06°\mathrm{C}$ contributes to the uncertainty, giving

$$\sigma_T = \sqrt{T_{\mathrm{spread}}^2 + T_{\mathrm{prec}}^2} = \sqrt{\left[\frac{1}{2} \cdot (T_{\mathrm{max}} - T_{\mathrm{min}})\right]^2 + T_{\mathrm{prec}}^2} \tag{5.5}$$

where T_{max} and T_{min} are the maximal and minimal temperature measured of all T_i, respectively.

The voltage output U_{b_x} of an individual bit bit_x is calculated out of the output voltage

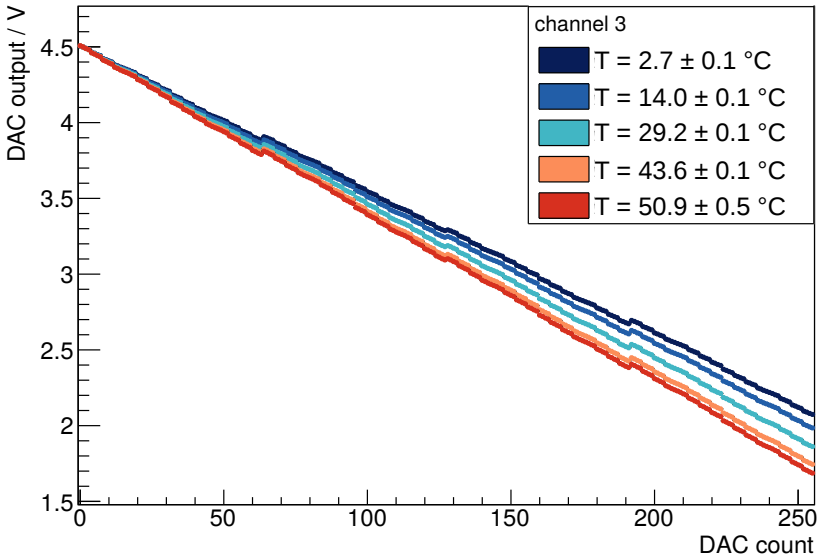

Figure 5.3: Temperature effect on the DAC output voltage, here shown for channel 3. The higher the temperature, the steeper the slope of the trace. Already published in [63].

of the DAC. For each bit, $N_{\mathrm{DAC}}/2$ combinations exist where only the off/on status of one specific bit switches but the status of the other bits is constant. The difference in the output voltages ΔU_k corresponding to these DAC counts is calculated and subsequently the mean is taken. This has the same result as adding up all output voltages U_{i} of DAC count i where bit_x is switched off and subtracting this sum of the output voltages where this particular bit is switched on and subsequently dividing the difference by $N_{\mathrm{DAC}}/2$:

$$U_{b_x} = \frac{1}{N_{\mathrm{DAC}}/2} \cdot \sum_{k=1}^{N_{\mathrm{DAC}}/2} \Delta U_k = \frac{1}{N_{\mathrm{DAC}}/2} \cdot \left(\sum_{i=1;\, bit_x=\mathrm{off}}^{N_{\mathrm{DAC}}} U_i - \sum_{i=1;\, bit_x=\mathrm{on}}^{N_{\mathrm{DAC}}} U_i \right) \quad . \tag{5.6}$$

The standard deviation is calculated with the equation for independent and identical distributed variables:

$$\sigma_{U_{b_x}} = \sqrt{\frac{1}{N_{\mathrm{DAC}}/2} \sum_{i}^{N_{\mathrm{DAC}}/2} (\Delta U_k - U_{b_x})^2} \quad . \tag{5.7}$$

Subsequently, the uncertainty on the mean is calculated and taken as error on the voltage value of the bit.

In fig. 5.4 the temperature dependence of the voltage value of an example bit is shown for five different channels. Numerical results and χ^2/ndf are listed in appendix 2. Generally, the χ^2/ndf confirm that the fits describe the dependence well. The voltage values for the bits and temperature slopes are similar for external and internal reference source, see appendix 1 and 5.2

As already seen in fig. 5.1, the values of the bits vary from channel to channel, corresponding to the vertical shift. But the slope of the voltage over temperature is nearly equal for all five channels. Thus, the weighted average and the standard deviation of

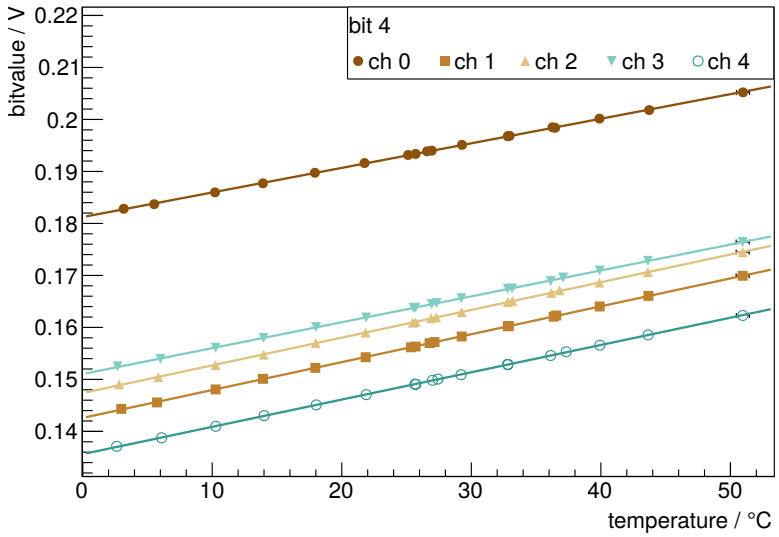

Figure 5.4: Temperature dependence of the voltage value of bit 4 of the first 5 channels for the external reference source. Internal and external reference source show the same characteristics, see table 5.2.

the slope are calculated for each bit and taken for all channels, including the 27 remaining ones which have not been measured. Since the equations are needed for different analyses, these are given in general terms. The weighted average is calculated with

$$A = E(X) = \sum_i^N \frac{X_i}{\sigma_{X_i}^2} \Bigg/ \sum_i^N \frac{1}{\sigma_{X_i}^2} \tag{5.8}$$

and the standard deviation with

$$\sigma_A = \sqrt{E(X^2) - E(X)^2} = \sqrt{\sum_i^N \frac{X_i^2}{\sigma_{X_i}^2} \Bigg/ \sum_i^N \frac{1}{\sigma_{X_i}^2} - \left(\sum_i^N \frac{X_i}{\sigma_{X_i}^2} \Bigg/ \sum_i^N \frac{1}{\sigma_{X_i}^2} \right)^2} \tag{5.9}$$

where N is the number of measurements, X is the measured quantity to be averaged, σ_X its uncertainty and E(X) or E(X^2) is the expected value of X or X^2, respectively. Here, the X_i are the individual slope values, σ_{X_i} the corresponding uncertainties resulting from the fit with ROOT [64] and $N = 5$ is the amount of evaluated channels. The determined values for the slope of each bit are listed in table 5.2. These are implemented into the operation programme of the Aachen Muon Detector. Still, one measurement at one temperature for each of the remaining channels is required to get a start value for each bit.

A hint to the transferability of the results to other boards is given by the study of a second EASIROC evaluation board which shows similar results which match within the 2σ region, see table 5.2. Hence, for future characterisations, it is possible to reduce the amount of measurements and check the compliance before taking a whole set of data.

Next, the dependence of each channel's maximal output voltage on temperature is evaluated. To use more than one data point per channel (where all bits are switched off), the maximum is calculated using the voltage at every DAC step y. For this, the DAC voltage output U_y at each step and the voltage values of the bits U_{b_i} which are

	board 36 [10^{-4} V/°C]		board 35 [10^{-4} V/°C]	
Bit	internal	external	internal	external
0	0.32 ± 0.06	0.32 ± 0.06	0.35 ± 0.04	0.32 ± 0.02
1	0.67 ± 0.03	0.65 ± 0.02	0.61 ± 0.04	0.62 ± 0.03
2	1.34 ± 0.05	1.30 ± 0.04	1.24 ± 0.03	1.27 ± 0.08
3	2.66 ± 0.07	2.56 ± 0.05	2.54 ± 0.04	2.61 ± 0.09
4	5.3 ± 0.3	5.2 ± 0.2	5.2 ± 0.1	5.3 ± 0.1
5	10.6 ± 0.2	10.2 ± 0.2	10.2 ± 0.2	10.5 ± 0.2
6	21.1 ± 0.4	20.6 ± 0.3	20.1 ± 0.3	21.0 ± 0.5
7	41.8 ± 0.7	40.4 ± 0.4	39.8 ± 0.6	41.4 ± 0.7

Table 5.2: Voltage over temperature slope for all bits, averaged over the first 5 channels. Board 36 (used for further analysis and data taking) and board 35 are evaluated. The fit results for the individual channels of board 36 are listed in appendix 2

switched on are summed up

$$U_y^{\max} = U_y + \sum_{i=1;\, bit_i=\text{on}}^{bits} U_{b_i} \quad . \tag{5.10}$$

Since switching on bits reduces the DACs' output voltage, eq. 5.10 is the reverse process to calculate back from the DAC output to its maximum. The uncertainty $\sigma_{U_y^{\max}}$ is calculated with error propagation out of the uncertainty on the single bits $\sigma_{U_{b_x}}$, the uncertainty on the DAC voltage output $\sigma_{U_{\text{DAC}}} = 0.0002\,\text{V}$ and the accuracy of the FLUKE multimeter $\sigma_{U_{\text{FLUKE}}} = 0.0004\,\text{V}$. The uncertainty on the maximal output $\sigma_{U_{\text{DAC}}}$ is determined as variance of ten voltage measurements with all bits switched off. Out of all 256 $U_y^{\max}$ values, the weighted average and the standard deviation are calculated with eq. 5.8 and 5.9 respectively, where $X_i = U_y^{\max}$ and $\sigma_{X_i} = \sigma_{U_y^{\max}}$.

The maximal output depends on the chosen reference source. While the internal source allows for fine tuning control of up to approximately 2.5 V, the external source reaches up to 4.5 V. Values close to these limits are expected for the maximal output delivered by the DAC. The results are shown in fig. 5.5 for the internal and external reference source.

ch	**external source**			**internal source**		
	voltage slope [10^{-5} V/°C]	σ [10^{-5} V/°C]	χ^2 / ndf	voltage slope [10^{-5} V/°C]	σ [10^{-5} V/°C]	χ^2 / ndf
0	1.5	0.9	1.56	-27.7	0.4	1.75
1	6.6	0.8	1.19	-18.7	0.4	1.05
2	1.9	0.9	0.73	-23.6	0.4	0.43
3	5.3	0.9	0.78	-19.5	0.4	0.59
4	5.7	0.9	0.79	-18.9	0.3	0.76

Table 5.3: Temperature dependence of the maximal output voltage for external and internal reference source for the first 5 channels.

For both reference sources the maximal output voltage depends on the channel. Thus, each channel has to be calibrated for a correct bias voltage correction. In case of the

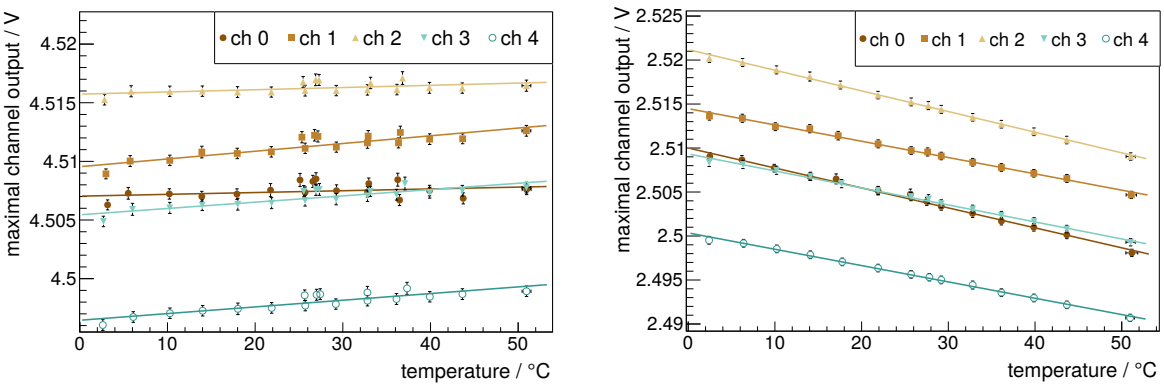

(a) External reference source.

(b) Internal reference source.

Figure 5.5: Temperature dependence of the maximal output value of the DAC for the first 5 channels. While the external reference source shows variations for all channels but with negligible dependences, the internal reference source causes a more distinct dependence. For higher temperatures, the maximal value decreases. The fluctuations in the slope are small enough to take the average and transfer it to all channels.

external reference source, the maximal output voltage shows only a small temperature dependence, see table 5.3. The slope varies from channel to channel. For the further operation of the Aachen Muon Detector, this variation of $(4 \pm 2) \cdot 10^{-5}\,\mathrm{V/°C}$ (mean and standard deviation) is small enough to be neglected and to avoid time-consuming calibration measurements. Instead, one measurement at room temperature can be taken to get the maximal output. However, the internal reference source shows a clearer temperature dependence of the maximal output voltage, see table 5.3. The voltage slopes of the example channels only vary on a small scale compared to the necessary accuracy for operating SiPMs. As a consequence, the result is averaged and transferred to the remaining 27 channels which have not been characterised in detail. Specifically, this means a correction factor of $-(22 \pm 4) \cdot 10^{-5}\,\mathrm{V/°C}$ is applied in the later operation of the AMD. Hence, only calibration measurements at one temperature are necessary for the internal source, too.

Summarising, one calibration measurement of the DACs of all channels is necessary since the bit values differ. But for temperature variation effects, the evaluation of a single channel is sufficient. Here, the bitvalue's slope of voltage change over temperature can be transferred from one channel to the other ones. This applies both for internal and external reference source. In case of the maximal output of the DAC, internal and external sources cause different dependencies. While for the external source no correction on temperature effects are needed, the internal source requires a correction factor. This can also be transferred from one channel to the remaining ones. Still, the maximal output differs for each channel and thus has to be calibrated.

The voltage output of the DAC which is supplied to the SiPMs for bias voltage fine tuning can thus be calculated with

$$U_{\mathrm{DAC}}[ch] = U_{\mathrm{max}}[ch] + s_{U_{\mathrm{max}}}[ch] \cdot (T - T_a) + \sum_{i=1;\, bit_i=\mathrm{on}}^{N_{\mathrm{bits}}} \left(U_{b_i}[ch] + s_{U_{b_i}}[ch] \cdot (T - T_b) \right) \tag{5.11}$$

where ch is the number of the channel for which the output is calculated, $U_{\max}$ is the maximal output of the DAC when all bits are switched of, $s_{U_{\max}}$ is the slope of the temperature dependent maximal output, U_{b_i} is the voltage value of bit i, $s_{U_{b_i}}$ is the slope of the temperature dependent bit's voltage value and $N_{\text{bits}} = 8$ is the number of bits. T_a and T_b are the temperatures at which the reference value of the maximal output and the bits is measured, respectively. See appendix 1 for all values.

Measurements with a second evaluation board give a hint that these results apply for other chips, too. This includes the correction factors. Thus, the amount of calibration measurements can be reduced drastically.

5.2.2 Noise Quantification and Threshold Constraints

During the operation of the Aachen Muon Detector, the knowledge of the background or dark count rate is essential. When studying extensive air showers, the background rate is subtracted from the results to isolate the signal. Since noise effects can occur in distinct severity for the different signal lines (channels), the channel uniformity is tested. The background rate varies with temperature and is hence determined in a wide temperature range. The overall aim is to set a threshold on the signal pulses which is equally high in p.e. for all channels and adjusts with temperature. As the EASIROC provides multiple internal amplification factors, their effects on the dark count rate scan are studied.

Measurement Setup

The measurement of the dark count rates is performed with the same setup as used in the prospective operation. This guarantees that all noise sources are included in the background rate. A schematics of the setup is shown in fig. 5.6. One SiPM carrier board is packed in a lightproof box and only the coaxial cables lead out. These connect the SiPMs to the first eight channels of the evaluation board. The SiPM carrier board and the evaluation board are situated inside the COOLI to allow temperature variations. A PC is connected to the USB plug of the EASIROC test board for controlling the data acquisition and the readout process. The SiPMs and the test board are powered by the power supply unit (PSU) which in turn is connected to a 24 V power source. A multimeter measures the PSU output voltage supplied to the SiPMs.

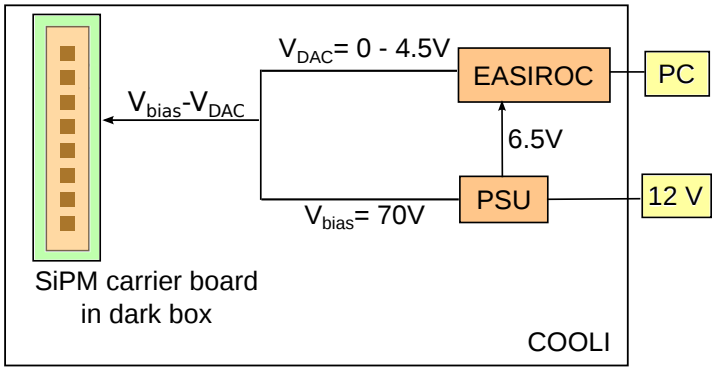

Figure 5.6: Schematics of the test setup for background rate measurements. Power supply unit (PSU), SiPM carrier board and EASIROC evaluation board are placed inside the cooling chamber COOLI to enable measurements at different temperatures.

Before starting a measurement, the SiPMs and the evaluation board have to be connected to the power supply. Here, the order of switching on the devices is crucial to avoid damage. The evaluation board is supplied with power first. Then, all 8-bit DACs for the bias voltage regulation are switched on in the slow control. This enables the current flow through the DACs to ground level. Otherwise, a too high voltage on the DACs could destroy parts of the EASIROC since the current would flow uncontrolled through the chip. Afterwards, the SiPMs are supplied with power. When turning on the power supply, the voltage increase should not exceed a few volts per second as this can also cause a too high given voltage at the 8-bit DAC input. The applied voltage is set to approximately 70 V. Here, the exact value depends on the temperature range expected for the measurements and thus the necessary range for the bias voltage fine tuning. As the 8-bit DAC covers only a limited range, the applied voltage is adjusted before measurements to fit this range.

Measurement Procedure

The EASIROC allows the setting of a discriminator threshold with a 10-bit DAC (c.f. chapter 3.4.2). By increasing the threshold, only higher signal pulses cause a positive discriminator output. This can be used to reduce the noise level significantly since these events usually have small pulses. But it also reduces the signal by cutting off events with low pulse heights. Hence, a trade-off between noise reduction and signal loss has to be found. For this purpose, the background rate is measured at each threshold value of the 10-bit DAC.

When the measurement programme is started, the multimeter reads out the voltage given by the PSU at the SiPMs. Then, the temperature sensors on the SiPM carrier board and on top of the EASIROC are read out. Out of all these values, the operation voltage of each SiPM is determined: The manufacturer gives a specific recommended operation voltage for each SiPM. With the stated values by Hamamatsu and the temperature correction for the SiPMs (c.f. chapter 5.1), the corrected bias voltage is determined. Subsequently, the difference of the given voltage by the PSU and the optimal bias voltage is calculated. This required voltage adjustment for an optimal operation is done with the 8-bit DACs. The DAC count which corresponds to this voltage difference is calculated by the measurement programme running on the PC, taking into account the temperature dependence of the DACs (c.f. chapter 5.2.1).

The 8-bit DAC counts and the 10-bit DAC threshold count are written into the slow control. After this new configuration is committed, a short waiting period is essential to allow the changed values to stabilise, in this case the threshold and the supplied voltage. The input signal from the SiPMs are processed over the fast shaper chain and compared to the threshold value with the discriminator. Continuously, its status is available for all channels individually on the T0 to T31 outputs on the evaluation board. Every 10 ns, the FPGA checks for all 32 channels if the discriminator was on (signal above threshold) within the last 10 ns. Each time the discriminator switches from off to on, a counter for this channel is incremented by one. A further counter which is common for all 32 channels is incremented by one every 10 ns to control the predefined measuring time t_{measure}. After $t_{\mathrm{measure}}/10\,\mathrm{ns}$ counts, all 32 counters are read out and copied into a memory of the FPGA. All counters are reset and the measurement is rerun for a given number of times N_{run}. Periodic read out of both temperature sensors and the voltage output of the PSU and subsequent adaption of the fine tuning voltage by adjusting

the 8-bit DAC values guarantees that the SiPM characteristics are stable. The data transfer from FPGA to PC of the measured event counts is done via USB.

Measurements were taken for 8 channels, at various internal gains of the EASIROC (see chapter 3.4.2) and for different temperatures.

Analysis of Data

With known measuring time t_{measure} and event numbers N_{events}, the event rate for each threshold value and each channel is calculated with

$$R = \frac{\sum_{i}^{N_{\text{run}}} N_{\text{events},i}}{t_{\text{measure}} \cdot N_{\text{run}}} \quad . \tag{5.12}$$

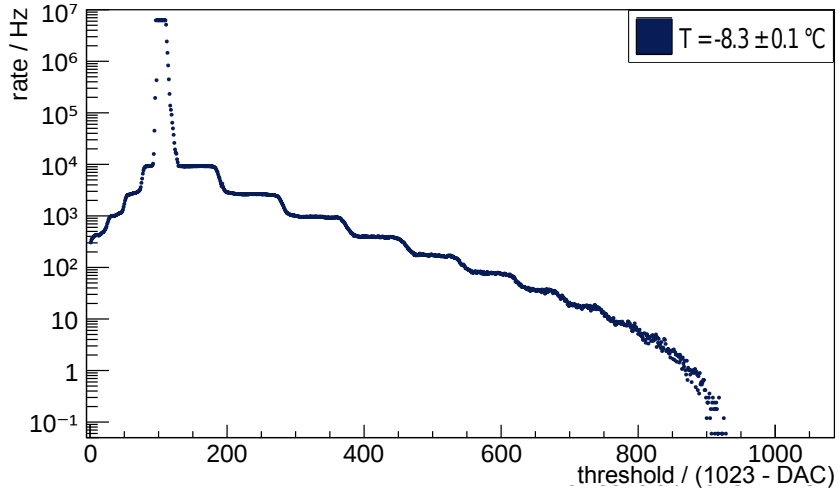

Figure 5.7: Dark count rate scan for channel 3 at (-8.3 ± 0.1)°C. The step-like structure is caused by the nearly discrete pulse characteristics of SiPMs. Each step corresponds to a photo equivalent. Around the baseline of the pulses at around (1023-DAC)=120, the fluctuating traces cause high rates, see fig. 5.8. For the high end of the threshold values, saturation effects occur.

The result for a dark count rate scan is shown in fig. 5.7. From left to right, the set threshold value increases. This is equivalent to a decreasing 10-bit DAC count, down from 1023 to 0. The DAC scale was inverted to make the graphs more intuitive so that the necessary pulse height to pass the discriminator increases from left to right. First, the rate rises stepwise. This can be understood with help of fig. 5.8. For low threshold values, the discriminator triggers on the undershooting bit of the pulse. Threshold values further off from the baseline of the pulse traces result in less entries as only high pulses lead to high overshoots. Close to the zero level of the traces, the discriminator picks up events of the fluctuating trace itself. Thus, the event rate increases drastically, here seen at around (1023-DAC)=120. For threshold values higher than the zero level of the traces, the positive parts of the pulses are compared to the threshold. Steps in the dark noise rate scan occur due to the nearly discrete nature of SiPM pulses. When comparing the step-like structure to the charge integral of an SiPM (see fig. 3.10 in chapter 3.3), the steep bit of a step is equivalent to a peak of the charge integral

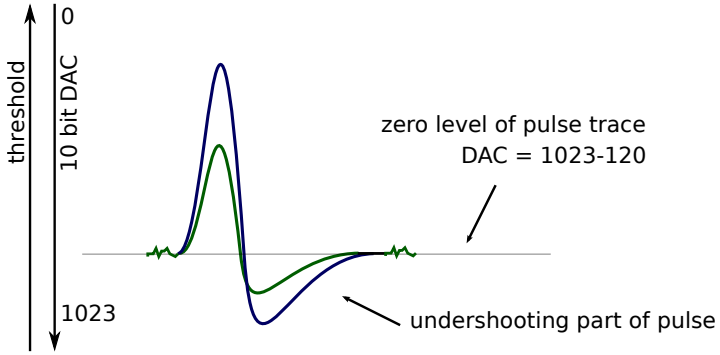

Figure 5.8: Schematics of the working principle of the threshold. High DAC counts correspond to an output of low voltage values. With rising threshold, first the fluctuating zero level line of the pulse traces is passed and then the positive parts of the pulses compared to the threshold by the discriminator.

spectrum. The peak width corresponds roughly to the width of the steep bit of the step. Thus, the steps can be attributed to photo equivalents (p.e.) (see chapter 3.4.2).

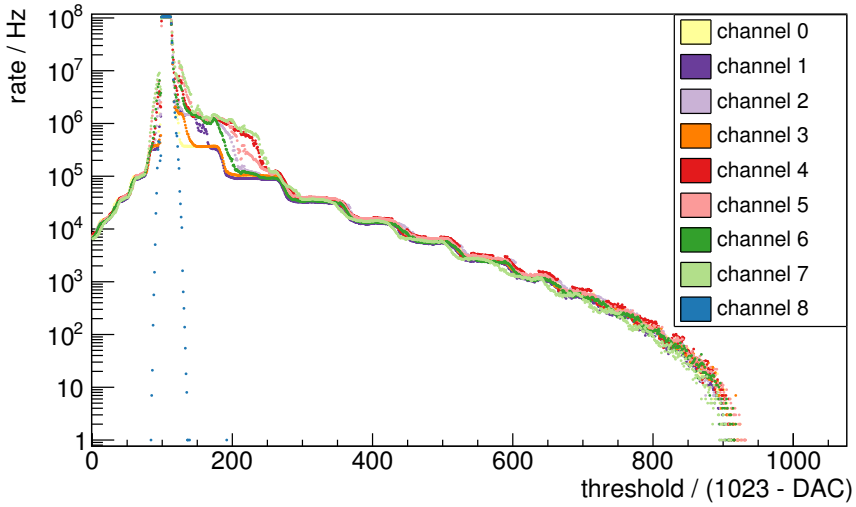

Figure 5.9: Background rate scan for the first nine channels at (10.0 ± 0.5)°C and internal gain control value 1. Electronic noise effects occur for DAC counts between (1023-DAC)=340 and 120. High rates occur at around (1023-DAC)=120 for thresholds close to the zero level of the traces. This is demonstrated by channel 8 to which no SiPM is connected.

Before discussing the results for different channels, amplification factors and temperatures, an occurring feature is elucidated. For all measurements, electronic noise effects from the EASIROC board arise (see fig. 5.9) for low discriminator thresholds in the DAC count range (1023-DAC)≈120 - 340. This is equivalent to the low p.e.-range. Their severity varies with the above mentioned parameters, see fig. 5.9 as an example for different channels. High temperatures generally show more severe noise effects. Tests have been performed to identify the source of the noise. These include shifting the SiPMs by one read out channel. The noise is not affected and has the same shape as before for each channel. Thus, the SiPMs can be excluded as source. Additionally, a

second EASIROC evaluation board was taken to check whether the effects are board specific. But again the same effects occur and the same channels are affected. Also the 10-bit DAC for threshold setting can be excluded as origin since output measurements prove its linearity and no unexpected behaviour occurs. Measurements by other groups confirm the 10-bit DAC stability [65]. Finally, the USB communication between PC and the USB communication chip on the EASIROC board was turned off during the measurements and only switched on shortly for data readout. This reduces the noise significantly to a very low level. For rate scans like the determination of the dark count rate, the method is applicable, but for the final operation of the AMD a constant USB communication will be necessary. As so far no other possibilities were found to reduce the noise, only measurements with thresholds above (1023-DAC)≈340 will give exploitable results.

During the data taking process of the subsequently shown results, the USB communication was switched off.

Channel Uniformity

A measurement of the first 8 channels at gain control value = 1 (high amplification, c.f. chapter 3.4.2) and $T = (10.0 \pm 0.5)°C$ was already shown in fig. 5.9 (results without USB communication only differ in a smoother step-like behaviour for low p.e. pulses). While the dark count rate is constant for all channels to a high degree, the positions of the p.e. steps vary slightly. Since their position is crucial for the analysis of SiPM pulse heights, the effects on channel uniformity have to be characterised within each analysis. For the calculation of the pulse height in p.e., the p.e. step positions have to be determined in terms of DAC counts. For operating the Aachen Muon Detector, the DAC count is calculated for the desired threshold in p.e.. If no threshold value can be set which corresponds to the same p.e. step for all channels, the channel uniformity is not given and they have to be analysed individually. Alternatively, the gain of the SiPM of the channels can be adapted such that the traces show steps at equal positions. This in turn is accompanied with an analysis when a readjustment is necessary.

To determine the conversion equation from p.e. to DAC count, a numerical derivation of the dark count spectrum is applied. Subsequently, Gauss functions are fitted onto the peaks and thus their positions are determined. The uncertainties of the Gaussian fits reflect the accuracy of finding the peak, but not the DAC range of pulses of equal p.e. steps. Thus, the uncertainty of the fit underestimates the uncertainty. In fig. 5.9, the DAC range of each p.e. step corresponds to the steep parts between the plateaus of the scan. Therefore, the uncertainties are read off manually. The half of the width between the points where the spectrum steepens and flattens is taken as uncertainty. Analytic results for the determination of the position $P(pe, T)$ of a fixed p.e. step pe at temperature T out of the determined values are given together with the analysis of the temperature dependence see eq.5.14 and table 5.4.

Internal Gain Effects

The internal amplification of the EASIROC allows for the amplification of pulses before further processing of the signal. Measurement conditions, especially the expected pulse heights, define which amplification factor is needed. The amplification factor is controlled by a gain control of 4 bits. For low control values, high amplifications of the

signal are obtained and vice versa. When high pulses are expected, a small amplification factor is required (i.e. a high gain control value) to allow for a large dynamical range for the slow shaper and ADC measurements and to avoid saturation effects. Additionally, when expecting large pulses higher thresholds can be set for noise suppression. In contrast, for low rate measurements, such as the dark noise scan, a high amplification factor enables a data analysis of higher precision. For the Aachen Muon Detector, simulations and first test measurements have to clarify the expected height of typical signal pulses from air shower muons. Then, they have to be compared to the covered range of the different amplification measurements and the optimum has to be chosen. Since for this comparison the range of the DAC for all internal gains has to be known, all are measured for the first eight channels. The evaluation of various gain control values is shown in fig. 5.10 exemplarily at approximately (9.1 ± 0.1)°C for channel 0. Rate scans with high amplification factors show saturation effects for high thresholds.

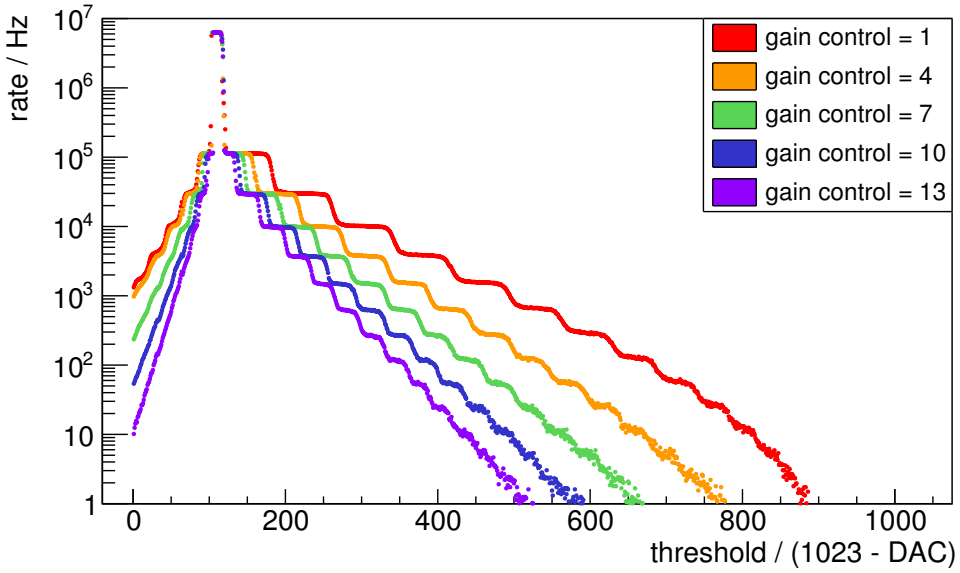

Figure 5.10: Background rate scan for different gain control values at approximately (9.1 ± 0.1)°C and for channel 0. The gain control value is low for a high amplification of the signal and vice versa.

The further measurements and analyses are limited to the gain control value of 8. Still, some example plots are given for a gain control of 1 as this was measured for a few control temperatures to exclude a completely different behaviour. This is mainly due to practical reasons as each measurement takes approximately 8 hours. The gain control value was chosen due to medium amplification factors covering a wide range of applications. Furthermore, the dark noise rate can be quantified with any amplification factor. Additionally, the basic behaviour under temperature variations is expected to be comparable for all gains.

Temperature Effects

The dark noise rates of SiPMs are temperature dependent. Hence, the rate scans have to be performed at different temperatures to quantify the effect. Additionally, this tests

whether all temperature dependencies (SiPMs, 8-bit DAC) are implemented yet or if further corrections are needed.

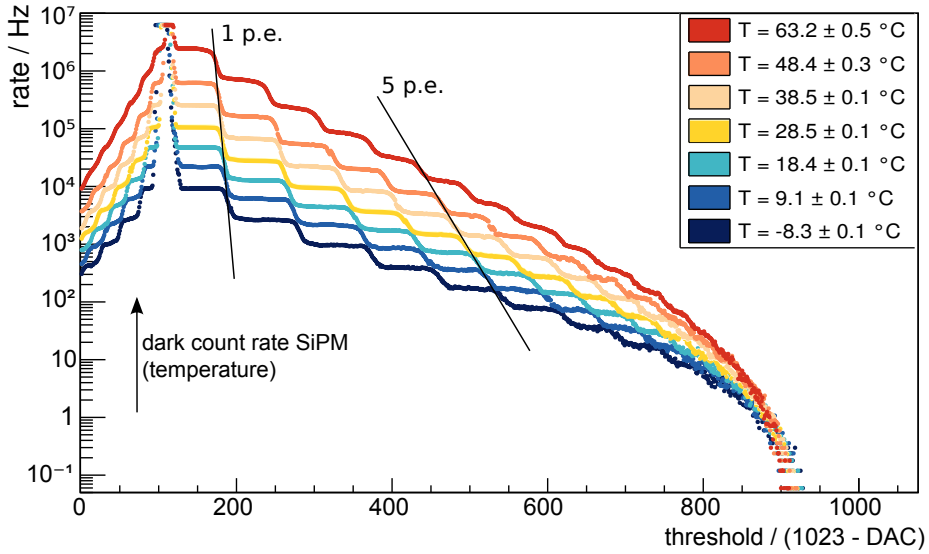

Figure 5.11: Background rate scan for different temperatures for channel 0 and an internal gain control of 1. Both SiPMs and EASIROC are at the same temperature. A vertical and horizontal shift of the traces is observed. The horizontal effect indicates an additional temperature effect of the EASIROC. The vertical shift is due to a changing dark count rate of the SiPMs with temperature variations.

In fig. 5.11 a selection of measurements in a temperature range of -10°C to 65°C is plotted. A vertical and a horizontal shift exist. The vertical shift is the change in the dark count rate of the SiPMs. The horizontal shift is due to another temperature dependence of the EASIROC. To prove this, a second COOLI is used in the setup and a single SiPM is placed inside and connected to a channel of the evaluation board which is placed in the first COOLI. The SiPM carrier board is taken out of the setup. In this configuration, the temperature for SiPM and EASIROC can be regulated separately.

Measurements were taken for constant SiPM temperature and variable EASIROC temperature and vice versa. The results for constant EASIROC temperature mainly show a vertical shift, see fig. 5.12. The step-like rates are still shifted very little to higher pulses for colder temperatures. But in contrast to the previous setup, this shift is nearly constant for all p.e. values and smaller than one p.e. step. Thus, no misinterpretation of pulse heights can occur and the effect is negligible. At stable SiPM temperature, the horizontal shift can be identified, see fig. 5.13. Small vertical variations can result from an unstable bias voltage. This can either result from a varying voltage output of the power supply unit or from fluctuations due to the steps in the output of the 8-bit DACs, see fig. 5.1.

To guarantee a threshold setting at the correct p.e. height, the step-structure of the photo equivalents has to be determined under consideration of temperature variation effects. As before, the p.e. positions are determined for each temperature. In total, the positions are determined for the first four channels for six temperature measurements in a range between approximately -6°C and 63°C. For each measurement, the 0 to 11 p.e. steps are identified. The DAC values of each p.e. for different temperatures are plotted into a graph as a function of temperature, see fig. 5.14 for an example. The

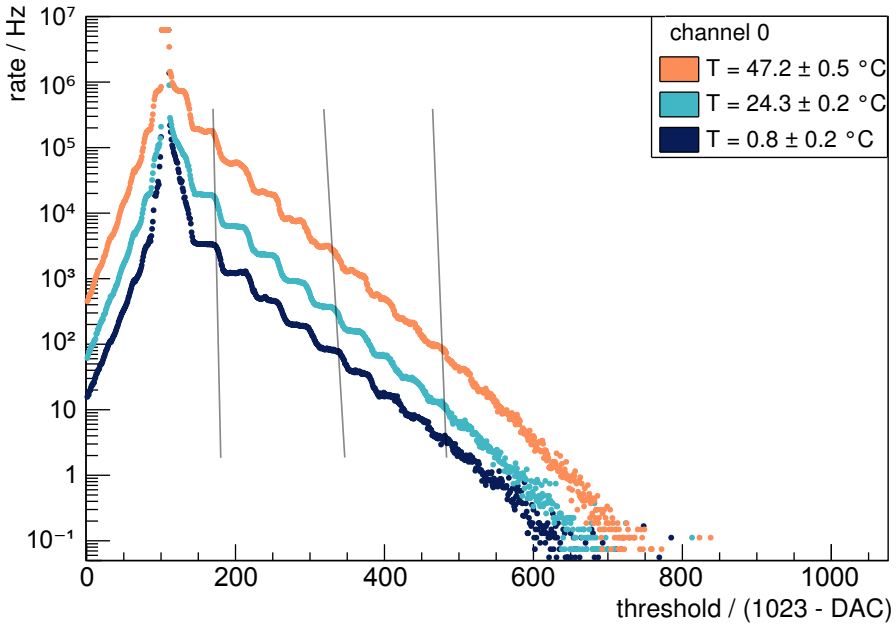

Figure 5.12: Background rate scan for different SiPM temperatures and constant EASIROC temperature of (51.0 ± 0.2)°C at a gain control value of 8. The vertical shift is due to the changing dark noise of SiPMs with temperature differences (the grey lines serve as help for orientation). The horizontal shift is negligible.

uncertainty on the DAC value is the accuracy with which the position of the step is determined. Temperature readout occurs for each DAC value. The mean is taken and as uncertainty the spread of all values. A linear function is fitted onto the data of each p.e.:

$$P[p.e.](T) = p_1[p.e.] \cdot T + p_0[p.e.] \tag{5.13}$$

where $P[p.e.](T)$ is the position of a fixed photo equivalent step $p.e.$ at temperature T in °C in DAC counts. The χ^2/ndf values reveal that the implemented uncertainties are a little too large but for the determination of the temperature dependence this is not problematic. For the other fits, the values are similar. $p_0[p.e.]$ and $p_1[p.e.]$ are the two free parameters of the fit and can be read off from fig. 5.15 for channel 0. To generalise the calculation of the step position for all p.e. values, $p_1[p.e.]$ and $p_0[p.e.]$ are plotted as a function of $p.e.$, see fig. 5.15. Since the dark count traces show saturation effects in the high p.e. range, no linear dependency but one of higher order is expected. A polynomial of second order is fitted to the data points of both graphs and fits nicely, see fig. 5.15. Thus, eq. 5.13 is generalised to

$$P(p.e., T) = (a + b \cdot p.e. + c \cdot p.e.^2) \cdot T + (d + e \cdot p.e. + f \cdot p.e.^2) \tag{5.14}$$

where a, b and c are the free parameters of the polynomial fitted onto the p_1 data points and d, e and f are the free parameters of the polynomial fitted onto the p_0 data points. The χ^2/ndf values confirm that a polynomial of second order fits the data well, see table 5.4. The results for the first four channels are summarised in table 5.4. Within the uncertainties, the values for the four different channels match within approximately two standard deviations.

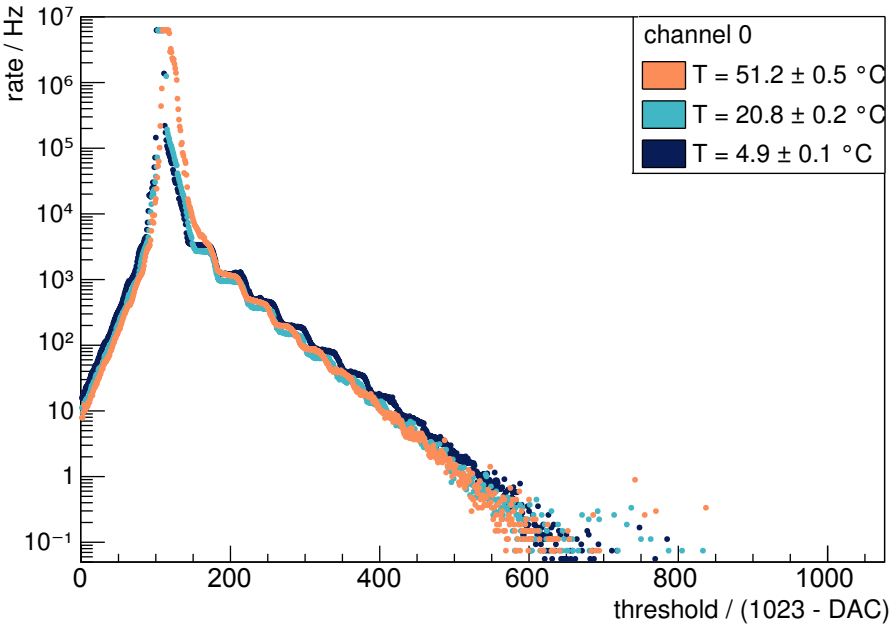

Figure 5.13: Background rate scan for different EASIROC temperatures and constant SiPM temperature of (0.56 ± 0.3)°C at a gain control value of 8. The horizontal shift indicates an additional temperature dependence of the EASIROC. Only small vertical fluctuations between the traces occur, meaning that the shift in fig. 5.11 originates from the SiPM dark noise.

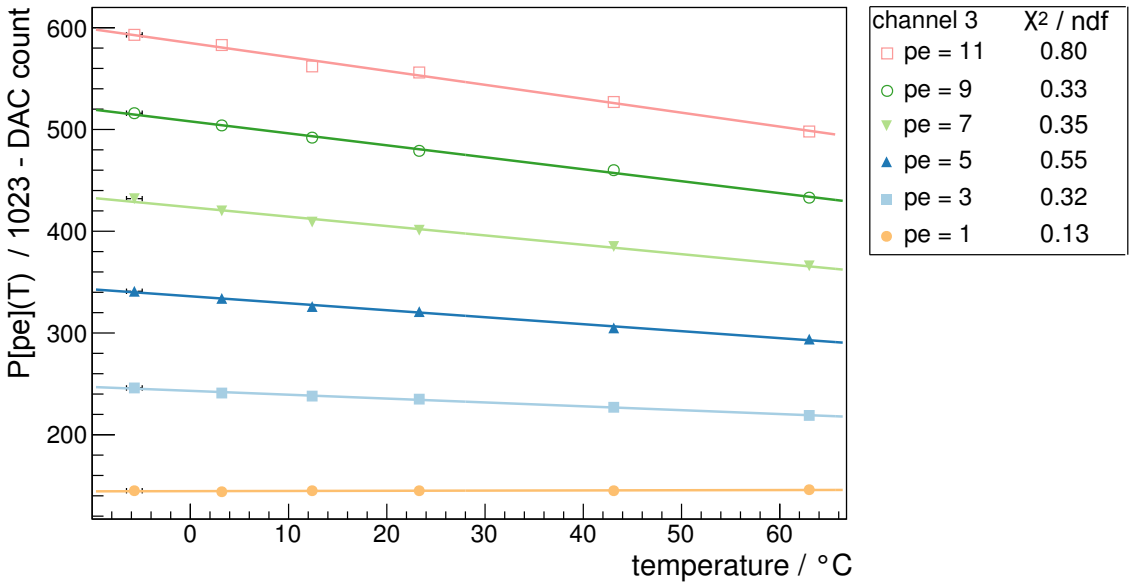

Figure 5.14: DAC values as a function of temperature for some p.e. values for channel 3 and a gain control value of 8. A linear function was fitted to the data points. χ^2/ndf values are given. The slopes of the different p.e. vary.

The temperature dependence of the EASIROC and thus the p.e. step position is considered for the threshold setting. Since only one threshold value can be set with the 10-bit DAC for all channels, a good compliance of the studied channels is advantageous. Otherwise, the set threshold is at different p.e. steps for the individual channels and this has to be taken into account in the analysis. Here, the accordance is given for

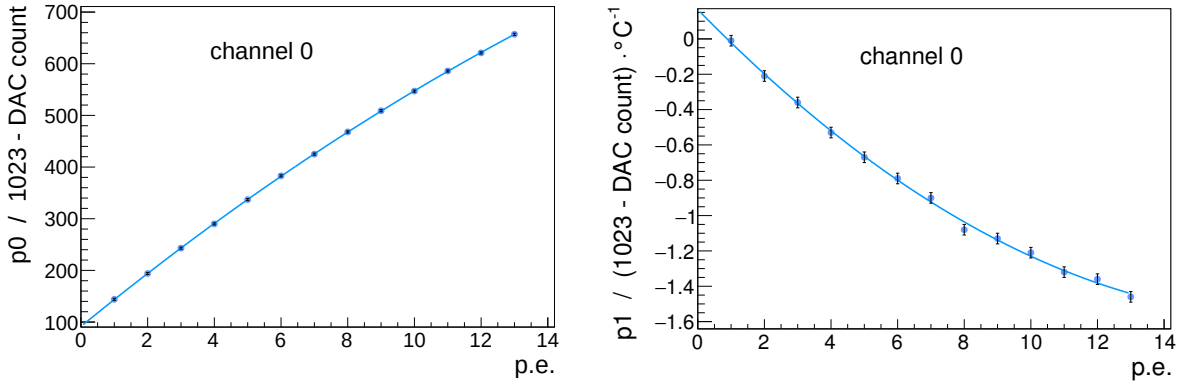

(a) Y-axis intercept p_0 over p.e..

(b) Slope p_1 over p.e..

Figure 5.15: Y-axis intercept p_0 and slope p_1 of fig. 5.14 over p.e. for channel 0. Onto both series of data, a polynomial of second order is fitted to describe the dependence.

Channel	0	1	2	3
a	0.17 ± 0.03	0.15 ± 0.03	0.20 ± 0.03	0.20 ± 0.03
b	-0.19 ± 0.01	-0.18 ± 0.01	-0.21 ± 0.02	-0.20 ± 0.01
c	0.0053 ± 0.0007	0.0042 ± 0.0008	0.0058 ± 0.0008	0.0057 ± 0.0008
χ^2/ndf	0.48	1.10	0.91	0.72
d	91.6 ± 2.0	91.6 ± 2.1	91.5 ± 1.9	93.0 ± 2.0
e	52.7 ± 0.6	52.4 ± 0.7	54.4 ± 1.4	51.9 ± 0.7
f	-0.71 ± 0.04	-0.67 ± 0.05	-0.73 ± 0.05	-0.66 ± 0.05
χ^2/ndf	0.21	0.27	0.31	0.29

Table 5.4: Parameters for the determination of the p.e. position with eq. 5.14 for the first 4 channels and according χ^2/ndf. a, b and c in units of $°C^{-1}$ and d, e, and f are without unit.

the studied channels. In case of strong deviations in the output for different channels during further tests of the AMD, the relevant channel's temperature dependence may be differing from this analysis. Then, the channel has to be characterised and the p.e. positions corrected by the determined differences. Alternatively, the gain of the SiPM can be adjusted by the bias voltage which implicates slight changes in the SiPM properties.

temperature / °C	-10	10	20	30	40	50	60
rate / kHz	10	30	50	100	300	600	$3{\cdot}10^3$

Table 5.5: Dark count rate at 1 p.e. level for several temperatures. The accuracy of the temperature values is about 1°C and the rate values is about 10%. All values are approximate. Hamamatsu states a dark count rate of approximately 100 kHz for 25°C for the installed SiPMs of type S12571-050P which complies with the measured values [48].

Summarising, the dark count rate of the setup is determined for different temperatures in a range from -10°C to 65°C. The rate at the 1 p.e. level for several temperatures

is listed in table 5.5. The first four channels were analysed in detail. Their performance matches within the given uncertainties and thus the characteristics are adapted to all channels. In case of deviating results for an individual channel in prospective measurements with the AMD where other sources causing the effect can be excluded, the performance characteristics of the corresponding channel can be analysed to verify whether this adaption causes the effect. Different amplification factors allow for processing differently high hitrates and hence a wide range of applications. For the gain control value of 8, the temperature dependence of the step-like function is determined. The EASIROC shows a temperature dependence which changes the width of the steps. To allow for a precise threshold setting with the 10-bit DAC, a correction equation cancels out this effect. The resulting p.e. step positions for a gain correction value of 8 in a temperature range from -10 to 60°C according to the correction equation can be read off fig. 5.16. If in the final operation of the Aachen Muon Detector another amplification is applied, further calibration measurements have to be taken but the principle of the analysis remains the same.

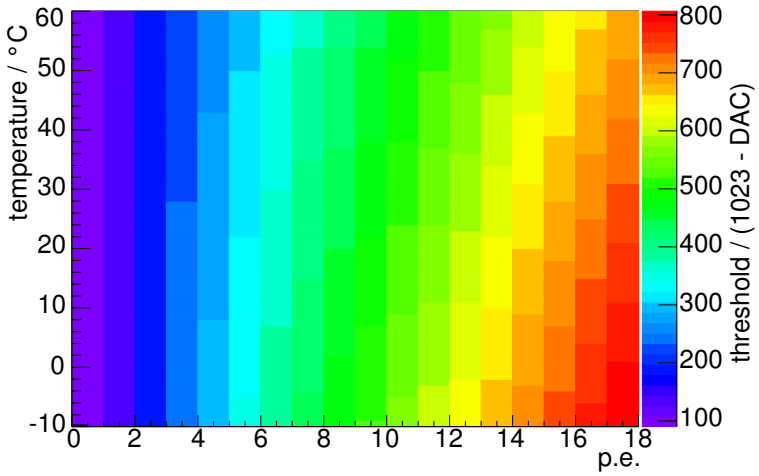

Figure 5.16: Temperature dependent p.e. position for the first 18 p.e. steps for an internal gain control value of 8 as calculated with eq. 5.14. The colours encode the step position in DAC counts.

5.3 Power Supply Stability

The power supply unit (PSU) was developed by the electronics workshop of the III. Phys. Inst. of RWTH Aachen University. The output voltage can be varied in a small range using a potentiometer to manually adapt to the external conditions and thus to the changing SiPM and EASIROC characteristics. For all test measurements, voltages between approximately 68 and 70 V are applied.

As for the SiPMs and the EASIROC test board, the temperature dependence of the PSU has to be quantified. Therefore, a temperature sensor is mounted on top of the operational amplifier which is one of the components of the PSU regulating the output voltage. The PSU is placed inside the COOLI and connected to a multimeter which is read out by a PC. An external power source supplies the PSU with a voltage of about

24 V. The COOLI is set to a temperature of -6°C. The maximal output voltage of the PSU is read out and the temperature stabilisation of the COOLI is turned off. Thus, the temperature inside the COOLI increases slowly. Voltage values are taken every 30 s. Once the COOLI reaches approximately 12°C the temperature is set to 70°C. During the heating up of the interior of the COOLI data is taken constantly. As soon as the temperature reaches 70°C, the COOLI is switched off again to pass through these temperature values again.

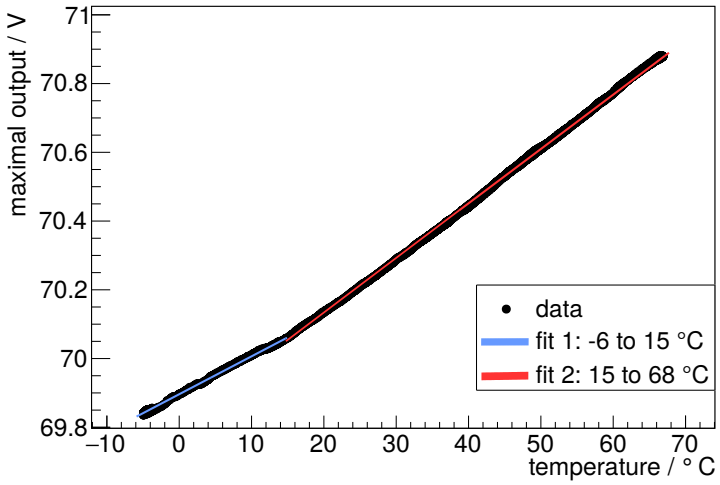

Figure 5.17: The temperature dependence of the power supply unit (PSU) can be described with two linear fits. The break between both lines occurs at approximately 15°C.

The voltage output as a function of temperature is shown in fig. 5.17. The uncertainty on the output is estimated out of the spread of values taken at the same temperature and amounts to about 5 mV. A decrease of the output voltage with decreasing temperature is observed. This dependence is split up in two linear fits. Between approximately -6 to 15°C, the slope is about 11 mV/°C. Between approximately 15 to 70°C, the slope is about 16 mV/°C. The χ^2/ndf are 0.31 and 0.66, respectively which implies that the estimation of uncertainties is a bit too conservative but besides the fitted functions describe the data well. Thus, the output voltage at a certain temperature can be calculated with

$$V_{\mathrm{PSU}}(T) = (69.896 \pm 0.002)\,\mathrm{V} + (11.0 \pm 0.2)\ \mathrm{mV/°C} \cdot T \tag{5.15}$$

for a range between -6 to 15°C and with

$$V_{\mathrm{PSU}}(T) = (69.819 \pm 0.004)\,\mathrm{V} + (15.8 \pm 0.3)\,\mathrm{mV/°C} \cdot T \tag{5.16}$$

for a temperature range from 15 to 70°C where T is the temperature in ∘C. The origin of the break in the output voltage is still not understood [66].

For future versions of the AMD, the electronics workshop develops PSUs which are less influenced by varying temperatures and do not show the break in the output voltage. Until then, the temperature effect is corrected for in the measurement programmes or continuously monitored using an externally read out multimeter.

5.4 Correction Flowcharts

The measurement and characterisation procedures as described in the preceding chapters are time consuming and thus impractical for frequent repetitions of other channels and boards. Thus, results are adapted for other channels and boards as far as possible. The remaining necessary measurements are listed in flowcharts, split into the temperature corrections for SiPMs and PSU of chapters 5.1 and 5.3, see fig. 5.18, the voltage output characterisation of the 8-bit DAC of chapter 5.2.1, see fig. 5.19, and the characterisation of the dark noise spectra and related effects of chapter 5.2.2, see fig. 5.20. A whole characterisation and analysis of a new evaluation board takes approximately a week with the current measurement conditions and applying the method given in the flowcharts. This can still be reduced when e.g. other temperature chambers which adjust to fixed temperatures faster are available. Additionally, in principle it is possible to characterise multiple boards in parallel which will further reduce the required time.

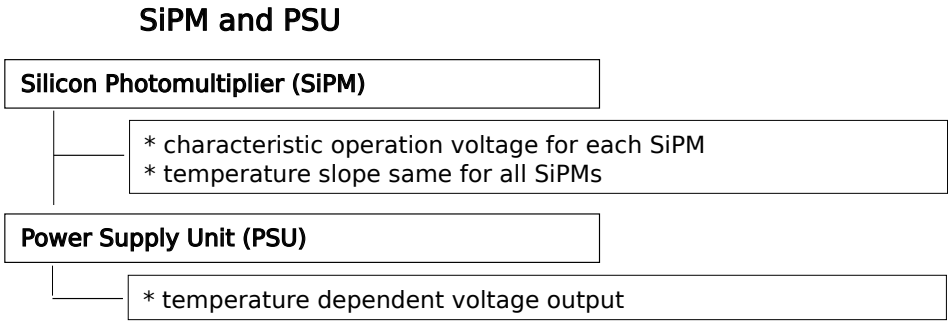

Figure 5.18: Correction on temperature for both SiPMs and PSU is needed, see chapter 5.1 and 5.3.

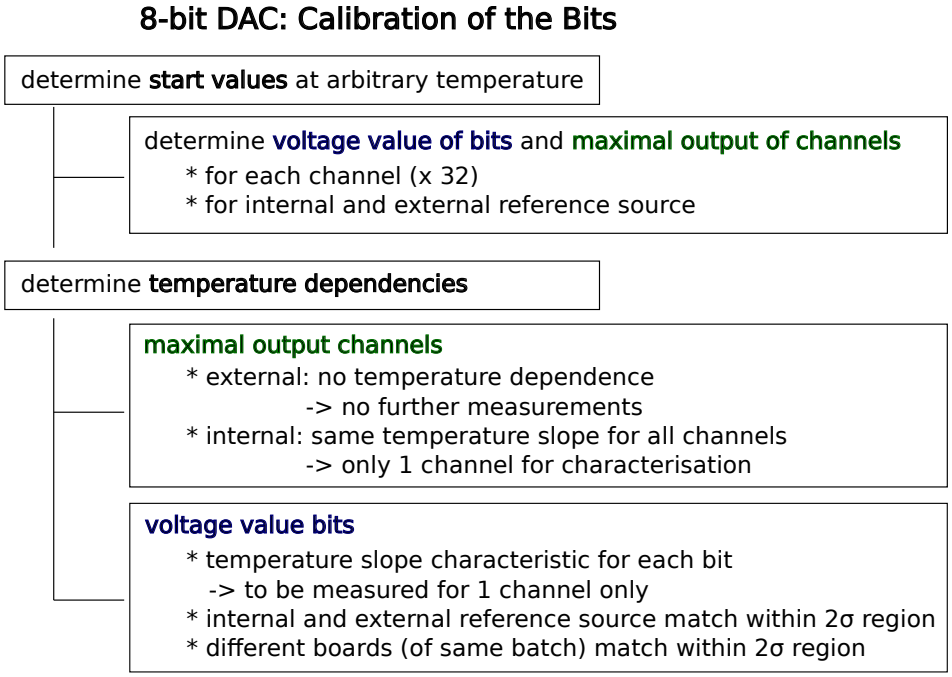

Figure 5.19: Flowchart for the characterisation of the voltage output of the 8-bit DACs for the bias voltage fine tuning of the SiPMs, see chapter 5.2.1.

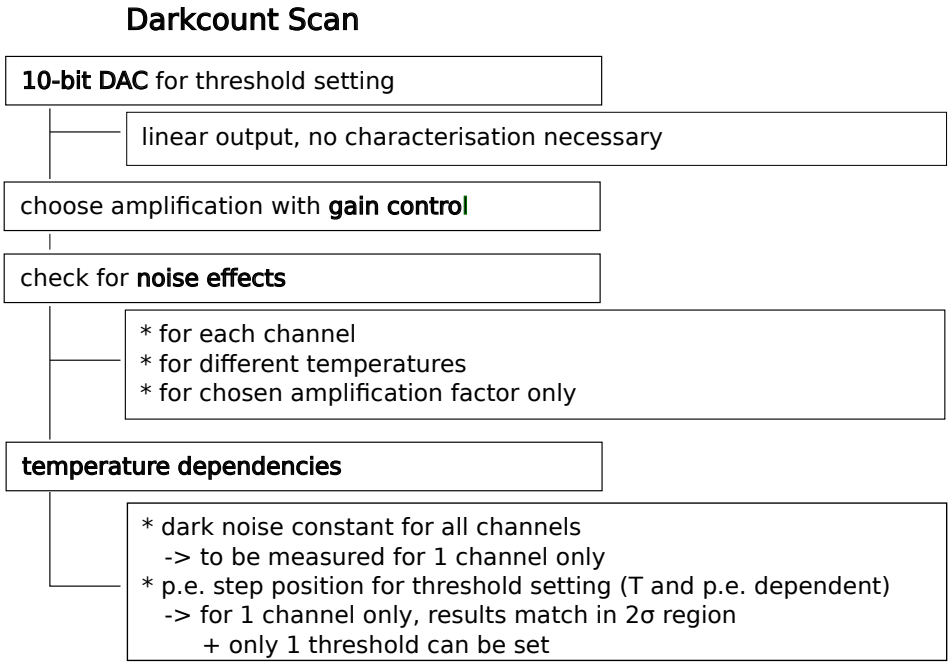

Figure 5.20: Flowchart for the dark count characterisation and determination of temperature, noise and internal gain effects, see chapter 5.2.2

Chapter 6

Test Measurements Towards the Aachen Muon Detector

The mechanics and electronics of the detector have thoroughly been tested as decribed in chapter 4 and 5. Thus, the components can be assembled for test measurements of the complete readout chain and performance tests. Therefore, a new setup for test measurements is developed, called the Aachen Muon Detector shelf. It allows for attaining easy access to all components. Tests include the first application of a complete readout chain, the measurement of the pulse height distribution of the atmospheric muon signal and the study of the output of tiles with different wrappings.

6.1 First Measurements with a Complete Readout Chain

The dark count measurements have quantified the occurring noise effects under various circumstances, see chapter 5.2.2. The next step is to connect a scintillator tile to one of the SiPMs and thus complete the readout chain.

Measurement Setup

The measurement setup of chapter 5.2.2 is complemented with a wrapped scintillator tile and a clear light guide which connects tile and SiPM. Thus, the setup consists of one scintillator tile, a clear fibre, an SiPM carrier board, the EASIROC evaluation board and the power supply unit (PSU). All components are placed inside of one COOLI. The PSU is powered from outside of the COOLI by a voltage supply. Compared to the previous setup, the multimeter is only used for the initial setting of the output voltage of the PSU but not during data taking. All quantified temperature dependences are implemented into the measurement programme running on the PC, including SiPMs, EASIROC and PSU. A schematics of the test setup is shown in fig. 6.1.

To avoid any light pollution caused by the setup itself, all LEDs of the EASIROC test board are either switched off or desoldered. The scintillator wrapping serves as an additional light shield besides being a reflector for light escaping the tile. External penetration of light is excluded as the setup is inside the lightproof COOLI. The outcoming signal can thus only arise from traversing particles or the noise spectrum as measured in chapter 5.2.2.

Measurement Procedure

The measurement procedure is exactly the same as for the measurement of the dark count rate in chapter 5.2.2. Thus, it is dispensed with a detailed description. Briefly

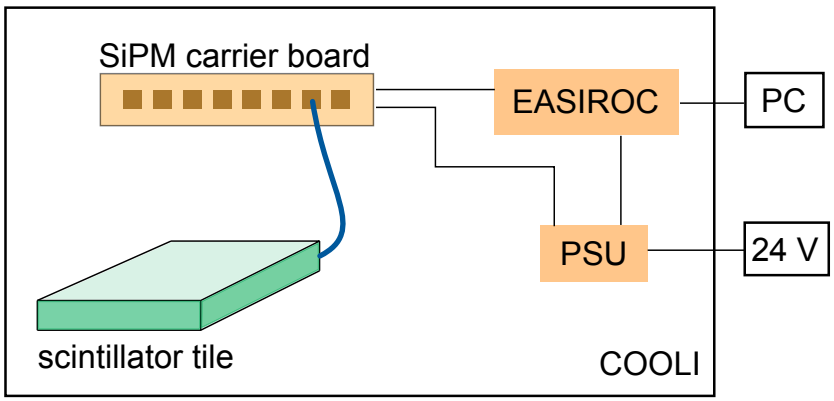

Figure 6.1: Schematics of the test setup for the first measurements with a complete readout chain consisting of one scintillator tile, an clear fibre, an SiPM carrier board, the EASIROC evaluation board and the power supply unit (PSU).

explained, the correct bias voltage is applied to the SiPMs with the PSU and the fine tuning of the 8-bit DACs of the EASIROC. Then, the threshold is set to its lowest value with the 10-bit DAC. The measurement is started for a given measurement period and the event counts are transferred to the FPGA and subsequently read out. This is repeated for all threshold values. Only one channel is measured as the previous chapter has demonstrated a sufficiently high uniformity between channels. The reproducibilty of results of the single channels was proven by repeating the measurements of the previous chapter several times.

Since these are the first measurements taken with a complete Aachen Muon Detector signal chain, the expected signal height of muons can be estimated from simulations. These predict a maximum at around 30-40 p.e. for an ideal detector [67]. It has to be guaranteed that a wide photo equivalent (p.e.) signal range is measured to not miss the signal region. This implies the choice of a reasonable gain control value to fit the dynamic range. The highest amplification factors are excluded as for these the fast shaper saturates for high p.e. pulses. Thus, a moderate gain control value of 8 is chosen. Measurements were taken at a temperature of T=(0.0±0.5)°C.

Analysis of Data

Out of the event counts measured, the event rate is calculated with eq. 5.12 on page 56. The result for a measurement with the complete readout chain compared to a simple dark count scan without scintillator taken under the same settings and external influences is shown in fig. 6.2.

The results are re-binned with a factor of 4 to smooth fluctuations and thus set priority to the relevant characteristics. Additionally, the plotted threshold range is reduced to enlarge these features. The first approximately 8 p.e. steps are identifiable, both for the measurement with scintillator tile and without. The additional contribution of the measurement with the scintillator is due to particles passing through the tile. External light was already excluded as source. Since above the setup lie several cm of concrete in form of ceilings, all charged particles except muons are absorbed. The additional event contribution is thus a signal due to atmospheric muons and to a smaller extend due to natural radioactivity.

For low p.e. pulses, a high dark count rate prevails over the particle signal. From

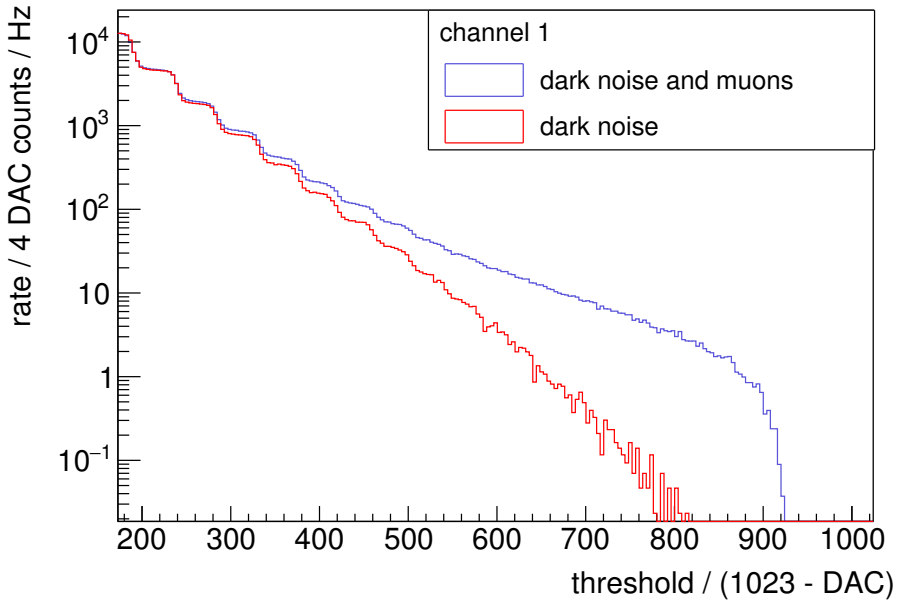

Figure 6.2: Results of the first measurements with a complete AMD readout chain compared to the dark noise rate of the same chain but without scintillator tile and optical waveguide. Results are re-binned with a factor of 4.

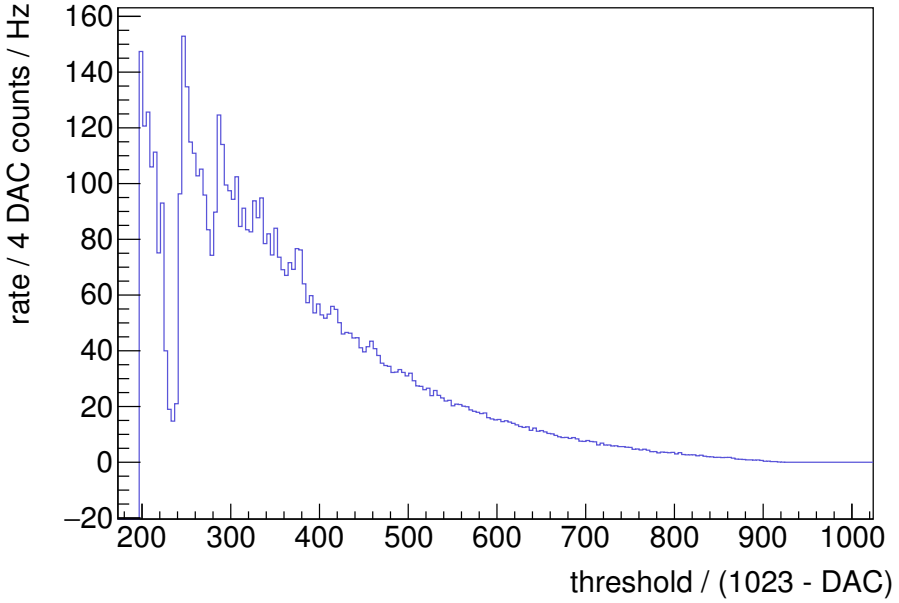

Figure 6.3: Isolated signal of measurements with a complete AMD readout chain. The signal shape resolution is limited due to the method of data taking and the height is influenced not only by the muons but also by changing background rates between the measurements.

about 3 p.e. on, the signal can be distinguished and starts to dominate the spectrum.

To isolate the signal, the background spectrum is subtracted from the data taken with a connected tile. This is shown in fig. 6.3. While in fig. 6.2 a logarithmic y-scale is applied, fig. 6.3 is plotted with a linear scale. In the low p.e. region, single p.e. pulses

can be identified. In the medium to high p.e. region, a continuous decrease is observed to higher p.e. pulses. The decrease is due to a combination of two effects. Firstly, the integrated spectrum is observed as a low threshold also triggers high p.e. pulses which decreases to higher pulses per definition. Secondly, the number of events itself decreases to higher pulse heights. The exact form is strongly influenced by the background rate subtraction as the temperature between both measurements changes.

The rate of the signal can only be compared in the order of magnitude with expectations because already small temperature variations between measurements of the dark count rate and the complete readout chain measurement result in perceptible background rate changes, especially at low threshold values. These are propagated to the isolated signal rate. The expected integral intensity of vertical muons at ground level is approximately 70 $\mathrm{m^{-2}\,s^{-1}\,sr^{-1}}$ [4]. By integrating over the geometrical acceptance and for a $30\times30\,\mathrm{cm^2}$ tile, the rate amounts to approximately 800 muons $\mathrm{min^{-1}}$ or 13 Hz. Here, the observed rate is about (150/4) Hz≈40 Hz. This rate difference is mainly driven by the difference in the dark noise and is thus not the rate of a pure signal. A more precise measurement with a setup which is less influenced by the dark count rate of the SiPMs is essential to compare the measured rate with the expected rate.

In conclusion, a muonic signal is measured and it can be separated from the background rate. Due to the method of data taking, temperature differences between the measurements exist, inhibiting a complete subtraction of the dark count rate. This limits the determination of the form of the signal. Additionally, the high dark count background prevents the AMD from triggering itself for low thresholds. In contrast, for high pulses, the detector can trigger itself since the background rate is negligible.

As long as no signal amplification is attained, e.g. by increasing the light yield with another scintillator, better couplings, etc., or alternatively the noise level is suppressed, e.g. of the SiPMs and EASIROC or by using a coincidence, the AMD is dependent on an external trigger. For the operation of the Aachen Muon Detector, the SD stations of the Pierre Auger Observatory can provide this trigger.

The rate of detected atmospheric muons is to be determined more precisely. Thus, an alternative setup for the determination of the signal shape and rate is applied, see chapter 6.2.

6.2 Determination of the Atmospheric Muon Signal Distribution

The detection of the atmospheric muon signal distribution is an important link between measurements and simulations of the detector response. Thus, a detailed analysis helps to improve the understanding of the readout chain and its single components.

Measurement Setup

A schematics of the setup is shown in fig. 6.4.

Two wrapped scintillator tiles are stacked and connected to the SiPM carrier board with optical fibres of equal lengths. The power supply unit provides SiPMs and the EASIROC evaluation board with the necessary voltages of approximately 70 V and 6.5 V, respectively. The setup is placed inside the COOLI and the temperature is regulated to 25°C as measured at the SiPM carrier board or 28°C as measured at the

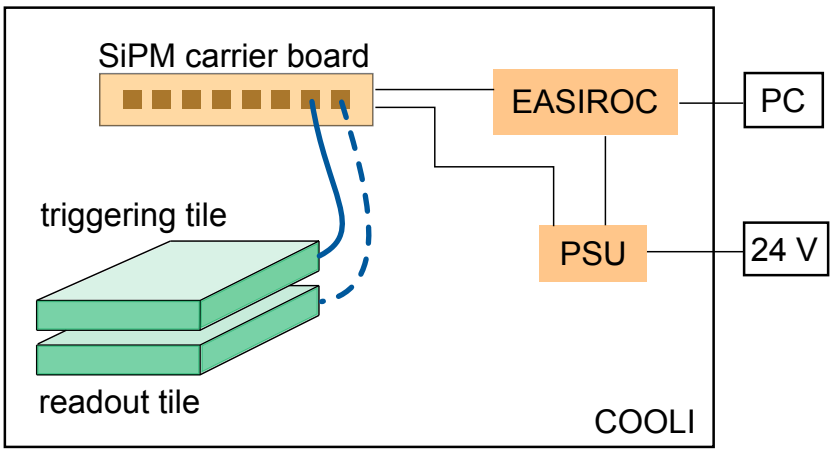

Figure 6.4: Schematics of the test setup for the detection of the atmospheric muon signal distribution. A coincidence trigger is used for data taking. One tile serves only as trigger to reduce the dark noise. The second trigger chain is once read out with a connected tile for the signal detection and once without a tile for background rate determination.

EASIROC. The temperature measured at the chip is always higher since the chip heats up slightly during its operation.

Measurement Procedure

A coincidence trigger of both tiles with 50 ns time window is applied for the data taking. For the readout process, the SiPM signals are passed into the EASIROC where they are processed by firstly amplifying the signal with a pre-amplifier and subsequently formed by the slow shaper. The integrated analogue signal is temporarily stored at its peaking time until the FPGA sends the read signal. From the EASIROC, it is send into a 12-bit ADC for digitisation of the pulse height which finally serves as an energy measure. A detailed description of the working principle and interplay between EASIROC, FPGA and ADC is given in chapter 3.4.2. Following settings are written into the slow control: The internal gain control value of the EASIROC is set to 1. This reduction in dynamic range is possible because the measurement in chapter 6.1 already revealed that the minimum ionising particle (MIP) peak is expected in a low p.e. region (i.e. in between 5 and 15 p.e.). By setting a high amplification factor (low gain control value), the resolution of the peak is increased. The peaking time of the slow shaper is set to 125 ns which is the largest integration time where still the single p.e. pulses are identifiable. Processed pulses of a certain number of cell breakdowns cause the same signal either if they occur simultaneously or within the shaping time, thus the largest number of muons possible is taken into account. For the detection of single atmospheric muons, this is a less important argument. Here, the integration time must exceed the signal propagation delay of about 20 ns in the detector [68]. But for the detection of muons in air showers a long integration time becomes especially important, as the dead time of the AMD of 16 µs allows for only one measurement per shower. From the first EAS particle entering the detector until 90% of the particles which hit the sensitive area have penetrated it, 500 ns pass [68]. This peaking time is unavailable. Instead, in 125 ns approximately 50-60% of the particles are detected [68]. Here, the signal propagation

delay of 10-20 ns, depending on optical fibre length, is included.

As no detailed analysis of the dark count spectrum for a gain control value of 1 has been performed, one measurement is taken at the temperature where also the atmospheric muon signal distribution peak is measured to quantify the dark count rate. The discriminator threshold is set to 2.5 p.e. or (1023-270) DAC counts as from 3 p.e. onwards the signal starts dominating over the background (c.f. chapter 6.1). A low threshold value is preferable to keep the signal rate of the detector high. But it has to be high enough to suppress dark counts so these do not dominate the output.

A measurement run of approximately 18.5 h is started. The ADC values are continuously transferred to a PC. After taking a first measurement where both tiles are connected, one of the tiles is disconnected. Thus, the coincidence trigger consists of one chain with disconnencted tile and a second chain with connected tile. All other conditions are kept constant and a second measurement run is started. In this second run, the readout chain with the disconnected tile is read out, thus giving a dark count analysis. By keeping the conditions constant, the same dark count rate and pulse height is measured as during the data taking processing with two connected scintillator tiles. Thus, it can simply be subtracted in the analysis.

Analysis of Data

The results of the measurements, once with connected tile in the readout chain, once with disconnected tile, are shown in fig. 6.5.

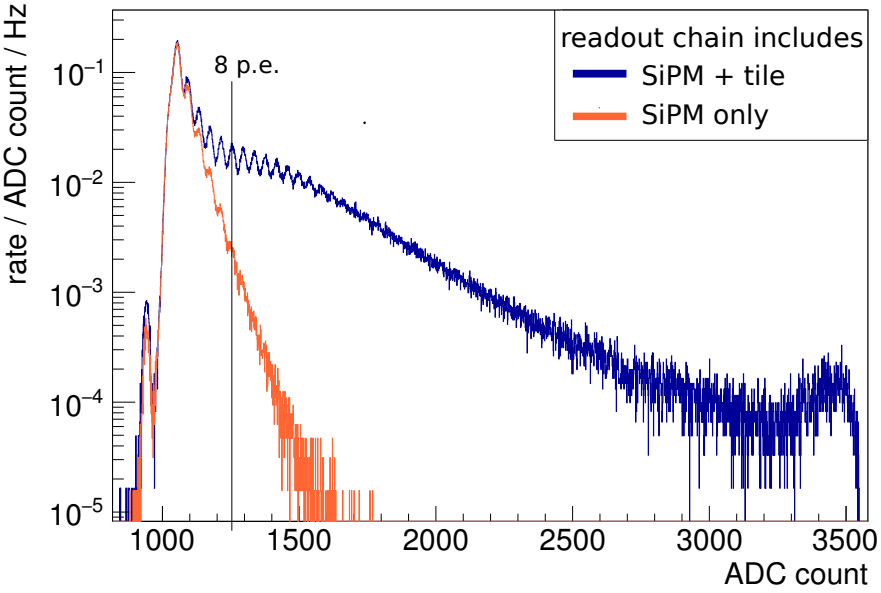

Figure 6.5: Measurement of the pulse height distribution of atmospheric muons. One signal chain with connected tile serves as trigger while a second chain is read out. In case of the orange trace, no scintillator tile is connected to the readout chain and only the background is measured. For the data taking of the blue trace, a tile is connected to the second chain. Already published in [63].

In the measured spectrum, the single p.e. pulses are identifiable. Additionally, a background peak at 0 p.e. occurs at an ADC count of around 950. This is due to a

faulty coincidence caused by electronic noise in the fast shaper line while the signal pulse in the slow shaper still lies below the normal SiPM pulses. As described before, the background spectrum is measured to be subtracted from the signal plus background trace. The resulting signal shape is shown in fig. 6.6.

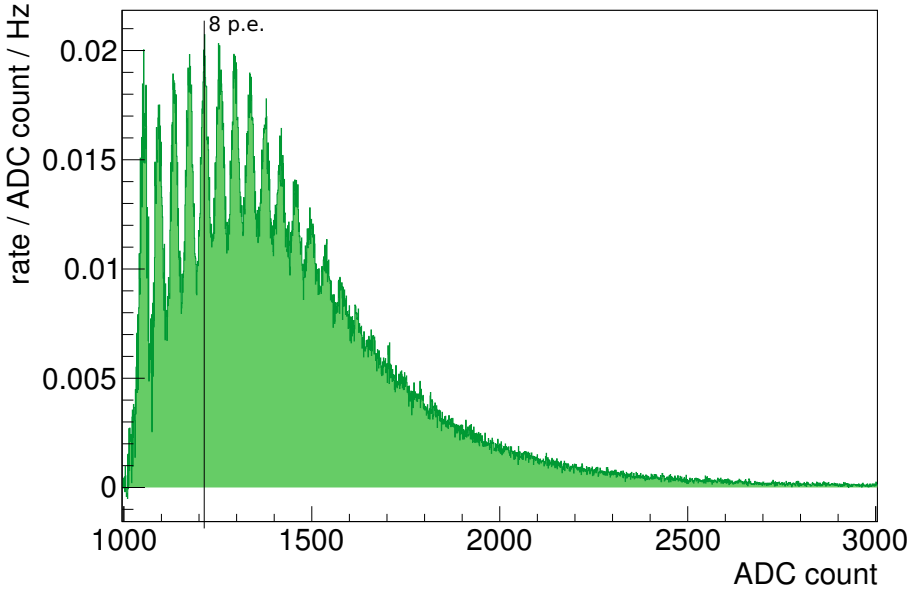

Figure 6.6: Isolated muon signal produced by subtracting the background spectrum from the measurement with connected tile, as shown in fig. 6.5. The individual p.e. pulses due to SiPM characteristics are clearly visible. Due to the application of a twofold coincidence, the dark count rate is highly reduced giving a clearer shape of the muon signal than in fig. 6.3. Already published in [63].

In this method of application, the pure signal peak is shown. Besides the overall shape, the single p.e. pulse heights are visible which result from the SiPM single photon counting characteristics. The signal is only caused by atmospheric muons. The hadronic and electromagnetic components are absorbed since the setup is located within a building with several cm of concrete above it where both components are absorbed. Muons have a broad minimum ionising particle region, see fig. 6.7. Compared to the spectrum of muons at ground level, see fig. 6.8, virtually all muons carry the MIP region energy. The ones which are of higher or lower energies are mostly absorbed by the concrete or shifted to energies in the MIP region.

To identify the maximum of the atmospheric muon peak, the results of fig. 6.6 are plotted in a binned version. The signal corresponding to each single p.e. peak are thus summarised in one bin, see fig. 6.9. Here, it becomes clear that the muon signal follows a Landau distribution. From fig. 6.9, the maximum is determined to 8-9 p.e.. Simulations of the Aachen Muon Detector predicted a peak in the region around 30-40 p.e. [67], depending on the length of the optical fibre. The difference can be explained since in the simulations, an ideal detector was implemented. Thus, no fibre impurities or damages, polishing effects, light losses at couplings or other output reducing effects are implemented yet.

Besides the shape of the signal, the rate is determined and compared to expectations. The measured rate for a coincidence trigger with two connected tiles is 19.6 Hz and with

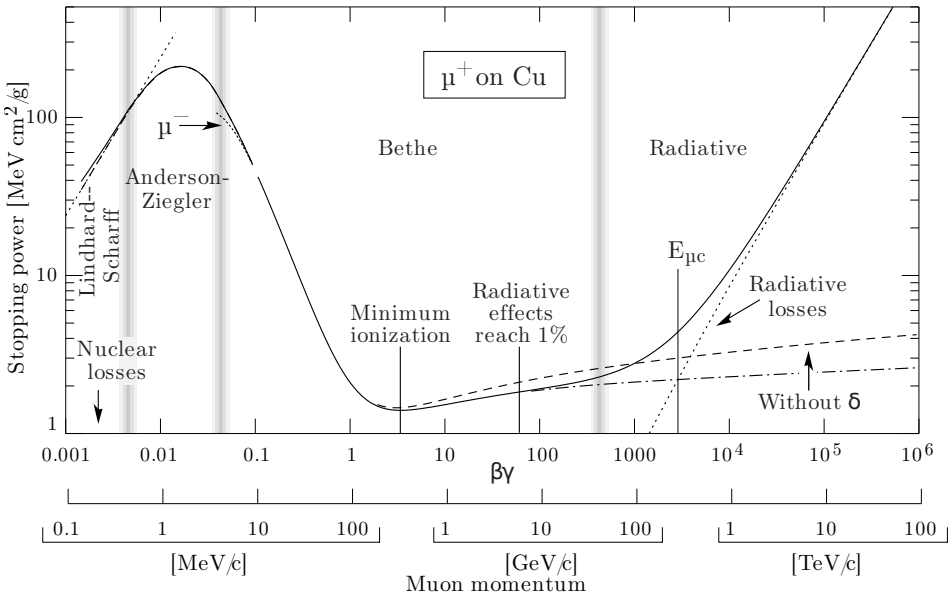

Figure 6.7: Stopping power of muons in copper. The region with similar stopping powers as at the minimum ionising particle energy reaches from approximately 0.1 to 100 GeV. The energy band is similar for air but the stopping power values change (which are not considered any further here). Taken from [4].

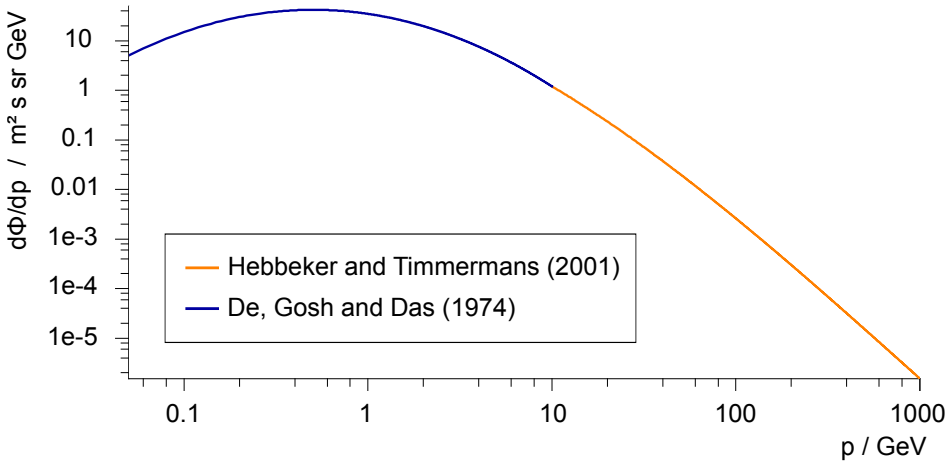

Figure 6.8: Differential flux of muons over energy. The spectrum is combined of data in the low energy (blue) [69] and high energy (orange) [70] range. The fits are compatible within the stated uncertainties. Taken from [71].

only one connected tile 10.3 Hz. In first approximation, the rates are subtracted giving a signal rate of 9.3 Hz. The systematic uncertainty is driven by the dead time of the detector due to signal processing and bias voltage adjustments of the SiPM to correct for varying temperatures and is estimated to about 5% [58], thus giving 0.5 Hz. The statistical uncertainty is given by the Poissonian nature of the distribution and is with 0.01 Hz negligible. This is not completely correct as coincidence triggers caused by a muon signal and noise event in the other SiPM or vice versa are not distinguishable from signal pulses. But for the purpose of testing the compliance in the order of magnitude this method is perfectly sufficient.

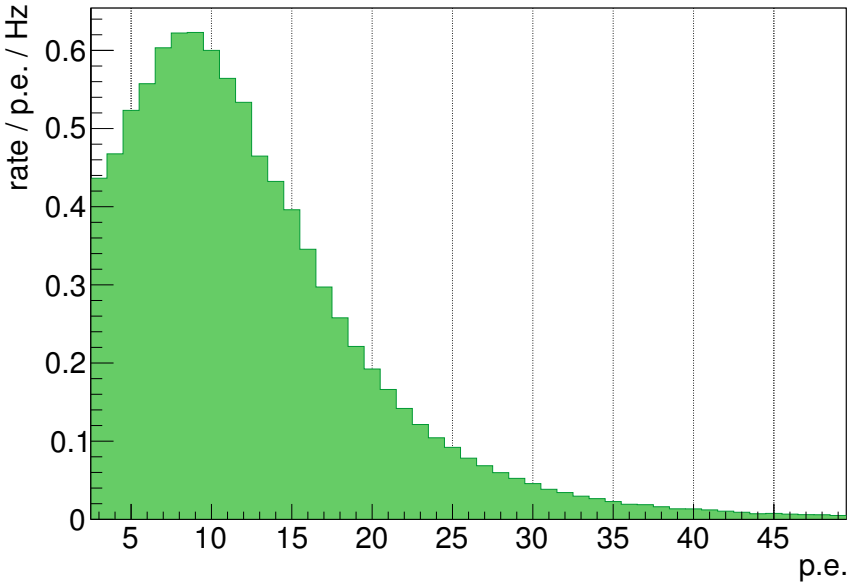

Figure 6.9: Binned muon signal. The data of fig. 6.6 is assigned to p.e. pulses. The most probable value of a muonic signal is 9 p.e.. Already published in [63].

The expectation for the vertical integral flux of muons with energies $E \geq 1\,\mathrm{GeV}$ amounts to about 70 $\mathrm{s^{-1}\,m^{-2}\,sr^{-1}}$ [4]. This corresponds to a rate per area of approximately 0.88 $\mathrm{min^{-1}\,cm^{-2}}$ which can be calculated by integrating over the geometrical acceptance. Consequently, for data taking with one scintillator tile of $30\times30\,\mathrm{cm^2}$ and no light loss effects, the expected rate is 13.2 Hz. Since in the measurement setup two tiles are placed directly above each other, only small variations from this rate are expected. Hence, this rate is used as expectation for the coincidence measurement as well. For both readout chains, the trigger efficiency is smaller than 100%. The trigger efficiency states the ratio of the photon distribution which is above the discriminator threshold. Light loss effects at couplings shift the distribution to lower p.e. values and a higher discriminator threshold lets only higher signal pass. Therefore, these effects decrease the trigger efficiency. The trigger efficiency of both readout chains is determined to roughly $\epsilon_{\mathrm{trigger}}$ =85% [58]. Thus, the expected rate reduces to

$$R = 0.88\,\mathrm{min^{-1}\,cm^{-2}} \cdot 30 \cdot 30\mathrm{cm^2} \cdot \epsilon^2_{\mathrm{trigger}} = 9.5\,\mathrm{Hz} \quad . \tag{6.1}$$

The uncertainties on R are difficult to estimate since many effects influece the rate. First, the rate per area is given for the vertical flux at sea level but the detector is located at about 170 above sea level in a multi-storey building with concrete ceilings. Additionally, the two scintillator tiles have, other than assumed, a certain vertical distance such that not all particles pass through both tiles. Thus, the uncertainty is conservatively estimated to 10 % of the rate per area. The uncertainty on the trigger efficiency is estimated to 5 %. Compared to these effects, the uncertainties on tile size are negligible. The uncertainties on the rate are calculated with Gaussian error propagation. Hence, the expected rate is $R = (9.5 \pm 1.1)\,\mathrm{Hz}$. Comparing the expected and the measured value, the measured value of $(9.3\pm0.5)\,\mathrm{Hz}$ is compatible with expectations within the uncertainties. Therefore, this is taken as proof for the proper functioning of

the detector.

6.3 Development and Application of an AMD Test Measurement Shelf

Besides the measurement of the pulse height distribution of atmospheric muons further test measurements are essential to test whether the detector response is as expected. This includes studies of the angular dependence of the muon rate and trigger efficiency, but also the effects of wrapping the scintillator tiles (see chapter 3.1) or comparing different connections between the fibres, such as silicon pads, optical glue or simply air gaps. For these measurements, an easy access test setup is developed in cooperation with the mechanical workshop of the III. Phys. Inst. of RWTH Aachen University. It allows for quick replacements and changes of the components. The basic idea is to operate eight tiles above one another instead of next to each other. With this coincidence setup, a selection of tiles can serve as trigger and the system can be operated without an external trigger system while still providing an almost pure muon signal.

Measurement Setup

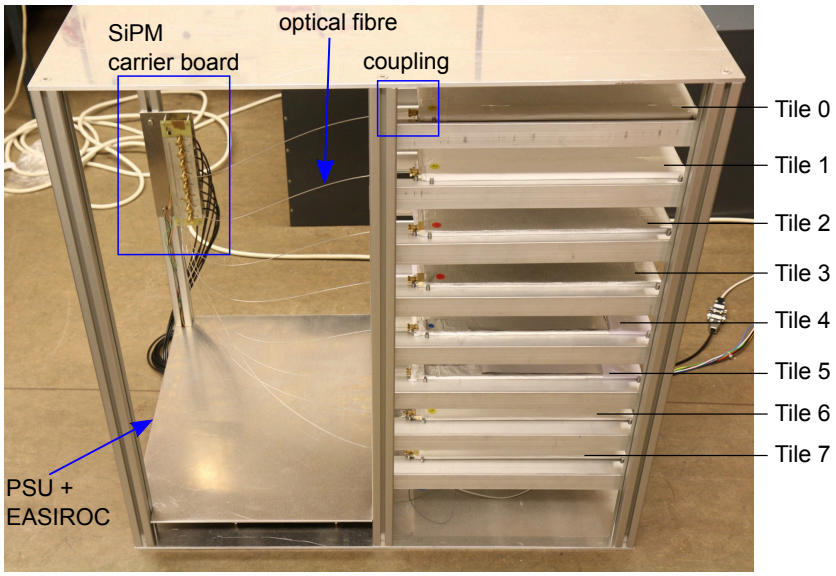

Figure 6.10: Aachen Muon Detector shelf for studying the detector response without an external trigger. Some tiles are used as trigger. By changing the position of the tiles used as trigger, e.g. the angular dependence of the muon rate can be determined.

The test setup consists of an aluminium framework into which up to eight scintillator tiles and their corresponding readout chains can be inserted separately. Thus, the setup includes up to eight wrapped tiles with inserted WLS fibres, the according number of optical fibres, one SiPM carrier board, the EASIROC board and the power supply unit (PSU). Photos of the setup are shown in fig. 6.10 and fig. 6.11. All optical fibres have the same length to avoid light absorption differences which influence the results. Henceforth, the setup is referred to as AMD shelf. The tiles are inserted into the rails of the shelf and are held in position by metal pins. A spatial distance of 8 cm between the

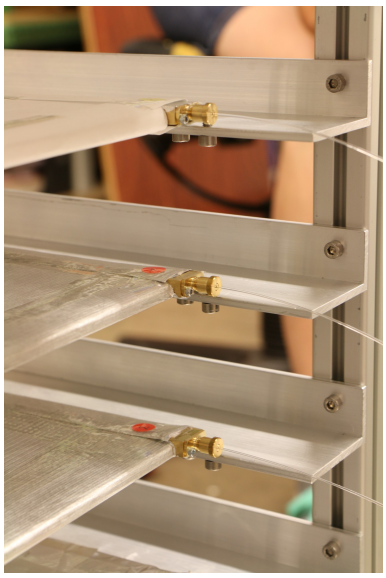

(a) Coupling WLS to optical fibre.

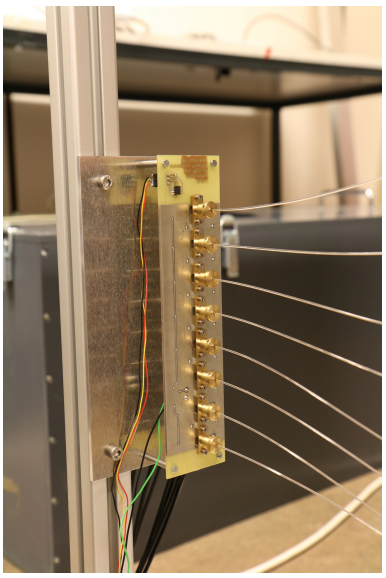

(b) SiPM carrier board and coupling WLS to optical fibre.

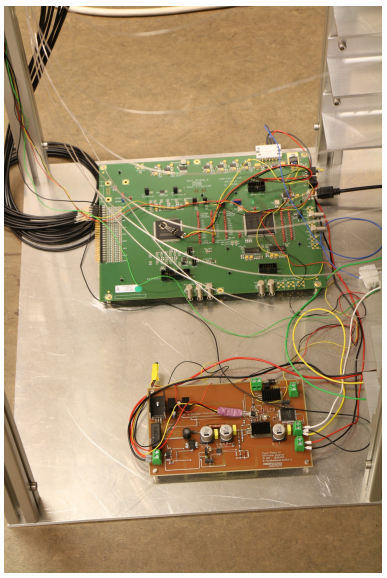

(c) EASIROC evaluation board and PSU mounted at the bottom of the shelf.

Figure 6.11: Detailed view of the couplings and position of the electronics in the AMD shelf.

rails is chosen to be able to insert absorbers in future test measurements. Additionally, measurements at multiple angular acceptance values are enabled by setting coincidence triggers for tiles with different vertical distance. The electronics can be stored at the bottom of the shelf. They are protected by an extra aluminium layer from falling elements during mounting or dismounting of single components. Since the minimal bending radius of all clear waveguides has to be complied, the SiPM carrier board sits at medium level at one of the outer struts instead of at the bottom with the other electronics. The whole AMD shelf is covered with a black lightproof cover.

Measurement Procedure

As one exemplary measurement with the AMD shelf, the effect of different wrappings is evaluated. For this purpose, the scintillator tiles are wrapped in different materials. Four are wrapped into Tyvek, two into Tyvek with additional UV coating and two into Teflon, see chapter 3.1. The sequence of tiles top down is: Tyvek, Tyvek, Teflon, Teflon, Tyvek (UV), Tyvek (UV), Tyvek, Tyvek. Their numbering top down is 0 to 7.

The measurement procedure is similar to the detection of the determination of the pulse height distribution of atmospheric muons in chapter 6.2. Thus, it is not described in detail again but only briefly. As the AMD shelf does not fit into a COOLI, the temperature is given by the conditions by the facilities it is located in, in the case of the subsequent measurement it amounts to T$\approx$ 25°C. The PSU is turned on to supply the EASIROC board and the SiPMs with power. Then, all settings are written into the slow control: The internal gain control value of the EASIROC is set to 1, the slow shaper is set to 125 ns, the measuring time is t$\approx$12 days and the trigger conditions are set. To reduce the noise level to a negligible level, four tiles (number 0, 3, 5, 7) are used for a coincidence trigger. Between uppermost triggering tile 0 and undermost

triggering tile 7 are 54 cm. The 10-bit DAC of the EASIROC is set to a threshold of 2.5 p.e.. The data processing is analogous to chapter 6.2 with EASIROC, FPGA and subsequent readout.

Analysis of Data

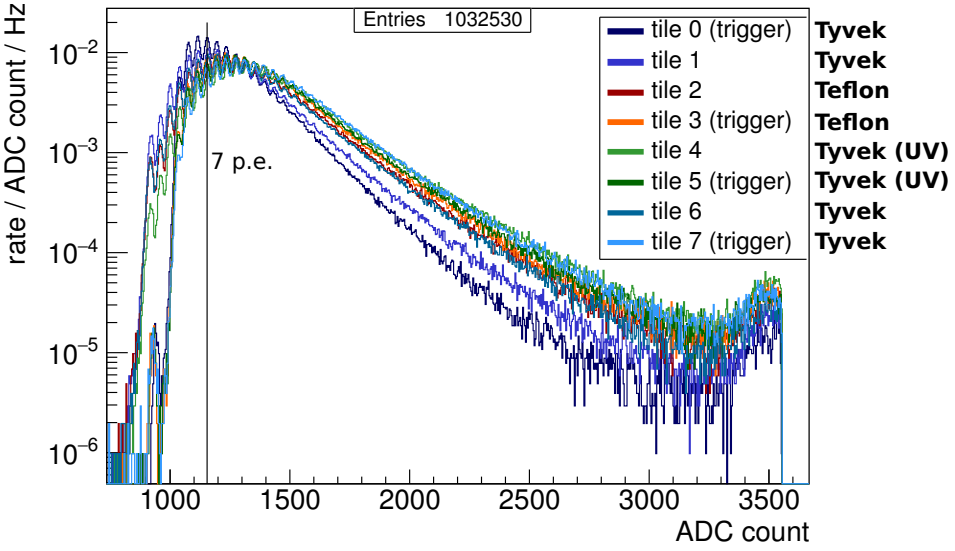

Figure 6.12: Measurement of muonic MIP peak with 8 tiles above one another. The numbering corresponds to the position in the shelf, with 0 as the highest. Four tiles serve for the coincidence trigger. Different wrapping techniques are applied.

The measurement results are shown in fig. 6.12. Since a fourfold coincidence trigger is applied, the traces show a pure signal. The signal of the channels which are used for the trigger start above the threshold of 2.5 p.e.. Additionally, they show an electronic noise peak which is caused by faulty triggers at around 950 ADC counts. All channels which are not used for triggering on muons already show the 1 p.e. peak.

Above the AMD shelf are several cm of concrete absorbing the greatest part of electromagnetic and hadronic particles. Thus, the signal originates from atmospheric muons of the minimum ionising particle (MIP) energy range, as explained in chapter 6.2. Single p.e. steps are identifiable. Hence, the most probable value (MPV) of the peak's position can be identified. An enlarged plot of the critical signal range is shown in fig. 6.13. Here, the MPV is determined to a value between 6 and 9 p.e., depending on the channel.

To determine the effect of different wrapping materials, Tyvek is plotted in blueish colours, Tyvek with UV coating in green and Teflon in orange and red. No explicit dependence is found between the wrapping materials. This complies with the expectations when comparing the result to table 3.1 which predicts similar reflection coefficients for Teflon and Tyvek. The angular distribution of photon reflection, see fig. 3.6, does not have any effect for the light yield of the AMD. But the individual tiles show outputs of different heights and different positions of the most probable value. To identify whether the effect originates from the tiles or the readout channels, the position of the tiles within the AMD shelf is changed. Similar results are measured for the individual tiles at different readout chains. Thus, the effect is caused by the scintillator tiles or their wrapping and not the chains. Whether the wrapping which is done manually

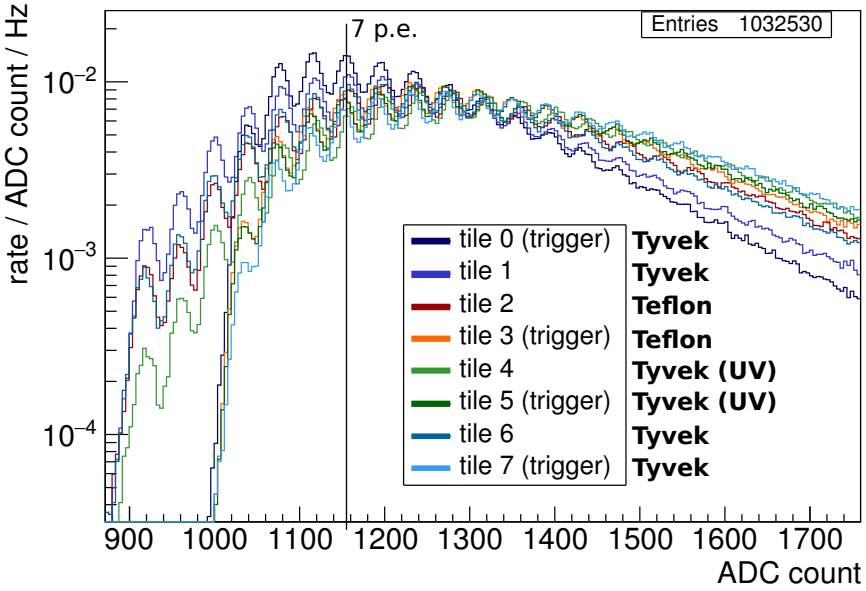

Figure 6.13: View inside the muonic MIP peak region (compare fig. 6.12). The individual p.e. pulses are identifiable. The MPV lies between 6 and 9 p.e., depending on the tile and corresponding readout chain.

causes different outputs or the tiles with pasted WLS fibres are the origin of it will be issue of further tests. Tests have been performed without any wrapping, but in this configuration no muonic signals were observed. Thus, this is an inappropriate method to test whether manufacturing differences in the tiles cause varying outputs.

Summarising, the minimum ionising particle peak for atmospheric muons is observed at p.e. values of around 6 to 9. Wrapping the tiles is essential for increasing the light yield to a level for the detection of the MIP peak. All tested wrapping materials show similar results in the light output, making the easiest in application, the Tyvek, the current method of choice.

As already done for the twofold coincidence trigger, the measured rate is compared to the expected one. Here, a rate of 1.035 Hz is measured. The statistical uncertainty results of the Poissonian nature of the distribution and amounts to 0.001 Hz. The systematic uncertainty is driven by dead time effects. Since the dead time effects due to the SiPM voltage adjustment could be exluded out of the rate, only the dead time for signal processing contributes. This is estimated to about 0.5 % of the signal rate [58] and thus amounts to 0.005 Hz. Consequently, the observed rate is $(1.035 \pm 0.001 \pm 0.005)$ Hz. The distance between the uppermost and the undermost tile defines the angular acceptance of the incoming particles. A Monte Carlo simulation is written to determine the percentage of muons hitting the undermost tile under the condition of firstly hitting the uppermost tile. The starting points and directions of the particles are generated in Cartesian and spherical coordinates with a random number generator, respectively. The polar angle ϕ is uniformly distributed from 0 to 2π. For the zenith angle θ, the particle flux dependence on θ and the solid angle of incoming particles have to be taken into account. The zenith angle dependence of the differential particle flux

$\mathrm{d}\Phi/\mathrm{d}p(p,\theta)$ of muons at sea level is given by

$$\frac{\mathrm{d}\Phi}{\mathrm{d}p}(p,\theta) = \frac{\mathrm{d}n(p,\theta)}{\mathrm{d}\Omega\,\mathrm{d}p\,\mathrm{d}S\,\mathrm{d}t} = \frac{\mathrm{d}\Phi}{\mathrm{d}p}(p)\cdot\cos^2(\theta) \tag{6.2}$$

where p is the momentum of the particle, n is number of particles, Ω is the solid angle, S is the area and t is the time [72]. Consequently, a uniform distribution in $\cos^2(\theta)\cdot\sin(\theta)$ is generated. Out of these two angles and the distance between the tiles, the coordinates of the particle passing through the plane of the undermost tile are calculated. The ratio of events hitting the bottom tile to all events amounts to ξ =11%. This is the relative geometric acceptance. To get the number of expected events, the expected flux per area is multiplied by the tile size, the acceptance ξ and the trigger efficiencies $\epsilon_{\mathrm{trigger}}$ of four tiles as it is a fourfold coincidence. Consequently, the expected rate is

$$R = 0.88\,\mathrm{min}^{-1}\,\mathrm{cm}^{-2}\cdot 30\cdot 30\mathrm{cm}^2\cdot\xi\cdot\epsilon_{\mathrm{trigger}}^4 = 1.18\,\mathrm{Hz} \tag{6.3}$$

where $\epsilon_{\mathrm{trigger}}$=0.95 [58]. The same assumption for the uncertainties are made as in the previous calculation for the twofold coincidence. Only the uncertainty on the trigger efficiency is reduced to 1% as the determination is more precise [58]. Thus, the expected rate amounts to $R = (1.18 \pm 0.12)\,\mathrm{Hz}$ The trigger efficiency is higher than in chapter 6.2 as the light loss factors were reduced by using new optical fibres with nicely polished exit surfaces, and special care has been taken when mounting the optical fibres in the couplings. This was possible due to the experience gained with the measurements in chapter 6.2. Expected and measured rates comply with $(1.18 \pm 0.12)\,\mathrm{Hz}$ and $(1.035 \pm 0.001 \pm 0.005)\,\mathrm{Hz}$ within the uncertainties, which is a good proof of the functioning of the detector.

As a final remark it should be noted that the measured atmospheric muons serve as proof of functioning of the detector. They are a good option for testing the response as their rate is much higher than the occurrence of extensive air showers. For the operation of the Aachen Muon Detector, atmospheric muons are background events which cause fake triggers.

Chapter 7

Conclusion and Outlook

The Aachen Muon Detector (AMD) is dedicated to the data taking of the muonic component of extensive air shower experiments. A new design focuses on the conditions set by the detection of muons in remote regions. These include the time course of arrival of the particles, the amount of particles expected and also an operation in the Pampa Amarilla of Argentina.

A total of 64 scintillator tiles each with $30 \times 30\,\mathrm{cm}^2$ form the sensitive area of the detector. This highly modular design enables arrival direction reconstruction, increases both light yield and dynamic range and enlarges the mechanical stability compared to a single scintillator of the same sensitive area. For further improvements of the light yield, the tiles are wrapped into Teflon or Tyvek. Wavelength shifting (WLS) fibres are glued into the tiles for light collection. These fibres are coupled to optical waveguides which conduct the light onto photosensors.

A test setup was developed to test the stability of the mechanical couplings and temperature effects on the fibres' light output. The stability of the couplings completely fulfills the requirements. The WLS and optical fibre were exposed to a temperature cycle typical for the Pampa Amarilla of between approximately 0°C and 50°C. No changes in the output were found, but before excluding this completely, the fibres have to be exposed to multiple temperature cycles. Already new fibres show impurities in the core and the cladding which can cause light loss effects. To enlarge the light yield, the fibre ends are polished. During this procedure, the cladding can be damaged with differing severity.

Silicon photomultipliers (SiPMs) are used as photosensors. They provide several advantages compared to photomultiplier tubes. Most beneficial is the resolution of single photons detected as cell breakdowns. As noise effects can also cause breakdowns, the initiation event is referred to as photo equivalent (p.e.). Further benefits include their small size, low operation voltage and robustness. To keep their characteristics stable for varying temperatures, their temperature is measured and their bias voltages are adapted continuously. A power supply unit (PSU) supplies the SiPMs with a voltage of approximately 70 V. The Extended Analogue SI-pm ReadOut Chip (EASIROC) is a specialised front-end ASIC for signal processing and fine tuning of the bias voltage of SiPMs. The fine tuning occurs for each channel individually with 8-bit DACs. Two reference sources allow for a fine tuning range between 0 and 4.5 V. The output of the DACs is determined and temperature dependent changes are quantified. Start values for each bit and the maximal output have to be quantified for each channel but the temperature dependence is equal for all channels.

The EASIROC board itself is powered by the PSU, too. A discriminator allows for the setting of a threshold in a 10-bit range. Measurements were taken with connected SiPMs to determine the dark count rate at each DAC count. The scans show clear steps which correspond to nearly discrete pulse heights at the according p.e. steps. This rate

and the position of p.e. steps is temperature dependent. Both effects were quantified and for the p.e. steps a correction equation was developed. Thus, in the operation of the AMD the DAC count of the threshold can be calculated for a given temperature and p.e. step. Noise effects occur when the USB connection of the EASIROC is active in the low threshold range which can be reduced to a minimum when deactivating the connection during data taking and only activating it for data readout. For all measurements taken, the different channels show a uniform output. Consequently, after checking for noise effects for all channels, the characterisation and analysis of the dark count rate and the p.e. step position is sufficient to be performed with one channel only.

Flow charts give an introduction manual for future characterisation and analysis procedures of similar setups.

After the performance of single components and subsystems were tested, a new measurement setup for further tests of the output with a whole detector chain was developed, the Aachen Muon Detector shelf. Here, 8 tiles can be placed above each other with distances of 8 cm. A coincidence trigger implemented in the EASIROC allows for the AMD shelf to trigger itself. Thus, the signal height distribution in p.e. of the atmospheric muon signal was measured. Wrapping the tiles is essential for detecting the signal but whether Teflon or Tyvek is used makes no visible difference. The distribution of the minimum ionising particle peak of atmospheric muons follows a Landau distribution with a most probable value (MPV) of 6-9 p.e. in the current configuration. The measured rate with a twofold coincidence with the tiles directly placed above each other amounts to $(9.3pm0.5)$ Hz which complies with the expectation of (9.5 ± 1.1) Hz. Similarly well compares the measured rate of (1.18 ± 0.12) Hz with a fourfold coincidence with a maximal spacing of triggering tiles of 56 cm to the expectation of $(1.035\pm0.001\pm0.005)$ Hz.

The individual readout chains are working well after the single components have been analysed within this thesis and all temperature dependencies are corrected for in the software and analysis programmes.

Future improvements will include an increase of the light yield and therefore the MPV in the muon distribution. Different wrapping techniques, melted fibre ends instead of polished ones and filling the air gap between fibre ends, and between fibre end and SiPM with either silicon pads or optical glue are promising options to shift the output to higher values.

Additionally, further test measurements will be performed with the AMD shelf. These include studies of the angular dependence of the arriving atmospheric muons by changing the vertical distance of triggering tiles, determining the trigger efficiency and the attenuation length of the muons by placing absorbers between the tiles.

Once the performance is characterised with atmospheric muons in the AMD shelf, the components will be placed in the steel housing of the AMD and the prototype will be finished for data taking of the muonic component of extensive air showers.

Appendix

1 Start values 8-bit DAC: Maximal Output and Bits

channel	**U_{max}** [V]	**Bit 0** [V]	**Bit 1** [V]	**Bit 2** [V]	**Bit 3** [V]	**Bit 4** [V]	**Bit 5** [V]	**Bit 6** [V]	**Bit 7** [V]
0	4.508	0.011	0.016	0.039	0.075	0.194	0.333	0.706	1.224
1	4.512	0.018	0.027	0.036	0.085	0.157	0.356	0.646	1.265
2	4.517	0.011	0.018	0.050	0.079	0.162	0.353	0.650	1.294
3	4.508	0.007	0.017	0.044	0.089	0.164	0.348	0.647	1.310
4	4.499	0.011	0.025	0.040	0.091	0.150	0.365	0.624	1.319
5	4.496	0.010	0.025	0.046	0.085	0.165	0.351	0.649	1.252
6	4.509	0.012	0.033	0.038	0.075	0.169	0.321	0.673	1.253
7	4.503	0.007	0.020	0.041	0.078	0.184	0.348	0.645	1.273
8	4.494	0.014	0.021	0.042	0.092	0.167	0.374	0.596	1.274
9	4.498	0.017	0.017	0.042	0.078	0.170	0.359	0.704	1.310
10	4.485	0.008	0.027	0.040	0.094	0.175	0.338	0.668	1.227
11	4.515	0.010	0.026	0.041	0.084	0.189	0.350	0.682	1.240
12	4.511	0.011	0.025	0.047	0.080	0.171	0.324	0.661	1.219
13	4.515	0.012	0.022	0.042	0.077	0.180	0.325	0.639	1.246
14	4.500	0.010	0.020	0.044	0.096	0.155	0.347	0.664	1.242
15	4.506	0.014	0.018	0.046	0.080	0.161	0.344	0.660	1.240
16	4.498	0.009	0.023	0.034	0.087	0.156	0.324	0.668	1.226
17	4.493	0.010	0.026	0.043	0.081	0.169	0.353	0.657	1.249
18	4.505	0.013	0.021	0.028	0.074	0.169	0.329	0.647	1.256
19	4.509	0.013	0.027	0.044	0.081	0.160	0.325	0.630	1.244
20	4.489	0.012	0.016	0.043	0.072	0.172	0.317	0.656	1.243
21	4.503	0.013	0.019	0.048	0.090	0.168	0.330	0.682	1.153
22	4.501	0.006	0.014	0.036	0.075	0.186	0.323	0.667	1.237
23	4.505	0.005	0.023	0.037	0.085	0.166	0.336	0.649	1.309
24	4.498	0.008	0.018	0.038	0.091	0.153	0.330	0.660	1.260
25	4.495	0.011	0.021	0.038	0.087	0.149	0.331	0.643	1.296
26	4.495	0.008	0.020	0.037	0.094	0.161	0.330	0.617	1.228
27	4.516	0.011	0.019	0.038	0.082	0.167	0.334	0.633	1.226
28	4.509	0.010	0.023	0.044	0.066	0.175	0.346	0.659	1.235
29	4.505	0.010	0.020	0.037	0.070	0.142	0.334	0.613	1.197
30	4.495	0.012	0.021	0.048	0.071	0.192	0.355	0.635	1.223
31	4.499	0.017	0.025	0.041	0.085	0.159	0.364	0.679	1.461

Table 1: Maximal output and bit values for each channel at (27.1±0.4)°C for the external reference source.

channel	**U_{max}** [V]	**Bit 0** [V]	**Bit 1** [V]	**Bit 2** [V]	**Bit 3** [V]	**Bit 4** [V]	**Bit 5** [V]	**Bit 6** [V]	**Bit 7** [V]
0	2.504	0.012	0.016	0.041	0.079	0.212	0.363	0.764	1.328
1	2.510	0.019	0.031	0.038	0.089	0.169	0.383	0.697	1.350
2	2.515	0.012	0.019	0.053	0.087	0.173	0.378	0.698	1.392
3	2.504	0.008	0.018	0.046	0.095	0.179	0.380	0.698	1.402
4	2.495	0.012	0.028	0.045	0.096	0.160	0.390	0.678	1.423
5	2.493	0.012	0.032	0.049	0.090	0.177	0.379	0.697	1.354
6	2.505	0.013	0.035	0.040	0.081	0.181	0.345	0.729	1.360
7	2.502	0.008	0.023	0.044	0.084	0.202	0.373	0.694	1.370
8	2.491	0.014	0.022	0.045	0.101	0.178	0.404	0.641	1.368
9	2.495	0.018	0.019	0.046	0.084	0.187	0.386	0.753	1.407
10	2.483	0.009	0.028	0.044	0.102	0.188	0.359	0.723	1.313
11	2.511	0.010	0.028	0.043	0.090	0.203	0.380	0.736	1.330
12	2.510	0.011	0.027	0.051	0.087	0.184	0.353	0.711	1.316
13	2.513	0.014	0.023	0.046	0.083	0.195	0.352	0.694	1.346
14	2.499	0.011	0.022	0.049	0.104	0.167	0.372	0.710	1.337
15	2.504	0.015	0.019	0.050	0.088	0.176	0.374	0.712	1.338
16	2.494	0.010	0.025	0.036	0.095	0.170	0.351	0.722	1.319
17	2.492	0.011	0.028	0.046	0.090	0.180	0.381	0.706	1.342
18	2.502	0.014	0.024	0.030	0.080	0.179	0.355	0.700	1.349
19	2.509	0.014	0.029	0.047	0.086	0.173	0.351	0.679	1.346
20	2.486	0.012	0.016	0.048	0.079	0.184	0.344	0.710	1.342
21	2.500	0.015	0.020	0.051	0.097	0.185	0.354	0.738	1.242
22	2.496	0.006	0.015	0.038	0.081	0.202	0.343	0.719	1.335
23	2.502	0.005	0.025	0.040	0.091	0.178	0.363	0.696	1.406
24	2.495	0.008	0.019	0.042	0.101	0.165	0.355	0.708	1.357
25	2.491	0.012	0.022	0.043	0.094	0.157	0.355	0.695	1.396
26	2.493	0.009	0.022	0.040	0.101	0.177	0.361	0.666	1.328
27	2.513	0.013	0.020	0.044	0.086	0.180	0.357	0.677	1.308
28	2.509	0.011	0.024	0.048	0.070	0.188	0.369	0.711	1.314
29	2.504	0.011	0.022	0.040	0.073	0.150	0.357	0.655	1.283
30	2.493	0.013	0.022	0.054	0.074	0.206	0.376	0.677	1.308
31	2.497	0.017	0.027	0.043	0.091	0.169	0.392	0.724	1.559

Table 2: Maximal output and bit values for each channel at (27.5±0.5)°C for the internal reference source.

2 Slope of Bits of 8-bit DAC

Bit	Channel	external source			internal source		
		slope $[10^{-4}\,\mathrm{V}/^{\circ}\mathrm{C}]$	σ $[10^{-4}\,\mathrm{V}/^{\circ}\mathrm{C}]$	χ^2/ **ndf**	**slope** $[10^{-4}\,\mathrm{V}/^{\circ}\mathrm{C}]$	σ $[10^{-4}\,\mathrm{V}/^{\circ}\mathrm{C}]$	χ^2/ **ndf**
0	0	0.429	0.003	0.51	0.419	0.003	0.73
	1	0.325	0.003	0.78	0.337	0.003	1.28
	2	0.234	0.002	0.50	0.238	0.002	0.33
	3	0.280	0.003	0.96	0.278	0.003	1.31
	4	0.323	0.003	0.61	0.346	0.003	1.25
1	0	0.634	0.003	1.04	0.661	0.003	1.31
	1	0.681	0.003	0.56	0.654	0.003	2.24
	2	0.656	0.002	1.63	0.679	0.004	1.17
	3	0.701	0.004	1.06	0.746	0.004	2.27
	4	0.638	0.003	0.63	0.660	0.003	1.71
2	0	1.312	0.005	0.31	1.373	0.004	1.98
	1	1.246	0.005	0.56	1.299	0.004	2.39
	2	1.323	0.004	1.14	1.365	0.004	1.89
	3	1.356	0.005	1.18	1.407	0.005	1.51
	4	1.253	0.004	0.63	1.272	0.004	2.08
3	0	2.525	0.008	0.74	2.583	0.006	1.92
	1	2.640	0.007	0.50	2.760	0.007	2.79
	2	2.552	0.006	1.14	2.783	0.006	1.58
	3	2.624	0.007	1.18	2.785	0.007	2.34
	4	2.537	0.007	1.19	2.666	0.007	1.63
4	0	4.754	0.01	1.06	4.820	0.01	1.98
	1	5.381	0.01	0.64	5.560	0.01	3.95
	2	5.337	0.01	1.06	5.540	0.01	2.08
	3	5.267	0.01	1.03	5.190	0.01	2.95
	4	5.258	0.01	0.85	5.520	0.01	3.45
5	0	10.390	0.03	0.60	10.660	0.02	2.66
	1	9.940	0.02	0.41	10.290	0.02	2.25
	2	10.220	0.02	1.13	10.590	0.02	2.08
	3	10.500	0.02	1.08	10.920	0.02	3.48
	4	10.140	0.02	0.64	10.550	0.02	2.91
6	0	20.220	0.06	0.67	20.590	0.04	2.75
	1	20.700	0.05	0.79	21.470	0.05	2.91
	2	21.000	0.05	0.80	21.780	0.05	3.58
	3	20.520	0.04	0.76	21.240	0.04	3.77
	4	20.370	0.05	1.04	20.850	0.05	3.04
7	0	40.300	0.1	0.69	41.290	0.1	2.42
	1	40.250	0.1	0.63	41.900	0.1	2.17
	2	40.200	0.1	0.74	41.640	0.1	2.94
	3	40.480	0.1	0.54	42.120	0.1	2.50
	4	40.820	0.1	0.78	42.280	0.1	3.84

Table 3: Temperature dependent temperature slope for all bits for the first 5 channels for external and internal reference source.

Bibliography

[1] J. Bluemer, R. Engel, and J. Hoerandel. *Cosmic Rays from the Knee to the Highest Energies*. In: Prog.Part.Nucl.Phys. 63 (2009), pp. 293–338. DOI: 10.1016/j.ppnp.2009.05.002.

[2] K.-H. Kampert and A. Watson. *Extensive Air Showers and Ultra High-Energy Cosmic Rays: A Historical Review*. In: Eur. Phys. J. H37 (2012), pp. 359–412. DOI: 10.1140/epjh/e2012-30013-x.

[3] P. Carlson and A. Watson. *Erich Regener and the ionisation maximum of the atmosphere*. In: History of Geo- and Space Sciences 5.2 (2014), pp. 175–182. DOI: 10.5194/hgss-5-175-2014. URL: http://www.hist-geo-space-sci.net/5/175/2014/.

[4] K. A. Olive et al. *Review of Particle Physics*. In: Chin. Phys. C38 (2014). 090001. DOI: 10.1088/1674-1137/38/9/090001.

[5] A. Letessier-Selvon and T. Stanev. *Ultrahigh energy cosmic rays*. In: Rev. Mod. Phys. 83 (2011), pp. 907–942. DOI: 10.1103/RevModPhys.83.907. URL: http://link.aps.org/doi/10.1103/RevModPhys.83.907.

[6] J. J. Beatty and S. Westerhoff. *The Highest-Energy Cosmic Rays*. In: Annual Review of Nuclear and Particle Science 59.1 (2009), pp. 319–345. DOI: 10.1146/annurev.nucl.58.110707.171154. URL: http://dx.doi.org/10.1146/annurev.nucl.58.110707.171154.

[7] K. Kotera and A. V. Olinto. *The Astrophysics of Ultrahigh-Energy Cosmic Rays*. In: Annual Review of Astronomy and Astrophysics 49.1 (2011), pp. 119–153. DOI: 10.1146/annurev-astro-081710-102620. URL: http://dx.doi.org/10.1146/annurev-astro-081710-102620.

[8] T. Pierog and K. Werner. *EPOS Model and Ultra High Energy Cosmic Rays*. In: Nucl. Phys. Proc. Suppl. 196 (2009), pp. 102–105. DOI: 10.1016/j.nuclphysbps.2009.09.017.

[9] K.-H. Kampert and M. Unger. *Measurements of the cosmic ray composition with air shower experiments*. In: Astroparticle Physics 35.10 (2012), pp. 660–678. DOI: http://dx.doi.org/10.1016/j.astropartphys.2012.02.004. URL: http://www.sciencedirect.com/science/article/pii/S0927650512000382.

[10] A. Aab et al. *Large Scale Distribution of Ultra High Energy Cosmic Rays Detected at the Pierre Auger Observatory with Zenith Angles up to 80°*. In: Astrophys. J. 802.2 (2015), p. 111. DOI: 10.1088/0004-637X/802/2/111.

[11] O. Deligny. *Large-Scale Distribution of Arrival Directions of Cosmic Rays Detected at the Pierre Auger Observatory and the Telescope Array above 10 PeV*. In: Proceedings, Cosmic Ray Anisotropy Workshop (CRA2013). Vol. 531. (2014), p. 012002. DOI: 10.1088/1742-6596/531/1/012002.

[12] A. Aab et al. *Searches for Anisotropies in the Arrival Directions of the Highest Energy Cosmic Rays Detected by the Pierre Auger Observatory*. In: Astrophys. J. 804.1 (2015), p. 15. DOI: 10.1088/0004-637X/804/1/15.

[13] D. Heck et al. *CORSIKA: a Monte Carlo code to simulate extensive air showers*. Forschungszentrum Karlsruhe GmbH, Karlsruhe (Germany), (1998).

[14] R. Engel, D. Heck, and T. Pierog. *Extensive Air Showers and Hadronic Interactions at High Energy*. In: Annual Review of Nuclear and Particle Science 61.1 (2011), pp. 467–489. DOI: 10.1146/annurev.nucl.012809.104544. URL: http://dx.doi.org/10.1146/annurev.nucl.012809.104544.

[15] R. Engel. *Indirect Detection of Cosmic Rays*. In: Handbook of Particle Detection and Imaging. Springer Berlin Heidelberg, (2012), pp. 593–632. ISBN: 9783642132704. DOI: 10.1007/978-3-642-13271-1_24. URL: http://dx.doi.org/10.1007/978-3-642-13271-1_24.

[16] A. Aab et al. *Depth of maximum of air-shower profiles at the Pierre Auger Observatory. I. Measurements at energies above* $10^{17.8}$ eV. In: Phys. Rev. D 90 (12 2014), p. 122005. DOI: 10.1103/PhysRevD.90.122005. URL: http://link.aps.org/doi/10.1103/PhysRevD.90.122005.

[17] A. Tapia et al. *The lateral shower age parameter as an estimator of chemical composition*. In: Proceedings, 33rd International Cosmic Ray Conference (ICRC2013). (2013). URL: http://inspirehep.net/record/1254039/files/arXiv:1309.3536.pdf.

[18] T. Pierog et al. *EPOS LHC: Test of collective hadronization with data measured at the CERN Large Hadron Collider*. In: Phys. Rev. C92.3 (2015), p. 034906. DOI: 10.1103/PhysRevC.92.034906.

[19] A. Aab et al. *Muons in air showers at the Pierre Auger Observatory: Measurement of atmospheric production depth*. In: Phys. Rev. D90.1 (2014). [Erratum: Phys. Rev.D92,no.1,019903(2015)], p. 012012. DOI: 10.1103/PhysRevD.92.019903, 10.1103/PhysRevD.90.012012,10.1103/PhysRevD.90.039904.

[20] A. Aab et al. *Muons in air showers at the Pierre Auger Observatory: Mean number in highly inclined events*. In: Phys. Rev. D91.3 (2015). [Erratum: Phys. Rev.D91,no.5,059901(2015)], p. 032003. DOI: 10.1103/PhysRevD.91.059901, 10.1103/PhysRevD.91.032003.

[21] J. Matthews. *A Heitler model of extensive air showers*. In: Astropart. Phys. 22 (2005), pp. 387–397. DOI: 10.1016/j.astropartphys.2004.09.003.

[22] A. Aab et al. *The Pierre Auger Cosmic Ray Observatory*. In: Nuclear Instruments and Methods in Physics Research Section A: Accelerators, Spectrometers, Detectors and Associated Equipment 798 (2015), pp. 172–213. DOI: http://dx.doi.org/10.1016/j.nima.2015.06.058. URL: http://www.sciencedirect.com/science/article/pii/S0168900215008086.

[23] P. Abreu et al. *Identifying Clouds over the Pierre Auger Observatory using Infrared Satellite Data*. In: Astropart. Phys. 50-52 (2013), pp. 92–101. DOI: 10.1016/j.astropartphys.2013.09.004.

[24] J. Lozano-Bahilo et al. *Results of the Pierre Auger Observatory on High Energy Cosmic Rays*. In: Journal of Physics: Conference Series 160.1 (2009), p. 012038. URL: http://stacks.iop.org/1742-6596/160/i=1/a=012038.

[25] J. Abraham et al. *The fluorescence detector of the Pierre Auger Observatory*. In: Nuclear Instruments and Methods in Physics Research Section A: Accelerators, Spectrometers, Detectors and Associated Equipment 620.2–3 (2010), pp. 227–251. DOI: http://dx.doi.org/10.1016/j.nima.2010.04.023. URL: http://www.sciencedirect.com/science/article/pii/S0168900210008727.

[26] E. Varela. *The low-energy extensions of the Pierre Auger Observatory*. In: J. Phys. Conf. Ser. 468 (2013), p. 012013. DOI: 10.1088/1742-6596/468/1/012013.

[27] I. Allekotte et al. *The surface detector system of the Pierre Auger Observatory*. In: Nuclear Instruments and Methods in Physics Research Section A: Accelerators, Spectrometers, Detectors and Associated Equipment 586.3 (2008), pp. 409–420. DOI: http://dx.doi.org/10.1016/j.nima.2007.12.016. URL: http://www.sciencedirect.com/science/article/pii/S0168900207024680.

[28] P. Billoir. *The Cherenkov Surface Detector of the Pierre Auger Observatory*. In: Nuclear Instruments and Methods in Physics Research Section A: Accelerators, Spectrometers, Detectors and Associated Equipment 766 (2014). RICH2013, Proceedings of the Eighth International Workshop on Ring Imaging Cherenkov Detectors Shonan, Kanagawa, Japan, December 2-6, 2013, pp. 78–82. DOI: http://dx.doi.org/10.1016/j.nima.2014.05.013. URL: http://www.sciencedirect.com/science/article/pii/S0168900214005129.

[29] J. C. Espadanal. *Measurement of the Muon Content of eas With the Pierre Auger Observatory*. In: Proceedings, 30th International Workshop on High Energy Physics: Particle and Astroparticle Physics, Gravitation and Cosmology: Predictions, Observations and New Projects (IHEP 2014). Pierre Auger Collaboration. (2015), pp. 287–292. DOI: 10.1142/9789814689304_0045.

[30] L. Cazón, R. Vázquez, and E. Zas. *Depth development of extensive air showers from muon time distributions*. In: Astroparticle Physics 23.4 (2005), pp. 393–409. DOI: http://dx.doi.org/10.1016/j.astropartphys.2005.01.009. URL: http://www.sciencedirect.com/science/article/pii/S0927650505000253.

[31] A. Aab et al. *Reconstruction of inclined air showers detected with the Pierre Auger Observatory*. In: JCAP 1408.08 (2014), p. 019. DOI: 10.1088/1475-7516/2014/08/019.

[32] M. Ave, R. Vázquez, and E. Zas. *Modeling horizontal air showers induced by cosmic rays*. In: Astroparticle Physics 14.2 (2000), pp. 91–107. DOI: http://dx.doi.org/10.1016/S0927-6505(00)00113-4. URL: http://www.sciencedirect.com/science/article/pii/S0927650500001134.

[33] T. Antoni et al. *The cosmic-ray experiment KASCADE*. In: Nuclear Instruments and Methods in Physics Research Section A: Accelerators, Spectrometers, Detectors and Associated Equipment 513.3 (2003), pp. 490–510. DOI: http://dx.doi.org/10.1016/S0168-9002(03)02076-X. URL: http://www.sciencedirect.com/science/article/pii/S016890020302076X.

[34] W. Apel et al. *The KASCADE-Grande experiment*. In: Nuclear Instruments and Methods in Physics Research Section A: Accelerators, Spectrometers, Detectors and Associated Equipment 620.2–3 (2010), pp. 202–216. DOI: http://dx.doi.org/10.1016/j.nima.2010.03.147. URL: http://www.sciencedirect.com/science/article/pii/S0168900210007734.

[35] *The Next Frontier in UHECR Research with an Upgraded Pierre Auger Observatory*. In: Community Summer Study 2013: Snowmass on the Mississippi (CSS2013) Minneapolis, MN, USA, July 29-August 6, 2013. (2013). URL: http://www.slac.stanford.edu/econf/C1307292/docs/submittedArxivFiles/1307.0226.pdf.

[36] F. Suarez et al. *The AMIGA muon detectors of the Pierre Auger Observatory: overview and status*. In: 33rd International Cosmic Ray Conference, The Astroparticle Physics Conference. Pierre Auger Collaboration. (2013).

[37] T. Hebbeker et al. *Muon measurement using scintillator tiles with SiPM readout*. In: GAP Note (Pierre Auger Collaboration Internal Report) (2013). GAP-2013-057.

[38] P. Abreu et al. *Muon Array with RPCs for Tagging Air showers (MARTA)*. In: Proceedings, 34th International Cosmic Ray Conference (ICRC 2015). (2015).

[39] G. F. Knoll. *Radiation Detection and Measurement*. 4th ed. Wiley, (2010).

[40] H.-C. Schultz-Coulon. *The Physics of Particle Detectors - Scintillation Detectors - Particle Detection via Luminescence*. lecture notes. http://www.kip.uni-heidelberg.de/~coulon/Lectures/Detectors/Free_PDFs/Lecture4.pdf, last visted: November 2015. Kirchhoff Institute for Physics, Heidelberg University, 2011.

[41] R. Cameron et al. *Fogging in Polyvinyl Toluene Scintillators*. In: Nuclear Science, IEEE Transactions on 62.1 (2015), pp. 368–371. DOI: 10.1109/TNS.2015.2390076.

[42] Eljen Technology. *EJ-212 Plastic Scintillator*. data sheet. http://www.eljentechnology.com/index.php/products/plastic-scintillators/64-ej-212, last visited: November 2015, (2007).

[43] DuPont. *DuPont™ Tyvek® Graphics - Typical Properties of Tyvek® style 10*. data sheet. http://www2.dupont.com/Tyvek_Graphics/en_US/assets/downloads/Typical_properties_UK_10%20styles.pdf, last visited: November 2015, (2008).

[44] M. Janecek and W. W. Moses. *Optical Reflectance Measurements for Commonly Used Reflectors*. In: IEEE Transactions on Nuclear Science 55 (2008), pp. 2432–2437. DOI: 10.1109/TNS.2008.2001408.

[45] Saint-Gobain Crystals. *Scintillating Optical Fibres*. data sheet. http://www.crystals.saint-gobain.com/uploadedFiles/SG-Crystals/Documents/SGC%20Fibers%20Brochure.pdf, last visited: November 2015, (2014).

[46] A. Dyshkant et al. *Small scintillating cells as the active elements in a digital hadron calorimeter for the e^+ e^- linear collider detector*. In: Journal of Physics G: Nuclear and Particle Physics 30.9 (2004), N1. URL: http://stacks.iop.org/0954-3899/30/i=9/a=N01.

[47] Saint-Gobain Ceramics and Plastics. *BC-600 Optical Cement*. data sheet. http://www.crystals.saint-gobain.com/uploadedFiles/SG-Crystals/Documents/SGC%20BC600%20Data%20Sheet.pdf, last visited: November 2015, (2014).

[48] Hamamatsu Photonics K.K., Solid State Division. *MPPC (multi-pixel photon counter) - S12571-025, -050, -100C/P*. datasheet. https://www.hamamatsu.com/resources/pdf/ssd/mppc_kapd9003e.pdf, last visited: November 2015, (2013).

[49] Edmund Optics. *1000µm Faser optischer Güte Plastik ohne Mantel*. data sheet. http://www.edmundoptics.de/optics/fiber-optics/optical-grade-fiber-optics/02534/, last visted: November 2015, (2014).

[50] S. Nieswand. *Measurement of the exit characteristics of light from optical multimode plastic fibres*. master's thesis. RWTH Aachen University, (2014).

[51] SensL sense light. *An Introduction to the Silicon Photomultiplier*. technical note. http://www.sensl.com/downloads/ds/TN%20-%20Intro%20to%20SPM%20Tech.pdf, last visited: November 2015, (2011).

[52] Hamamatsu Photonics K.K., Solid State Division. *MPPC, MPPC modules*. technical information. https://www.hamamatsu.com/resources/pdf/ssd/mppc_kapd0002e.pdf, last visted: November 2015, (2015).

[53] D. Renker and E. Lorenz. *Advances in solid state photon detectors*. In: JINST 4 (2009), P04004. DOI: 10.1088/1748-0221/4/04/P04004.

[54] L. Gallego et al. *Modeling crosstalk in silicon photomultipliers*. In: JINST 8 (2013), P05010. DOI: 10.1088/1748-0221/8/05/P05010.

[55] M. Putignano, A. Intermite, and C. Welsch. *Study of the response of Silicon Photomultipliers in presence of strong cross-talk noise*. In: Proceedings, 2nd International Conference, IPAC 2011, San Sebastian, Spain. (2011).

[56] Omega - Orsay Micro Electronics Group Associated. *EASIROC - Software & Test Board User Guide*. user guide. Institut National de Physique Nucléaire et de Physique des Particules, 3 Rue Michel-Ange, 75794 Paris CEDEX 16, Fance, (2012).

[57] Omega; Orsay Micro Electronics Group Associated. *EASIROC - Datasheet*. Institut National de Physique Nucléaire et de Physique des Particules, 3 Rue Michel-Ange, 75794 Paris CEDEX 16, Fance, (2011).

[58] L. Middendorf. *Readout Electronics and DAQ for the SiPM based muon detector prototype "Aachen Muon Detector"*. to be published. PhD Thesis. III. Phys. Inst. A, RWTH Aachen University, (2016).

[59] B. Philipps. Mechanical Workshop, III Phys. Inst. A, RWTH Aachen University, private communication. (2015).

[60] LumiTronix. *Superbright LED UV 130mcd 20° 3.1V*. datasheet. http://www.leds.de/en/Ordinary-LEDs/LEDs-5mm/Colored-LEDs/Superbright-LED-UV-130mcd-20-3-1V.html, last visted: November 2015, (2015).

[61] Fluke Corporation. *FLUKE 8845A/8846A Digital Multimeter - Users Manual*. datasheet. http://assets.fluke.com/manuals/8845a___pmeng0200.pdf, last visted: November 2015, (2006).

[62] T. Hermanns. *Aufbau eines Systems für Kühltests zur Qualitätsüberwachung von CMS Silizium-Modulen*. Diplomarbeit. RWTH Aachen University, (2004).

[63] C. Peters et al. *The muon detector prototype AMD for the determination of the muon content in UHECRs*. In: Proceedings, 34th International Cosmic Ray Conference (ICRC 2015). (2015).

[64] R. Brun and F. Rademakers. *ROOT: An object oriented data analysis framework*. In: Nucl. Instrum. Meth. A389 (1997), pp. 81–86. DOI: 10.1016/S0168-9002(97)00048-X.

[65] D. Impiombato et al. *Characterization of EASIROC as Front-End for the readout of the SiPM at the focal plane of the Cherenkov telescope ASTRI*. In: Nucl. Instrum. Meth. A729 (2013), pp. 484–490. DOI: 10.1016/j.nima.2013.07.029.

[66] D. Louis. Electronics Workshop, III. Phys. Inst. A, RWTH Aachen University, private communication. (2015).

[67] M. Wirtz. *Simulation studies of a novel scintillator detector with SiPM readout for muons of cosmic ray air showers*. bachelor's thesis. RWTH Aachen University, (2014).

[68] T. Niggemann. III Phys. Inst. A, RWTH Aachen University, private communication. (2015).

[69] O. Allkofer and H. Jokisch. *A survey on the recent measurements of the absolute vertical cosmic-ray muon flux at sea level*. English. In: Il Nuovo Cimento A (1965-1970) 15.3 (1973), pp. 371–389. DOI: 10.1007/BF02734678. URL: http://dx.doi.org/10.1007/BF02734678.

[70] T. Hebbeker and C. Timmermans. *A compilation of high energy atmospheric muon data at sea level*. In: Astroparticle Physics 18.1 (2002), pp. 107–127. DOI: http://dx.doi.org/10.1016/S0927-6505(01)00180-3. URL: http://www.sciencedirect.com/science/article/pii/S0927650501001803.

[71] I. Bekman. *Inbetriebnahme eines Praktikumsversuchs zur Messung kosmischer Strahlung*. bachelor's thesis. RWTH Aachen University, (2010).

[72] J. N. Crookes and B. C. Rastin. *An investigation of the absolute intensity of muons at sea-level*. In: Nucl. Phys. B39 (1972), pp. 493–508. DOI: 10.1016/0550-3213(72)90384-7.

Acknowledgements

During the course of this thesis I could benefit of the diverse support of many people whom I would like to thank in the following.

Foremost, I would like to express my sincere gratitude to Prof. Thomas Hebbeker for the opportunity to study this interesting subject and his continuous enthusiasm and fruitful discussions in our frequent team meetings. Besides, I would like to thank Prof. Christopher Wiebusch who kindly agreed to be the second examiner for my thesis.

In addition, my warm thanks go to our small Aachen Muon Detector working group and thus to the people who supervised my work. Lukas Middendorf and Christine Peters have always supported me with their inspiring ideas and are great team players for reaching our common goal, the AMD. Furthermore, I would like to thank Jun. Prof. Thomas Bretz for his thought-provoking impulses.

Many thanks to all Institute III A colleagues and friends. Especially to my office mates Tim Niggemann and Florian Scheuch who always had helpful answers for all my little questions; to Sebastian Thüer for all his support whenever needed; to the employees of the mechanical and electronics workshop whom made the construction of our detector possible in the first place; to my proofreaders Florian Briechle, Markus Lauscher, Lukas Middendorf, Tim Niggemann, Christine Peters, and Sebastian Thüer for all their comments; and last but not least to Adriana del Piero, Melanie Roder and Iris Rosewick the ever friendly and helpful ladies from the secretary and administration without whom all organisational tasks would not have been possible.

Last but not least, I would like to thank my family and friends for their support during this time.

Erklärung

Hiermit versichere ich, dass ich diese Arbeit einschließlich beigefügter Zeichnungen, Darstellungen und Tabellen selbstständig angefertigt und keine anderen als die angegebenen Hilfsmittel und Quellen verwendet habe. Alle Stellen, die dem Wortlaut oder dem Sinn nach anderen Werken entnommen sind, habe ich in jedem einzelnen Fall unter genauer Angabe der Quelle deutlich als Entlehnung kenntlich gemacht.

Aachen, den 4. Februar 2016

Rebecca Meißner